

## REVIEW ARTICLE

# Growth and applications of Group III-nitrides

**O Ambacher**Walter Schottky Institute, Technical University Munich, Am Coulombwall,  
D-85748 Garching, Germany

Received 18 February 1997, in final form 15 June 1998

**Abstract.** Recent research results pertaining to InN, GaN and AlN are reviewed, focusing on the different growth techniques of Group III-nitride crystals and epitaxial films, heterostructures and devices. The chemical and thermal stability of epitaxial nitride films is discussed in relation to the problems of deposition processes and the advantages for applications in high-power and high-temperature devices. The development of growth methods like metalorganic chemical vapour deposition and plasma-induced molecular beam epitaxy has resulted in remarkable improvements in the structural, optical and electrical properties. New developments in precursor chemistry, plasma-based nitrogen sources, substrates, the growth of nucleation layers and selective growth are covered. Deposition conditions and methods used to grow alloys for optical bandgap and lattice engineering are introduced. The review is concluded with a description of recent Group III-nitride semiconductor devices such as bright blue and white light-emitting diodes, the first blue-emitting laser, high-power transistors, and a discussion of further applications in surface acoustic wave devices and sensors.

## 1. Introduction

Group III-nitrides have been considered a promising system for semiconductor devices applications since 1970, especially for the development of blue- and UV-light-emitting diodes. The III–V nitrides, aluminium nitride (AlN), gallium nitride (GaN) and indium nitride (InN), are candidate materials for optoelectrical applications at such photon energies, because they form a continuous alloy system (InGa<sub>1-x</sub>N, InAl<sub>1-x</sub>N, and AlGa<sub>1-x</sub>N) whose direct optical bandgaps for the hexagonal wurtzite phase range from 1.9 eV for  $\alpha$ -InN and 3.4 eV for  $\alpha$ -GaN to 6.2 eV for  $\alpha$ -AlN. The cubic modifications have bandgaps in the range from 1.7 eV for  $\beta$ -InN and 3.2 eV for  $\beta$ -GaN to 4.9 eV for  $\beta$ -AlN (figures 1 and 2) [1–6]. Other advantageous properties include high mechanical and thermal stability, large piezoelectric constants and the possibility of passivation by forming thin layers of Ga<sub>2</sub>O<sub>3</sub> or Al<sub>2</sub>O<sub>3</sub> with bandgaps of approximately 4.2 eV and 9 eV. The spontaneous and piezoelectric polarization (in the wurtzite materials) and the high electron drift velocities ( $2 \times 10^5$  m s<sup>-1</sup> [7]) of GaN can be used to fabricate high-power transistors based on AlGa<sub>1-x</sub>N/GaN heterostructures. In addition, AlN is an important material with a variety of applications such as passive barrier layers, high-frequency acoustic wave devices, high-temperature windows, and dielectric optical enhancement layers in magneto-optic multilayer structures [8, 9].

Very informative reviews of the growth techniques and structural, optical and electrical properties of Group III-nitrides and their alloys have been presented by Strite *et al* [10, 11]. A good overview of applications of Group III-nitride based heterostructures for UV emitters and high-temperature, high-power electronic devices is provided in [12] and [13]. This review focuses on the development of the different growth techniques successfully applied to the deposition of Group III-nitride epitaxial films and heterostructures, such as chemical transport and metalorganic chemical vapour deposition (MOCVD), sputtering and molecular beam epitaxy (MBE). The quality of state-of-the-art material and its application for optical and electronic devices are discussed in detail in order to point out possible limitations, promising developments and future trends.

The first systematic effort to grow InN, GaN and AlN by chemical vapour deposition or sputtering processes took place in the 1970s in order to characterize the optical and structural properties of thin films. At that time, neither metalorganic precursors containing In or Al with electronic grade purity, plasma sources for nitrogen radicals compatible with MBE systems, nor substrate material with reasonably good thermal and lattice matches to the nitrides were available. The InN and GaN material had large concentrations of free electrons, presumed to result from oxygen impurities and intrinsic defects, and the structural quality of the AlN films was not good enough for optical

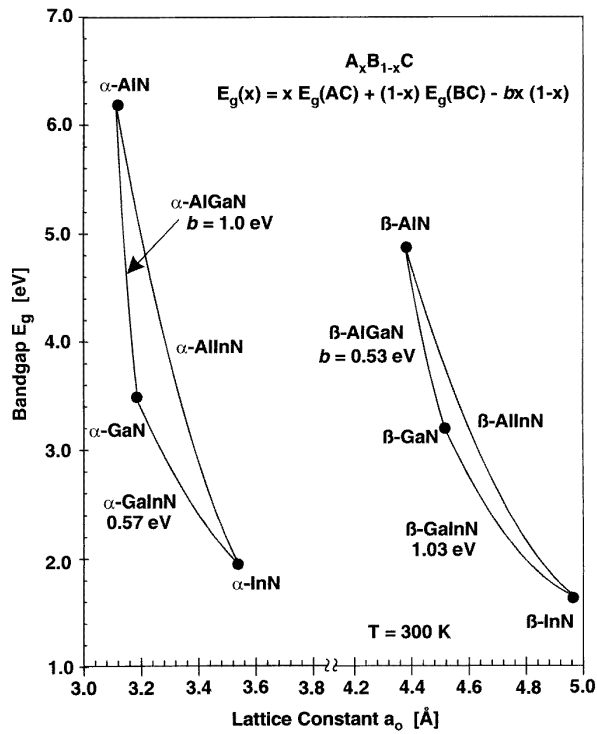


**Figure 1.** Bandgap and bowing parameters of hexagonal ( $\alpha$ -phase) and cubic ( $\beta$ -phase) InN, GaN, AlN and their alloys versus lattice constant  $a_0$  [1–6].

or electronic applications. Primarily, the development of MOCVD and plasma-induced molecular beam epitaxy (PIMBE) over the last eight years has led to a number of recent advances and important improvements in structural properties.

## 2. Crystal structure, polarity and polarization of InN, GaN and AlN

In contrast to cubic III–V semiconductors like GaAs and InP with the zincblende structure, the thermodynamically stable phase of InN, GaN and AlN, is the hexagonal wurtzite structure ( $\alpha$ -phase). Beside the  $\alpha$ -phase, a metastable  $\beta$ -phase with zincblende structure exists and a cubic high-pressure modification with NiAs structure was observed for pressures above 25 kbar in the case of AlN [14]. Because the  $\alpha$ - and  $\beta$ -phases of Group III-nitrides only differ in the stacking sequence of nitrogen and metal atoms (polytypes), the coexistence of hexagonal and cubic phases is possible in epitaxial layers, for example due to stacking faults. The hexagonal crystal structure of Group III-nitrides can be described by the edge length  $a_0$  of the basal hexagon, the height  $c_0$  of the hexagonal prism and an internal parameter  $u$  defined as the anion–cation bond length along the (0001) axis. Because of the different cations and ionic radii ( $\text{Al}^{3+}$ : 0.39 Å,  $\text{Ga}^{3+}$ : 0.47 Å,  $\text{In}^{3+}$ : 0.79 Å [15]), InN, GaN and AlN have different lattice constants, bandgaps and binding energies as shown in table 1 [16, 17].

Both wurtzite and zincblende structures have polar axes (lack of inversion symmetry). In particular, the bonds in

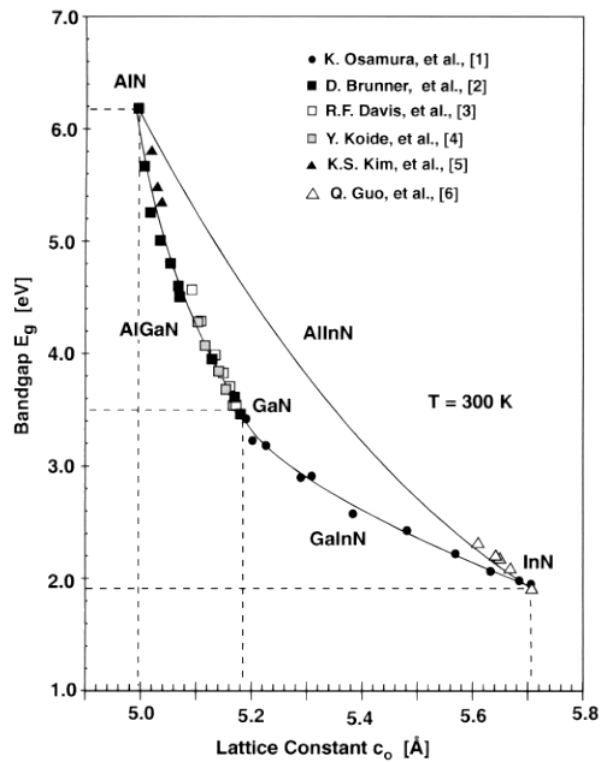


**Figure 2.** Experimental results of bandgaps of hexagonal Group III-nitrides versus lattice constant  $c_0$  at room temperature [1–6].

**Table 1.** Lattice constants, bandgaps and binding energies of hexagonal InN, GaN and AlN.

Wurtzite, 300 K	AlN	GaN	InN
$a_0$ (Å) <sup>b</sup>	3.112	3.189	3.54
$c_0$ (Å) <sup>b</sup>	4.982	5.185	5.705
$c_0/a_0$ (exp.) <sup>b</sup>	1.6010	1.6259	1.6116
$c_0/a_0$ (calc.) <sup>a</sup>	1.6190	1.6336	1.6270
$u_0$ <sup>a</sup>	0.380	0.376	0.377
$a_{\text{Bohr}}$ (Å) <sup>a</sup>	5.814	6.04	6.66
$E_B(\text{M–N})^c$ (eV) <sup>b</sup>	2.88	2.20	1.98

<sup>a</sup> From [16].

<sup>b</sup> From [17].

<sup>c</sup> M = In, Ga or Al, N = nitride.

the (0001) direction for wurtzite and (111) direction for zincblende are all faced by nitrogen in the same direction and by the cation in the opposite direction. Both bulk and surface properties can depend significantly on whether the surface is faced by nitrogen or metal atoms [18, 19]. The most common growth direction of hexagonal GaN is normal to the {0001} basal plane, where the atoms are arranged in bilayers consisting of two closely spaced hexagonal layers, one with cations and the other with anions, so that the bilayers have polar faces. Thus, in the case of GaN a basal surface should be either Ga- or N-faced. By Ga-faced we mean Ga on the top position of the {0001} bilayer, corresponding to [0001] polarity (figure 3). Ga-faced does not mean Ga-terminated; termination should only be used

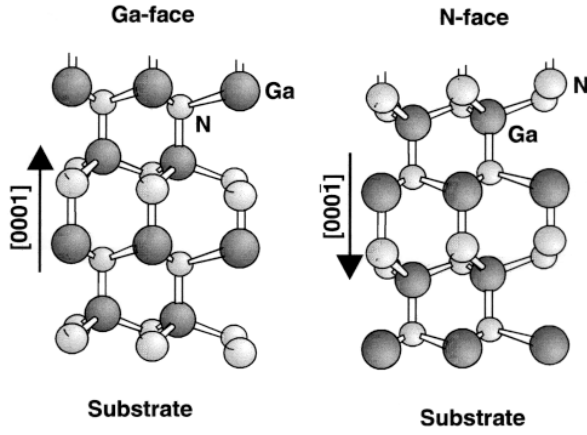


**Figure 3.** Different polarities (Ga- and N-faced) of wurtzite GaN.

to describe a surface property. A Ga-face surface might be N-terminated if it is covered with nitrogen atoms, but without flipping the crystal it will never be N-faced. It is, however, important to note that the (0001) and (000 $\bar{1}$ ) surfaces of GaN are inequivalent (by convention, the [0001] direction is given by a vector pointing from a Ga atom to a nearest-neighbour N atom).

It has been reported that high-quality epitaxial GaN films deposited by MOCVD on *c*-plane sapphire substrates grow in the (0001) direction with Ga-faced surfaces, while MBE growth commonly occurs in the (000 $\bar{1}$ ) direction, yielding an N-faced film [20–22].

Polar faces are known to have very marked effects on growth in binary cubic semiconductors. For example, growth along the Ga-faced {111} direction of GaAs is known to be slow and has the tendency to produce planar surfaces, whereas growth of the As-face is fast and rough [23]. Similarly, Ponce *et al* found that the smooth side of bulk single crystal platelets corresponds to the Ga-face (0001) whereas the N-face (000 $\bar{1}$ ) is much rougher [20].

In the following we will discuss the influence of spontaneous and piezoelectric polarization on the physical properties of Group III-nitrides. This class of polarization-related properties is obviously important for devices (section 9) because the electric fields influence the shape of the band edges and the carrier distribution inside nitride-based heterostructures. Therefore spontaneous and piezoelectric polarization can influence the radiative recombination in light-emitting devices as well as the electrical properties of the transistor structures discussed in detail later.

Wurtzite is the structure with highest symmetry compatible with the existence of spontaneous polarization [16, 24, 25] and the piezoelectric tensor of wurtzite has three independent nonvanishing components. Therefore, polarization in these material systems will have both a spontaneous and a piezoelectric component. Because of the sensitive dependence of spontaneous polarization on the structural parameters, there are some quantitative differences in polarization of the three nitrides studied here. The increasing nonideality of the crystal structure going

**Table 2.** Spontaneous polarization, piezoelectric and dielectric constants of AlN, GaN and InN.

Wurtzite	AlN	GaN	InN
$\mathbf{P}_{SP}$ (C m $^{-2}$ )	−0.081	−0.029	−0.032
$e_{33}$ (C m $^{-2}$ )	1.46 <sup>a</sup> 1.55 <sup>b</sup>	0.73 <sup>a</sup> 1 <sup>c</sup> 0.65 <sup>d</sup> 0.44 <sup>e</sup>	0.97 <sup>a</sup>
$e_{31}$ (C m $^{-2}$ )	−0.60 <sup>a</sup> −0.58 <sup>b</sup>	−0.49 <sup>a</sup> −0.36 <sup>c</sup> −0.33 <sup>d</sup> −0.22 <sup>e</sup>	−0.57 <sup>a</sup>
$e_{15}$ (C m $^{-2}$ )	−0.48 <sup>b</sup>	−0.3 <sup>c</sup> −0.33 <sup>d</sup> −0.22 <sup>e</sup>	
$\epsilon_{11}$	9.0 <sup>b</sup>	9.5 <sup>f</sup>	
$\epsilon_{33}$	10.7 <sup>b</sup>	10.4 <sup>f</sup>	

<sup>a</sup> From [16].

<sup>b</sup> From [26].

<sup>c</sup> From [27].

<sup>d</sup> From [28].

<sup>e</sup> From [29].

<sup>f</sup> From [30].

from GaN to InN to AlN ( $u_0$  increases and  $c_0/a_0$  decreases (table 1)), corresponds to an increase in spontaneous polarization. In the absence of external electric fields, the total macroscopic polarization  $\mathbf{P}$  of a solid is the sum of the spontaneous polarization  $\mathbf{P}_{SP}$  in the equilibrium lattice and the strain-induced or piezoelectric polarization  $\mathbf{P}_{PE}$ .

Here we consider polarizations along the (0001) axis, because this is the direction along which standard bulk materials, epitaxial films and heterostructures are grown. Spontaneous polarization along the *c*-axis is  $\mathbf{P}_{SP} = \mathbf{P}_{SP} \mathbf{z}$  (the direction of spontaneous polarization is determined by the polarity; the direction of the piezoelectric polarization depends on the polarity and whether the material is under tensile or compressive stress) and piezoelectric polarization can be calculated by using the piezoelectric coefficients  $e_{33}$  and  $e_{13}$  (table 2) as

$$\mathbf{P}_{PE} = e_{33}\epsilon_z + e_{31}(\epsilon_x + \epsilon_y) \quad (1)$$

where  $a_0$  and  $c_0$  are the equilibrium values of the lattice parameters,  $\epsilon_z = (c - c_0)/c_0$  is the strain along the *c*-axis, and the in-plane strain  $\epsilon_x = \epsilon_y = (a - a_0)/a_0$  is assumed to be isotropic. The third independent component of the piezoelectric tensor,  $e_{15}$ , is related to the polarization induced by shear strain and will not be discussed.

To give an example of the possible influence of polarization on the physical properties of nitride-based heterostructures, we calculate the electric field caused by polarization inside a Ga-faced  $\text{Al}_x\text{Ga}_{1-x}\text{N}/\text{GaN}/\text{Al}_x\text{Ga}_{1-x}\text{N}$  quantum well. We assume that the GaN is grown pseudomorphically on the AlGaN ( $a(\text{GaN}) = a(\text{AlGaN})$ )

**Table 3.** Experimental and calculated values of the piezoelectric constants and bulk modulus for wurtzite and zincblende Group III-nitrides.

GPa	AlN		GaN		InN	
	exp. <sup>a</sup>	calc. <sup>b</sup>	exp. <sup>c</sup>	calc. <sup>b</sup>	exp. <sup>d</sup>	calc. <sup>b</sup>
$C_{11}$	345	396	374	367	190	223
$C_{12}$	125	137	106	135	104	115
$C_{13}$	120	108	70	103	121	92
$C_{33}$	395	373	379	405	182	224
$C_{44}$	118	116	101	95	10	48
$B$	201	207	180	202	139	141
zincblende						
$C_{11}$	calc. <sup>e</sup>	calc. <sup>b</sup>	calc. <sup>e</sup>	calc. <sup>b</sup>	calc. <sup>e</sup>	calc. <sup>b</sup>
$C_{12}$	304	304	296	293	184	187
$C_{13}$	152	160	154	159	116	125
$C_{44}$	199	193	206	155	177	86

<sup>a</sup> From [31].<sup>b</sup> From [32].<sup>c</sup> From [33].<sup>d</sup> From [34].<sup>e</sup> From [35].

and that screening effects due to free carriers and surface states can be neglected.

The lattice constants  $a$  and  $c$  of the GaN layer are decreased and increased respectively, due to the biaxial compressive stress which becomes larger with increasing Al content of the AlGaIn film. The relation between the lattice constants of the hexagonal GaN is given by

$$\frac{c - c_0}{c_0} = -2 \frac{C_{13}}{C_{33}} \frac{a - a_0}{a_0} \quad (2)$$

where  $C_{13}$  and  $C_{33}$  are elastic constants (table 3). Using equations (1) and (2) the amount of piezoelectric polarization in the direction of the  $c$ -axis can be determined by

$$P_{PE} = 2 \frac{a - a_0}{a_0} \left( e_{31} - e_{33} \frac{C_{13}}{C_{33}} \right). \quad (3)$$

The strain of the pseudomorphically grown GaN can be calculated using Vegard's law (linear interpolation of the lattice constants of relaxed  $\text{Al}_x\text{Ga}_{1-x}\text{N}$  from the values for GaN and AlN:  $a(x) = (-0.077x + 3.189)\text{\AA}$  (table 1)), leading to

$$P_{PE}(\text{GaN}) = 0.0163x \text{ C m}^{-2} \quad (4)$$

and a total polarization of

$$P(\text{GaN}) = P_{SP}(\text{GaN}) + P_{PE}(\text{GaN}) = (-0.029 + 0.0163x) \text{ C m}^{-2}. \quad (5)$$

The polarization generates an electric field  $E(\text{GaN})$  inside the GaN layer:

$$E(\text{GaN}) = -\frac{P(\text{GaN})}{\varepsilon(\text{GaN})\varepsilon_0} = (3.6 \times 10^6 - 2.1 \times 10^6 x) \text{ V cm}^{-1} \quad (6)$$

where  $\varepsilon(\text{GaN})$  (table 2) and  $\varepsilon_0$  are the dielectric constants of GaN and vacuum.

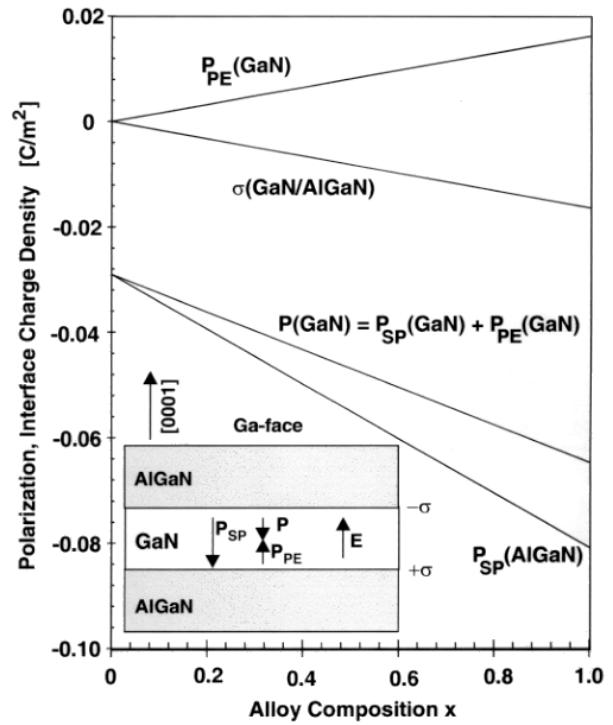


**Figure 4.** Polarization (spontaneous, piezoelectric and total polarization) of a relaxed  $\text{Al}_x\text{Ga}_{1-x}\text{N}$  and a pseudomorphic on top of  $\text{Al}_x\text{Ga}_{1-x}\text{N}$  grown GaN layer versus Al content  $x$ . The interface charge  $\sigma$  is caused by the different total polarizations of the GaN and the AlGaIn film.

The AlGaIn is assumed free of strain and therefore the piezoelectric polarization equals zero. The total polarization of the AlGaIn can be described by a linear approximation between the spontaneous polarization of GaN and AlN:

$$P(\text{AlGaIn}) = P_{SP}(\text{AlGaIn}) = (-0.029 - 0.052x) \text{ C m}^{-2}. \quad (7)$$

A charge density at the GaN/AlGaIn interfaces,  $\sigma(\text{GaN/AlGaIn})$ , is caused by the different polarizations of GaN and AlGaIn:

$$\pm\sigma(\text{GaN/AlGaIn}) = P(\text{GaN}) - P(\text{AlGaIn}) = \pm 0.068x \text{ C m}^{-2}. \quad (8)$$

The spontaneous polarization, piezoelectric polarization and interface charge density of GaN embedded in two  $\text{Al}_{0.15}\text{Ga}_{0.85}\text{N}$  layers are determined to be  $-0.029$ ,  $0.0025$  and  $\pm 0.0025 \text{ C m}^{-2}$  respectively. (For AlGaIn/GaN/AlGaIn heterostructures with different Al content  $x$ , see figure 4.) The electric field caused by polarization effects can reach a strength of  $3 \times 10^6 \text{ V cm}^{-1}$ .

The modification of the band edges due to spontaneous polarization and piezoelectric fields inside the GaN layer can have a significant influence on the optical properties (figure 5). Due to the Stark and Franz-Keldysh effects, the effective bandgap of GaN will be red-shifted and the recombination probability of electron hole pairs will be decreased because of the spatial separation of electrons and holes [36, 37]. These physical effects thus change the energy of the electroluminescence out of GaN or InGaIn

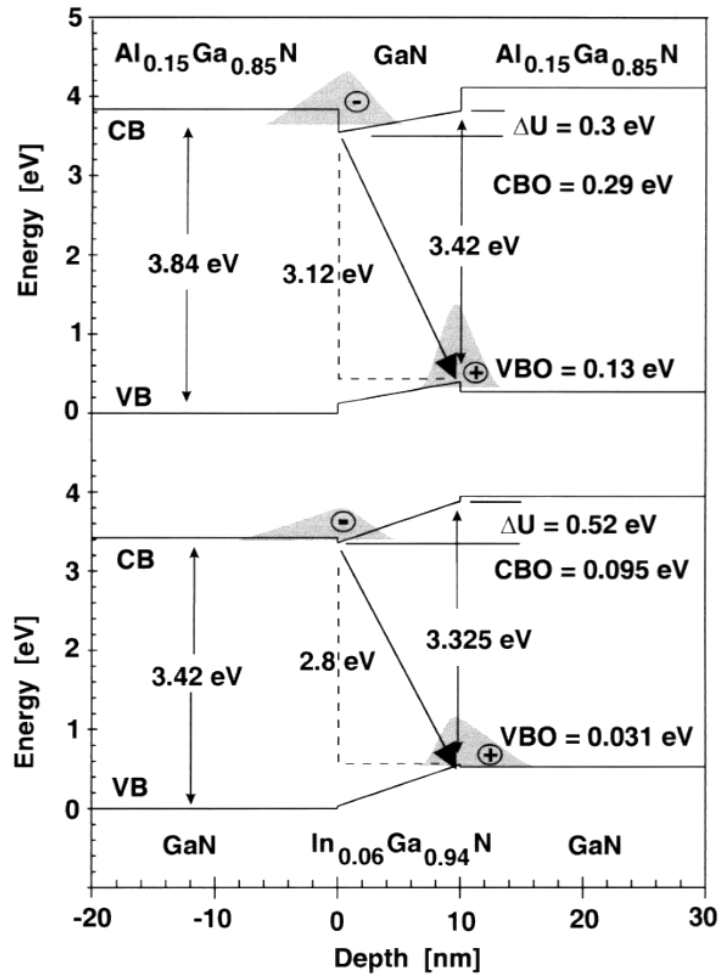


**Figure 5.** Conduction and valence band edges of a pseudomorphic grown AlGaIn/GaN/AlGaIn ( $x = 0.15$ ) and GaN/InGaIn/GaN ( $x = 0.06$ ) heterostructure. The arrows indicate schematically the radiative recombination of an electron and a hole, which is red-shifted in comparison to the bandgap energy due to the Stark effect.

quantum wells and the recombination rates of carriers inside a Group III-nitride based laser structure (section 9.5). The strong electric fields can also enhance electron or hole accumulation at AlGaIn/GaN interfaces (figure 5). This effect can be used in heterostructure field effect transistors, as discussed later in section 9.3. At which interface (lower or upper) of a AlGaIn/GaN/AlGaIn heterostructure electrons or holes are confined depends on the polarity of the material.

In respect of polarization effects, the Group III-nitrides exhibit unusual properties. The piezoelectric constants have the same sign as in II–VI compounds, and opposite to those of III–V compounds. The absolute values of the piezoelectric constants are up to ten times larger than in conventional III–V and II–VI compounds. In particular the constants  $e_{33}$  and  $e_{31}$  of AlN are larger than those of ZnO and BeO [38], and are therefore the largest known so far among the tetrahedrally bonded semiconductors. The spontaneous polarization (the polarization at zero strain) is also very large in the nitrides. That of AlN is only about three to five times smaller than in typical ferroelectric perovskites [39]. For these reasons, the spontaneous and piezoelectric polarization of hexagonal Group III-nitrides

can have a much larger influence on the electrical and optical properties of devices than in other III–V compounds. Finally it should be mentioned that free carriers with a concentration above  $10^{18} \text{ cm}^{-3}$ , charged defects or compensation of surface charges by adsorbates can reduce the polarization-induced electric fields and have to be considered in a detailed analysis of polarization-related effects.

### 3. Thermal properties and stability

The primary methods of obtaining crystal material rely on growing epitaxial layers on different substrates at high temperatures. Unfortunately, the different coefficients of thermal expansion between substrate and nitride introduce residual stress upon cooling. These induced stresses can cause additional structural defects and piezoelectric fields and will influence the optical and electrical properties of films and devices.

The determination of thermal expansivity is not only related to other thermal properties (thermal conductivity, specific heat) but can also yield parameters pertinent to

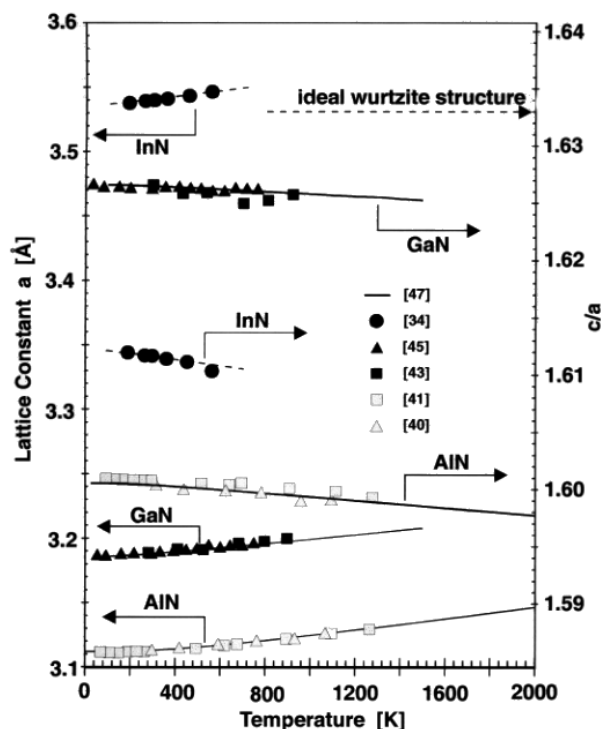


**Figure 6.** Lattice constant and  $c/a$  ratio versus temperature.

other basic properties, like the temperature dependence of the band gap [2]. The value of the thermal expansion coefficient depends on many parameters, such as defect concentration, free carriers, and strains, and the published values are somewhat scattered. The thermal expansivities perpendicular and parallel to the  $c$ -axis in hexagonal material are usually different. The lattice parameters and the thermal expansion coefficient have been measured to intermediate temperatures for AlN, GaN and once for InN [30,40–46]. The increase of the lattice constant  $a$  and the thermal expansion coefficients of hexagonal InN, GaN and AlN with increasing temperature measured by different groups are shown for comparison in figures 6 and 7. As the lattice constants  $a$  and  $c$  increase, the  $c/a$  ratio of the lattice constants becomes smaller with increasing temperature. The experimental data of the lattice constants and thermal expansion coefficients for AlN and GaN are in good agreement with the theoretical calculations of Wang and Reeber (figure 7) [47]. The calculated thermal expansion coefficients of AlN, GaN and InN at 100 K are  $1.3 \times 10^{-8} \text{ K}^{-1}$ ,  $1.2 \times 10^{-6} \text{ K}^{-1}$  and  $2.4 \times 10^{-6} \text{ K}^{-1}$  for  $a_0$  and  $-5 \times 10^{-8} \text{ K}^{-1}$ ,  $1.1 \times 10^{-6} \text{ K}^{-1}$  and  $2.8 \times 10^{-6} \text{ K}^{-1}$  for  $c_0$ . At 600 K, these values become  $5.3 \times 10^{-6} \text{ K}^{-1}$ ,  $5 \times 10^{-6} \text{ K}^{-1}$  and  $5.7 \times 10^{-6} \text{ K}^{-1}$  for  $a_0$  and  $4.4 \times 10^{-6} \text{ K}^{-1}$ ,  $4.4 \times 10^{-6} \text{ K}^{-1}$  and  $3.7 \times 10^{-6} \text{ K}^{-1}$  for  $c_0$ . Below 100 K the thermal expansion coefficient of AlN was calculated to be negative. Above 600 K up to the decomposition temperature (discussed below), the thermal expansion coefficients gradually increase by up to 25%.

The lattice constants, binding energy and decomposition temperature of Group III-nitrides have important consequences for the thermal stability of nitride-based devices.

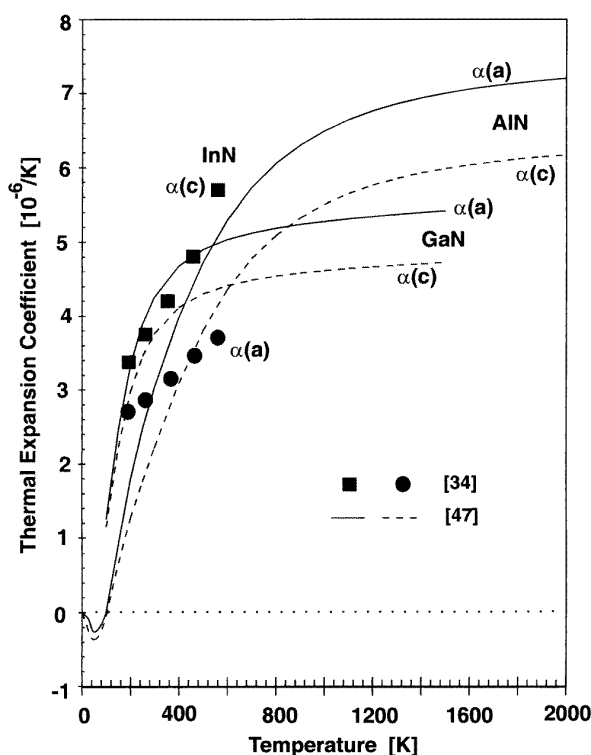


**Figure 7.** Thermal expansion coefficients parallel ( $\alpha(c)$ ) and perpendicular ( $\alpha(a)$ ) to the  $c$ -axis versus temperature.

The relatively large range of uncertainty and the limited number of experimental data concerning nitrogen diffusion, the temperature dependence of the nitrogen flux from a nitride crystal surface and the nitrogen pressures necessary to stabilize a GaN melt are due in part to the very high melting points  $T^M$  and  $N_2$  equilibrium pressures of the Group III-nitrides.

Recently, the thermal stability of InN was investigated at  $N_2$  pressures extending up to 18.5 kbar [48]. It was shown by differential thermal analysis that, over the whole investigated pressure range (0.1–18.5 kbar), rapid decomposition of InN occurs above  $(710 \pm 10)^\circ\text{C}$ . Trainor and Rose [49] observed dissociation of thin InN films at  $500^\circ\text{C}$  and 1 bar  $N_2$ . Guo and Kato [50] observed a change of the reflective high-energy electron diffraction (RHEED) pattern of InN single crystal films when the temperature was raised above  $550^\circ\text{C}$ . They concluded that the crystals decomposed to In and  $N_2$  above that temperature. MacChesney *et al* observed the equilibrium partial pressure of  $N_2$  over InN to be 1 bar at 800 K, increasing exponentially with  $1/T$  to  $10^5$  bar at 1100 K [51] (figure 8).

The first study of the thermal stability of GaN was made by Johnson *et al* [52]. More recently Sime and Margrave [53] investigated the evaporation of GaN and Ga metal in the temperature range 900 to  $1150^\circ\text{C}$  at 1 atm pressure of  $N_2$ ,  $NH_3$  and  $H_2$ , while studying the formation and decomposition equilibria. They determined the heat of evaporation and proposed the existence of  $[GaN]_x$  polymers in the gas phase. Thurmond and Logan [54] chemically measured the partial pressure ratios which

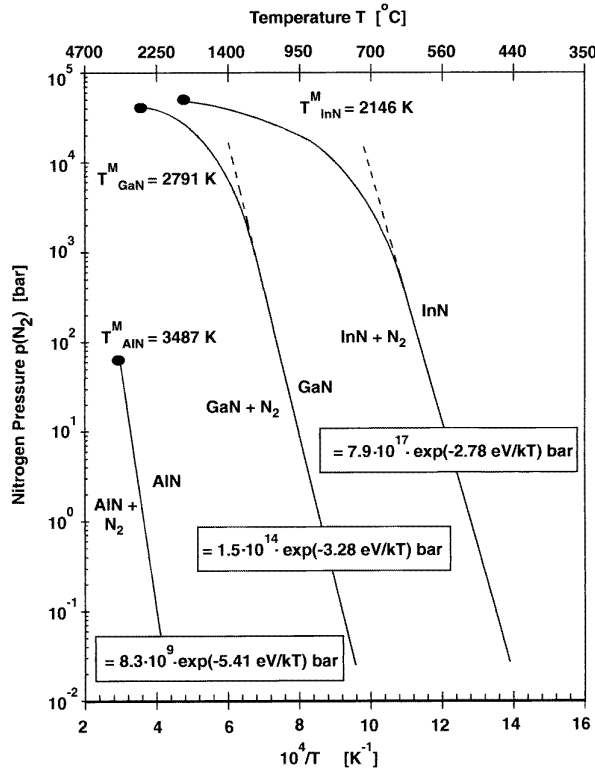


**Figure 8.** Equilibrium  $N_2$  pressure over the  $MN(s) + M(l)$  systems ( $M = \text{In, Ga or Al}$ ), and melting points  $T^M$  from high-pressure experiments and theoretical calculations [48–60].

exist in a ( $H_2 + NH_3$ ) gas mixture streaming over Ga and GaN. They determined the equilibria both in the case of formation and decomposition of GaN. Lorenz and Binkowski [55] observed the decomposition at given temperatures by measuring the time dependence of the increase in  $N_2$  pressure. An extensive study on the thermal stability of GaN at high temperatures and pressures up to 60 kbar has been performed by Karpinsky *et al* [56], using a gas pressure technique and a tungsten carbide anvil cell. In the high-pressure range, the  $p(1/T)$  curve strongly deviates from the linear dependence proposed by Thurmond and Logan (figure 8), but there is good agreement in the Gibbs free enthalpy with  $\Delta G^0 = (32.43T - 3.77 \times 10^4)$  cal/mol for GaN synthesis. The value of enthalpy  $\Delta H^0$  of  $-37.7$  kcal/mol is in good agreement with the value estimated by Madar *et al* [57].

Resistively heated graphite filaments were used by Class [58] to evaluate the melting behaviour and temperature of AlN. The melting of AlN was observed at 2750–2850 °C, at nitrogen pressures of 100 and 200 bar. Slack and McNelly [59] calculated  $N_2$  pressures over AlN in equilibrium with liquid Al to be 1, 10 and 100 bar at 2563 °C, 2815 °C and 3117 °C respectively. The melting temperatures for different nitrides were evaluated by Van Vechten [60] with the use of a semi-empirical theory for electronegativity, concluding that the melting point of AlN is close to 3487 K. Figure 8 summarizes the results of the theoretical calculations and experiments described above, including the melting temperatures.

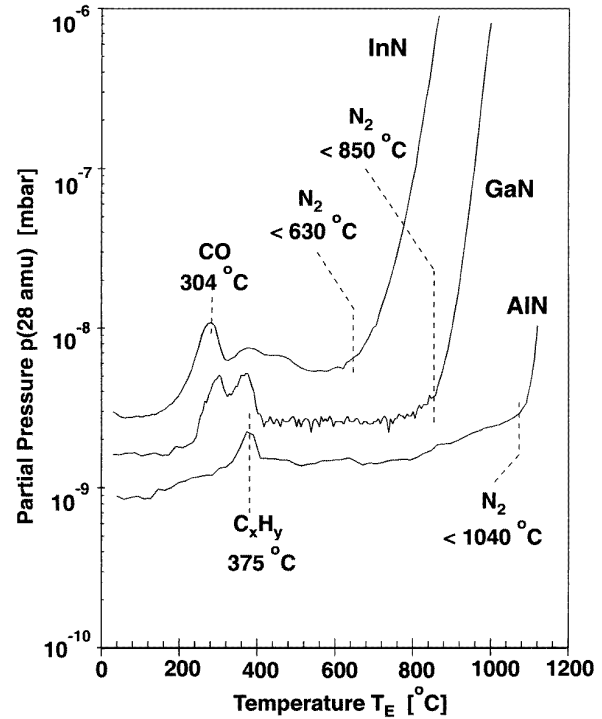


**Figure 9.** The partial pressure of mass 28 amu ( $N_2^+$ ,  $CO^+$ ,  $C_2H_4^+$ ) versus effusion or decomposition temperature  $T_E$ . The decomposition of InN, GaN and AlN is observed above 630 °C, 850 °C and 1040 °C respectively [61].

To quantitatively determine and compare the thermal stability of thin films, the desorption and decomposition of polycrystalline InN deposited at 550 °C, and epitaxial GaN and AlN grown at 950 °C and 1050 °C were measured by heating the samples in vacuum and recording the partial pressure of relevant gases using a quadrupole mass spectrometer [61]. For a known heating routine, the desorption spectra can be analysed to find the binding energies of various desorbed species as well as the thermal stability of the sample [62]. Figure 9 shows the partial pressure of mass 28 amu ( $N_2^+$ ,  $CO^+$ ,  $C_2H_4^+$ ) versus effusion or decomposition temperature  $T_E$ . The nitrogen partial pressure increases exponentially above  $T_E = 630$  °C, 850 °C and 1040 °C for InN, GaN and AlN respectively, illustrating that the decomposition temperature in vacuum is much lower than the melting point. To determine the effective decomposition activation energy more precisely, the nitrogen flux was calculated from the measured nitrogen pressure. The rate of nitrogen evolution  $\Phi(N)$  is equal to the rate of decomposition, and the slope of  $\ln[\Phi(N)]$  versus  $1/T$  (figure 10) gives the effective activation energy of the decomposition in vacuum  $E_{MN}$ . The decomposition rate equals the desorption of one monolayer every second ( $\Phi(N) = 1.5 \times 10^{15} \text{ cm}^{-2} \text{ s}^{-1}$ ) at 795, 970 and 1050 °C, and the activation energy of the thermally induced decomposition is determined to be  $E_{MN} = 3.5$  eV (336 kJ mol $^{-1}$ ), 3.9 eV (379 kJ mol $^{-1}$ ) and 4.3 eV (414 kJ mol $^{-1}$ ) for InN, GaN and AlN respectively (table 4). This indicates temperature limits for high-temperature or high-power devices.

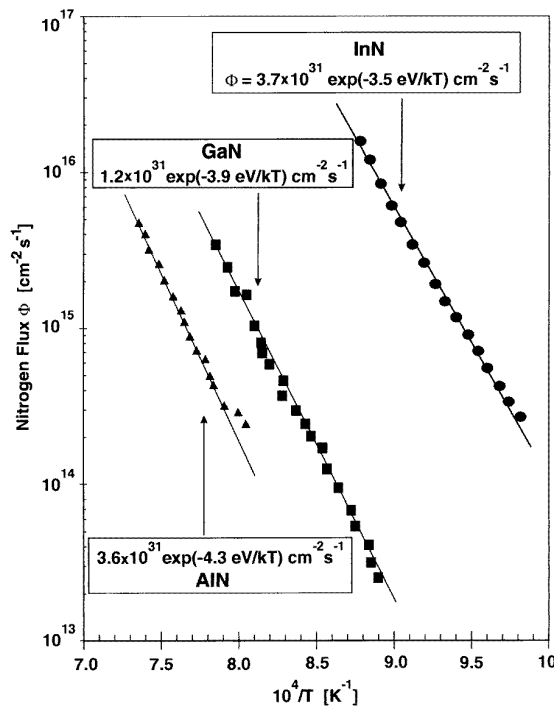


**Figure 10.** Nitrogen flux or desorption rate for InN, GaN and AlN in the temperature range of decomposition. The rate of N evolution is equal to the rate of decomposition and the slope of  $\ln[\Phi(N)]$  versus  $1/T$  gives the effective activation energy  $E_{MN}$  of the decomposition in vacuum [61].

**Table 4.** Density  $\rho$ , melting point  $T^M$ , decomposition temperature  $T_E$  and activation energy  $E_{MN}$  of the decomposition of InN, GaN and AlN ( $p < 10^{-6}$  mbar).

	$\rho^a$ (g cm $^{-3}$ )	$T^M$ <sup>a</sup> (K)	$T_E$ <sup>b</sup> (°C)	$E_{MN}$ <sup>b</sup> (kJ mol $^{-1}$ )
AlN	3.29	3487	1040	414
GaN	6.07	2791	850	379
InN	6.81	2146	630	336

<sup>a</sup> From [17].

<sup>b</sup> From [61].

In connection with the thermal stability of hexagonal nitrides, the thermally activated nitrogen self-diffusion should be mentioned. Nitrogen diffusion is a fundamental transport process in Group III-nitrides. In general, self-diffusion processes in wide-bandgap semiconductors or insulators are more complex than in metals [63]. This is due to the large variety of native defects, different possible charge states of defects, and to the much larger effects of small concentrations of defects on the Fermi level position [64]. Diffusion processes also play an important role in device fabrication and the thermal stability of high-power devices [65]. Diffusion of dopants is utilized to engineer p–n junctions and transistor structures [66]. In other cases, diffusion can be destructive to delicate structures due to the transport of dopants from thin layers into the adjacent layers or the substrate.

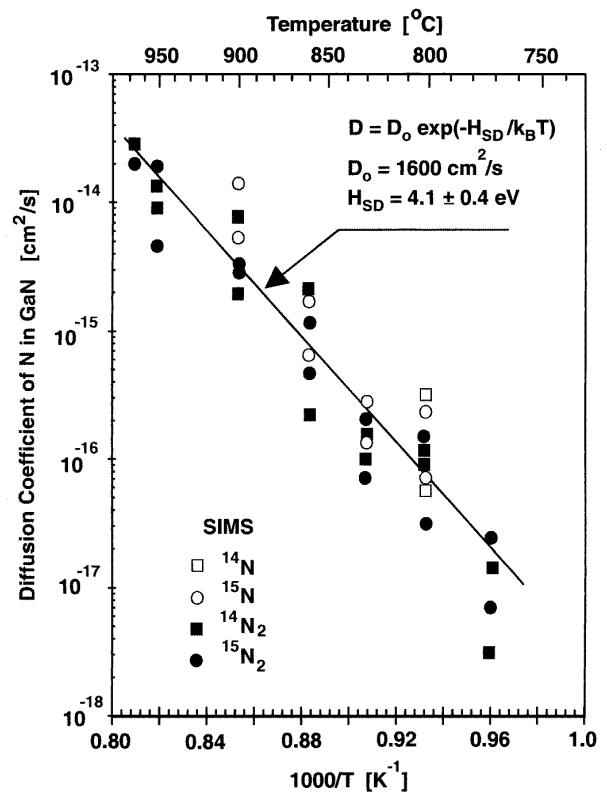


**Figure 11.** Arrhenius plot of the measured nitrogen self-diffusion coefficient in hexagonal GaN, obtained at temperatures between 770 and 970 °C. The diffusion coefficients were calculated from the concentration depth profiles determined from SIMS signals of  $^{14}\text{N}$  (open squares),  $^{15}\text{N}$  (open circles),  $^{14}\text{N}_2$  (full squares) and  $^{15}\text{N}_2$  (full circles). The line represents a least-squares fit to the measured data.

In III–V compounds, diffusion measurements are difficult to perform because of the high partial vapour pressure of the Group V elements and the dependence of native defect species and concentrations on stoichiometry. Goldstein [67] and Palfrey *et al* [68] diffused radioactive  $^{72}\text{Ga}$  into bulk GaAs to study Ga self-diffusion. The measurement of the depth profile of  $^{72}\text{Ga}$  was realized by mechanical sectioning and determination of the radioactivity. Within the temperature range investigated, the authors reported activation enthalpies varying between 2.6 and 5.6 eV. Wang *et al* [69] grew and studied an isotopically tagged  $^{69}\text{GaAs}/^{71}\text{GaAs}$  heterostructure. Upon heating between 800 and 1225 °C under an As-rich condition, the Ga diffusion coefficient  $D$  was determined by secondary ion mass spectrometry (SIMS) to be  $D(\text{Ga}) = (43 \pm 25) \text{ cm}^2 \text{ s}^{-1} \exp[(-4.24 \pm 0.06) \text{ eV } k_B^{-1} T^{-1}]$  over six orders of magnitude in  $D$ .

In analogy to that experiment, nitrogen self-diffusion was studied by using  $\text{Ga}^{14}\text{N}/\text{Ga}^{15}\text{N}/\text{Ga}^{14}\text{N}$  (500/500/500 nm) isotopic heterostructures grown on *c*-plane sapphire by PIMBE [70]. Concentration profiles of nitrogen isotopes after annealing were measured using SIMS. The activation enthalpy and entropy of nitrogen self-diffusion were obtained by analysing the diffusion length measured for annealing temperatures between 770



and 970 °C. The characteristic diffusion length  $l$  is defined as

$$l = 2\sqrt{Dt} \quad (9)$$

where  $D$  is the nitrogen self-diffusion coefficient and  $t$  is the annealing time. The diffusion coefficients of nitrogen are shown on an Arrhenius plot to determine the activation energy of the diffusion process in figure 11. If the self-diffusion is dominated by one thermally activated process, the coefficient  $D$  can be written as

$$D = D_0 \exp\left(-\frac{H_{SD}}{k_B T}\right) \quad (10)$$

where  $H_{SD}$  is the self-diffusion enthalpy and  $D_0$  is the pre-exponential factor. The measured  $D$  values span three orders of magnitude in the temperature range from 770 to 970 °C, resulting in an activation enthalpy of  $4.1 \pm 0.4$  eV and a pre-exponential factor of  $1600 \text{ cm}^2 \text{ s}^{-1}$ .

By analysing the dependence of the self-diffusion coefficient on temperature and the measured gradients in concentrations of  $^{14}\text{N}$  and  $^{15}\text{N}$ , the nitrogen flux  $\Phi_{SD}(\text{N})$  through the interfaces of the  $\text{Ga}^{14}\text{N}/\text{Ga}^{15}\text{N}/\text{Ga}^{14}\text{N}$  heterostructures was calculated using

$$\Phi_{SD}(\text{N}) = -D \frac{dC(\text{N})}{dx} \quad (11a)$$

$$= 3.8 \times 10^{30} \text{ cm}^{-2} \text{ s}^{-1} \exp\left(\frac{-4.1 \text{ eV}}{k_B T}\right) \quad (11b)$$

where  $dC(\text{N})/dx$  is the gradient in the concentration of  $^{14}\text{N}$  or  $^{15}\text{N}$  close to the interface. In the temperature range between 850 and 950 °C, the nitrogen flux through a GaN isotope interface is a factor of  $14 \pm 2$  lower than the nitrogen flux from a free GaN surface into vacuum. Within the accuracy of the measurements, the nitrogen diffusion process has the same activation energy as the decomposition process of GaN. There are at least three possible explanations for these findings as follows.

(i) Thermally induced decomposition in vacuum and the diffusion of nitrogen atoms in GaN are limited by the same processes which can be Ga–N bond breaking and/or nitrogen migration.

(ii) During the thermal decomposition of GaN, a high concentration of defects, which significantly enhance the diffusion process, could be created close to the sample surface.

(iii) The observed self-diffusion and decomposition may be dominated by nitrogen effusion and transport along one- or two-dimensional structural defects such as nanotubes or dislocations.

To clarify which kind of diffusion process dominates, further experiments are needed. The observed diffusion processes, thermal stability and the nitrogen loss from the surface of the Group III-nitrides have a strong influence on the growth mechanism and on the conditions under which epitaxial films and small crystals can be produced. The different methods for this are discussed next.

#### 4. Growth of Group III-nitride films and crystals

The history of the production of Group III-nitrides covers more than a century. AlN powder was first made in 1862 from liquid Al and  $\text{N}_2$  gas [71]. The major difficulty with this direct reaction method is that the surface film of AlN on Al is very adherent and impedes further reaction. In another technique, AlN powder can be formed from Al electrodes in a direct current arc [72]. This produces only small amounts of AlN per day and the powder usually has several per cent excess aluminium because even here the AlN skin is protective. A more useful method for making AlN is to react  $\text{AlF}_3$  powder with  $\text{NH}_3$  gas at high temperatures [73]. The overall chemical reaction at 1000 °C is:



In order to promote the formation of AlN, it is necessary to keep the  $\text{NH}_3$  partial pressure above 1 bar and the HF gas must be continually removed. At 1 atm pressure, a minimum of 25 molecules of  $\text{NH}_3$  are needed for each AlN molecule produced [59].

The earliest investigations of GaN powder were reported by Johnson and co-workers [74], who described the conversion of metallic Ga in a  $\text{NH}_3$  stream by the chemical reaction:



They obtained a black powder by flowing ammonia over metallic gallium at 1000 °C. Ejder contained Ga in an open sintered alumina boat [75]. The boat was placed in a silica glass tube in a tube furnace, and a mixture of nitrogen and ammonia was passed over the boat. The reaction between Ga and  $\text{NH}_3$  started below 1000 °C and the thin crust of GaN which formed on the surface of the molten Ga then decreased the rate of further GaN formation by lowering the evaporation rate of Ga from the metal surface. By this method whiskers, needles and prisms (sizes up to 500  $\mu\text{m}$ ) were formed on the edges of the boat and on the walls of the surrounding silica glass tube.

These early growth processes and investigations resulted in AlN and GaN powders and very small crystals which were used to determine basic physical properties like crystal structure, lattice constants and optical properties. These results enabled the identification of substrate materials suitable for the heteroepitaxy of Group III-nitrides.

##### 4.1. Substrates for heteroepitaxy

One particular difficulty in the growth of thin films is the unavailability of sufficiently large ( $>1$  cm) single crystals for use as substrates for homoepitaxial growth. Thus up to now, heteroepitaxial growth is a practical necessity and the choice of substrate is critical. This problem is well recognized and there have been a number of studies on the effects of the substrate on the structural, electrical and morphological properties of thin films of these compound semiconductors [76–88].

Possible substrate materials with low thermal expansion and lattice mismatch for vapour phase epitaxy (VPE)

and MOCVD are limited to those unaffected by high concentrations of ammonia and hydrogen at temperatures in excess of 1000 °C. This limits the use of Si, GaAs and GaP, if no low-temperature buffer layer can be grown as a first step of device fabrication. Even for PIMBE, in which the growth temperatures are about 250 °C lower than for VPE and MOCVD, the substrate surfaces have to be stable under the influence of nitrogen radicals at 800 °C. For device production processes, the substrate of choice has to be available in a minimum size of two inches, with atomically flat surfaces, and in large quantities at acceptable prices.

Under the presuppositions mentioned above, sapphire and silicon carbide are the most popular substrate materials. Although sapphire ( $\alpha$ - $\text{Al}_2\text{O}_3$ ) has a rhombohedral structure, it can be described by a hexagonal cell that is larger than the basic rhombohedral unit cell. To date, four orientations of sapphire have been used as substrates:  $(10\bar{1}0)$ ,  $(0001)$ ,  $(2\bar{1}10)$  and  $(11\bar{2}0)$ . The lattice mismatch between GaN and  $(0001)$  sapphire is 13.9%, as shown in table 5. This table also includes the thermal expansion mismatch which is just as important for epitaxial growth. For various commercially available sapphire orientations, the relationship of orientation, lattice mismatch and crystallographic symmetry with a GaN epitaxial film are given (figure 12). From the viewpoints of lattice mismatch and crystal symmetry,  $(10\bar{1}0)$  sapphire (*m*-plane) seems the most suitable for GaN growth. However, the *c*-axis of a GaN film grown on a  $(10\bar{1}0)$  sapphire substrate has a nonzero inclination with respect to the *c*-axis of the sapphire substrate. This means that twins may be generated. This is a major disadvantage of a  $(10\bar{1}0)$  plane compared to a  $(0001)$  plane.

Because of the high in-plane lattice mismatch (up to -29%) between the  $(0001)$  oriented films of InN, GaN and AlN and the  $(0001)$  sapphire, it seems surprising that epitaxial growth is possible. Transmission electron microscopy (TEM) was used to investigate the epitaxial growth of hexagonal GaN by MBE on the  $(0001)$  basal plane of  $\text{Al}_2\text{O}_3$ . The in-plane orientation obtained between layer and substrate gives a high lattice misfit of -13.9%, which induces a stress relaxation process directly in the interface region. High resolution TEM (HRTEM) images reveal  $\{11\bar{2}0\}_{\text{sapphire}}$  lattice fringes terminating at the interface between GaN and  $\text{Al}_2\text{O}_3(0001)$  [79]. Because the Burgers vectors of misfit dislocations are parallel to the  $(0001)$  interface plane, gliding is limited to the  $(0001)$  planes and therefore these misfit dislocations are confined at the interface. This interfacial relaxation process is very effective and the extension of dislocations into the GaN layer is suppressed. In the case of pseudomorphic growth the number of  $\{10\bar{1}0\}_{\text{GaN}}$  lattice fringes is expected to be the same as the number of  $\{11\bar{2}0\}_{\text{sapphire}}$  lattice fringes. The plastic relaxation of GaN by the formation of misfit dislocations leads to a termination of  $\{11\bar{2}0\}_{\text{sapphire}}$  lattice fringes at the interface. The quantitative evaluation of Fourier-filtered HRTEM images (figure 13) reveals an average of  $8.3 \pm 0.7$   $\text{Al}_2\text{O}_3$  lattice spacings between two terminating  $\{11\bar{2}0\}_{\text{sapphire}}$  fringes. By forming a coincidence lattice between GaN and  $\text{Al}_2\text{O}_3$ , a large

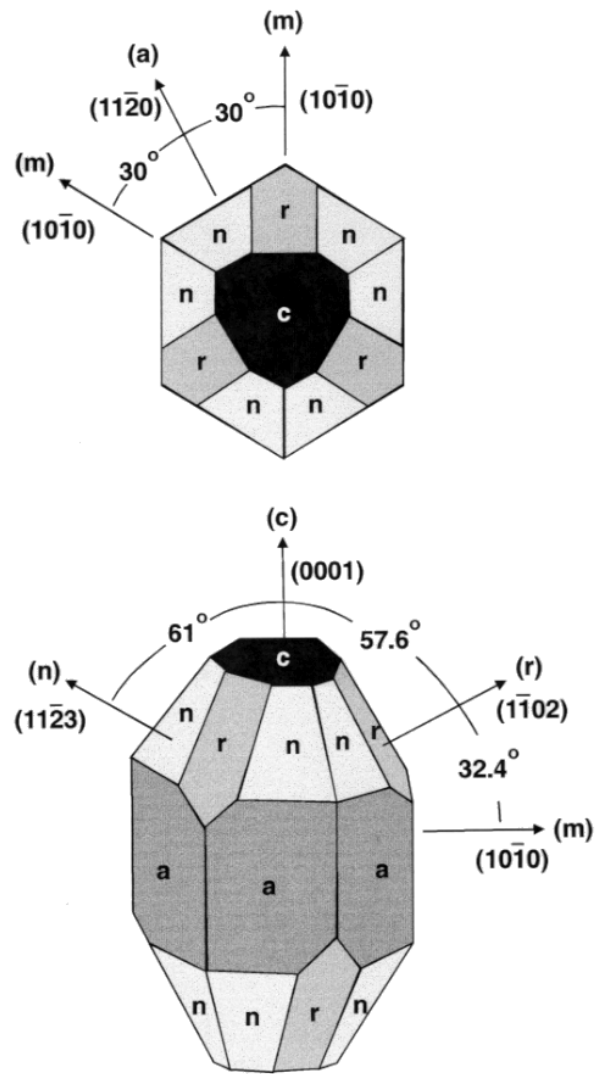


**Figure 12.** Rhombohedral structure and surface planes of sapphire.

portion (-11.8%) of the high mismatch is compensated by dislocations confined at the interface. The relaxation process allows an epitaxial growth of GaN on  $(0001)\text{Al}_2\text{O}_3$  with a density of non-confined dislocations of about  $10^{10} \text{ cm}^{-2}$  in the GaN. The non-confined dislocations are caused by the residual strain reduction from -2.1% measured near the interface to -0.2% obtained at the surface for a 1  $\mu\text{m}$  thick GaN film. The lattice constant  $a(\text{GaN}) = 3.1892 \text{ \AA}$  in the surface region reveals a residual strain of -0.2% in the GaN film after growth. With thermal expansion coefficients perpendicular to the *c*-axis of  $5.6 \times 10^{-6} \text{ K}^{-1}$  for GaN and  $7.3 \times 10^{-6} \text{ K}^{-1}$  for  $\text{Al}_2\text{O}_3$  (table 6), a lattice misfit of -13.75% can be calculated for a growth temperature of 800 °C. Cooling of the sample from growth temperature to room temperature causes a film strain of -0.12%, which is similar to the measured surface strain. Consequently it can be concluded that at the growth temperature, the film is almost completely relaxed and the residual strain close to the surface is only a thermal effect.

**Table 5.** Lattice mismatch and thermal expansion mismatch of different sapphire surface orientations with GaN.

Al <sub>2</sub> O <sub>3</sub> surface plane	Interface plane	In-plane	Lattice mismatch (%)	Thermal expansion mismatch (%)
	GaN Al <sub>2</sub> O <sub>3</sub>	GaN  Al <sub>2</sub> O <sub>3</sub>		
<i>m</i>	(01 $\bar{1}$ 3) (01 $\bar{1}$ 0)	[03 $\bar{3}$ 2]  [2 $\bar{1}$ $\bar{1}$ 0]	−2.6	9
		[2 $\bar{1}$ $\bar{1}$ 0]  [0001]	1.9	62
<i>c</i>	(0001) (0001)	[2 $\bar{1}$ $\bar{1}$ 0]  [01 $\bar{1}$ 0]	−13.9	−25.5
		[01 $\bar{1}$ 0]  [2 $\bar{1}$ $\bar{1}$ 0]	−13.9	
<i>a</i>	(0001) (2 $\bar{1}$ $\bar{1}$ 0)	[01 $\bar{1}$ 0]  [01 $\bar{1}$ 0]	−0.4	1.9
		[2 $\bar{1}$ $\bar{1}$ 0]  [0001]	1.9	
<i>r</i>	(2 $\bar{1}$ $\bar{1}$ 0) (01 $\bar{1}$ 2)	[01 $\bar{1}$ 0]  [2 $\bar{1}$ $\bar{1}$ 0]	13.8	1.1
		[0001]  [0 $\bar{1}$ 11]	1.1	

**Table 6.** Space group symmetry, lattice constants and thermal expansion coefficients for substrate materials which are used for the growth of epitaxial GaN films.

Substrate	Space group symmetry	Lattice constants (Å)	Thermal expansion coefficient (10 <sup>−6</sup> K <sup>−1</sup> )
$\alpha$ -GaN	P6 <sub>3</sub> mc	$a_0 = 3.189$ $c_0 = 5.185$	5.59 3.17
$\beta$ -GaN	F $\bar{4}$ 3m	$a_0 = 4.52$	?
Al <sub>2</sub> O <sub>3</sub>	R $\bar{3}c$	$a_0 = 4.7589$ $c_0 = 12.991$	7.3 8.5
6H-SiC	P6 <sub>3</sub> mc	$a_0 = 3.0806$ $c_0 = 15.1173$	4.46 4.16
3C-SiC	F $\bar{4}$ 3m	$a_0 = 4.3596$	3.9
Si	Fd $\bar{3}$ m	$a_0 = 5.43088$	3.59
GaAs	F $\bar{4}$ 3m	$a_0 = 5.652$	6.0
MgO	Fm $\bar{3}$ m	$a_0 = 4.216$	10.5
MgAl <sub>2</sub> O <sub>4</sub>	Fd $\bar{3}$ m	$a_0 = 8.083$ $a_0 = 5.431$	7.45 11.9
NdGaO <sub>3</sub>	Orthorhombic	$b_0 = 5.499$ $c_0 = 7.710$	6.6 5.8
$\gamma$ -LiAlO <sub>2</sub>	P4 <sub>1</sub> 2 <sub>1</sub> 2	$a_0 = 5.169$ $c_0 = 6.268$	15 7.1
LiGaO <sub>2</sub>	Pna2 <sub>1</sub>	$a_0 = 5.4063$ $b_0 = 6.3786$ $c_0 = 5.0129$	6 9 7
ZnO	P6 <sub>3</sub> mc	$a_0 = 3.252$ $c_0 = 5.213$	2.9 4.75

A model based on this observation can be inferred. During the initial growth process of the first monolayers, only confined misfit dislocations are generated before the entire substrate is covered with GaN. These dislocations originate at island borders and then start to glide beneath the islands. The occurrence of islands or of a rough surface during the initial growth can be expected in most highly mismatched heterostructures and this leads to three-dimensional island growth and films consisting of a mosaic (typical grain sizes of the order of a few hundred ångströms to a few micrometres) of columnar grains. The confined dislocations lead to a relaxation of a large part of the misfit and a minor strain of −2.1%. This residual strain is comparable to the lattice misfit between 6H-SiC and GaN, possibly explaining why GaN grown directly on both substrates contains comparable dislocation densities of about 10<sup>10</sup> cm<sup>−2</sup>.

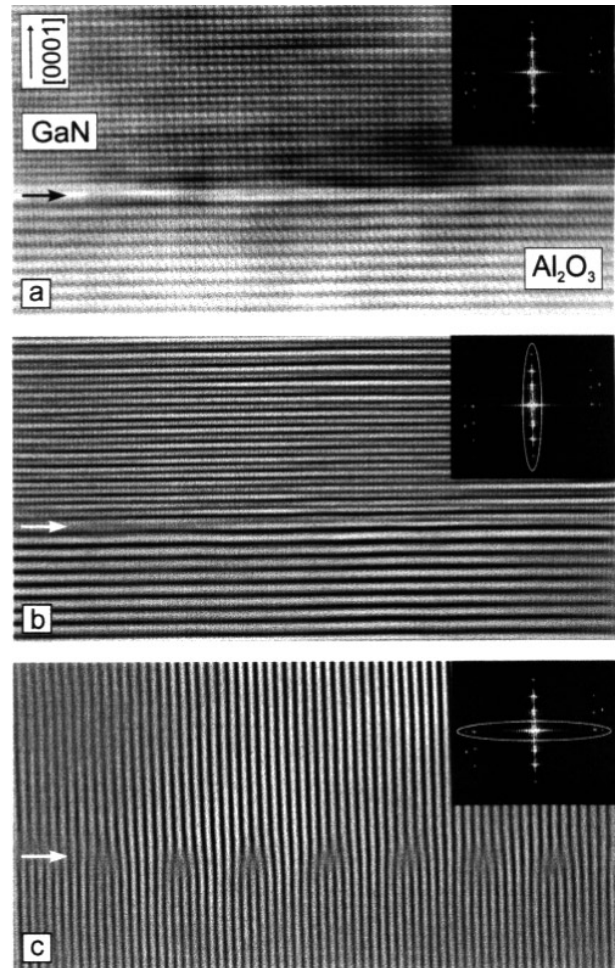


**Figure 13.** (a) HRTEM image of the GaN/Al<sub>2</sub>O<sub>3</sub> (0001) interface region in {1 $\bar{2}$ 10}GaN and {1100}Al<sub>2</sub>O<sub>3</sub> projection. The insert shows the intensity plot of the corresponding Fourier-transformed image. (b) shows the (0001) lattice planes of GaN and Al<sub>2</sub>O<sub>3</sub> without any recognizable plane bending or termination in the interface region. (c) Image after Fourier-filtering of the perpendicular direction. At the interface some {1120}Al<sub>2</sub>O<sub>3</sub> fringes terminate at regular intervals. In the inserts of (b) and (c) the selected area of the Fourier-transformed image which is used for the subsequent reconstruction is marked.

A first step in the improvement of device applicability of Group III-nitrides deposited on (0001) sapphire would

be to alter the film growth processes, to the exclusion of columnar islands and secondary grain growth. It is well accepted that surface nitridation of sapphire and the growth of low-temperature nucleation layers can alter the growth process and film qualities. Recent examples of heteroepitaxy mediated by buffer layers include the growth of smooth films of GaN with high carrier mobilities and light-emitting devices on AlN-buffered (0001) sapphire as discussed later on.

To overcome the large lattice mismatch between GaN and  $\text{Al}_2\text{O}_3$ , Fischer and co-workers used  $\text{LiAlO}_2$  substrates with 1.5% lattice mismatch and 21% mismatch in the thermal expansion coefficients respectively [80]. The epitaxy relationships between GaN and  $\text{LiAlO}_2$  are expected to be (0110)/(100)  $\text{LiAlO}_2$  with  $[2\bar{1}\bar{1}0]/[001]$   $\text{LiAlO}_2$ . Unlike  $\text{Al}_2\text{O}_3$  and 6H-SiC substrates with very smooth surfaces, the  $\text{LiAlO}_2$  substrate exhibited a wave-like surface with equidistant grooves about 10 nm deep, which could have originated from the mechanical surface polishing. Because of the high surface roughness, the interface between GaN and  $\text{LiAlO}_2$  was highly defective and caused three-dimensional growth of the GaN.

MOCVD of monocrystalline GaN thin films on  $\beta$ - $\text{LiGaO}_2$  substrates was realized by Kung *et al* [81]. The structure of  $\text{LiGaO}_2$  is similar to the wurtzite structure, but because Li and Ga have different ionic radii, the crystal has orthorhombic structure. The atomic arrangement in the (001) face is hexagonal, which promotes the epitaxial growth of (0001) GaN, so that the epitaxial relationship (0001)GaN/(001) $\text{LiGaO}_2$  is expected. The distance between the nearest cations in  $\text{LiGaO}_2$  is in the range of 3.133–3.189 Å, while the distance between nearest anions is in the range of 3.021–3.251 Å. The lattice mismatch between (0001) GaN on (001)  $\text{LiGaO}_2$  is then only 1–2%. The GaN layers were grown by MOCVD at temperatures between 600 and 1000 °C, at deposition rates of about  $0.7 \mu\text{m h}^{-1}$ . The samples had smooth surfaces and the x-ray rocking curve was as narrow as 300 arcsec, for substrate temperatures of 900 °C. All GaN layers were n-type ( $n_e \approx 10^{20} \text{ cm}^{-3}$ ) as determined by room-temperature Hall measurements. The electron mobility was about  $10 \text{ cm}^2 \text{ V}^{-1} \text{ s}^{-1}$ . The high electron concentrations may be due to the incorporation of oxygen, resulting from the decomposition of  $\text{LiGaO}_2$  at elevated substrate temperatures. This effect would probably be reduced by the use of low-temperature buffer layers.

The lattice mismatch of GaN to  $\text{NdGaO}_3$  has been calculated to be 1.2%. This material, with an orthorhombic crystal structure, has been regarded as pseudocubic because the lattice constants along the *a*- and *b*-axes are almost the same. The mismatch in the thermal expansion coefficients, however, is approximately 20%. GaN films were grown on  $\text{NdGaO}_3$  (011) by hydride VPE at 810 and 850 °C using  $\text{NH}_3$  and HCl+Ga as source gases [82]. The best results were obtained for GaN grown at a low growth rate after nitridation of the substrate surface. GaN (0001) films were confirmed by x-ray diffraction (XRD) measurements to grow along the *c*-axis with good lattice match to the substrate, as observed by TEM.

The deposition of single crystal wurtzite GaN films on cubic (111) and (001) spinel ( $\text{MgAl}_2\text{O}_4$ ) substrates

was reported by Kuramata *et al* [83], George *et al* [84] and Sun *et al* [85]. Kuramata and co-workers used MOCVD with trimethylgallium and ammonia and a 30 nm thick GaN buffer layer grown at 500 °C. The morphology of thick epitaxial GaN films deposited at 1030 °C on (111)  $\text{MgAl}_2\text{O}_4$  was specular, while the morphology of GaN on (001)  $\text{MgAl}_2\text{O}_4$  was very rough. From XRD measurements, the GaN film was found to be (0001) oriented. The crystallographic orientation relationships between the GaN and the  $\text{MgAl}_2\text{O}_4$  substrate are as follows: (0001)GaN//[(111) $\text{MgAl}_2\text{O}_4$ , (1100)GaN//( $\bar{2}$ 11) $\text{MgAl}_2\text{O}_4$ . The FWHM value of x-ray rocking curves for a  $3.6 \mu\text{m}$  thick film was 310 arcsec, which is significantly larger than the values reported for GaN deposited on sapphire.

Hellman *et al* reported preliminary results for the use of  $\text{ScAlMgO}_4$  as a substrate for hexagonal GaN [86]. The congruent melting of  $\text{ScAlMgO}_4$  makes Czochralski growth possible, so large high-quality substrates can be realized. Boules of 17 mm in diameter have already been fabricated. The low misfit (+1.8%) allows coherent epitaxy of GaN. The authors used nitrogen plasma induced molecular beam epitaxy (section 4.6). Near-bandgap photoluminescence was observed from some films grown with deposition rates in the range between 0.035 and  $0.5 \mu\text{m h}^{-1}$  at substrate temperatures of 600 to 650 °C. The FWHM of the XRD rocking curves, about 30 arcmin, indicates that the structural properties of the substrate and the epitaxial GaN film have to be improved.

Use of substrates other than GaN presents not only the disadvantages of lattice and thermal mismatch, but also the possibility of unintentional contamination from the substrate during growth. The presence of high concentrations of structural defects in GaN (especially dislocations, grain and twin boundaries) enhances the diffusion of impurities. Contamination of GaN by impurities emanating from  $\text{Al}_2\text{O}_3$ , SiC, and ZnO substrates has been studied by SIMS analysis [87]. The epitaxial GaN films were deposited at 800 °C by gas source MBE using 60–80 nm thick AlN buffer layers. For growth times of 6 h (deposition rate  $\approx 0.5 \mu\text{m h}^{-1}$ ), Al and O concentrations above  $5 \times 10^{17} \text{ cm}^{-3}$  were detected over a range of  $1 \mu\text{m}$  from the interface. The thickness of the Si-contaminated GaN layer grown on a SiC substrate for the same deposition time was found to be  $0.8 \mu\text{m}$ . The diffusion lengths of Zn and O from a ZnO substrate were 200 nm at 800 °C for a growth time of 2 h. These measurements demonstrate that even relatively stable substrate materials like  $\text{Al}_2\text{O}_3$  and SiC are sources of impurities (n-dopants such as O and Si) for the interfacial GaN layer. Because of the higher growth temperatures, this effect has to be expected to be much stronger for VPE processes.

Today sapphire and SiC substrates predominate the heteroepitaxial growth of Group III-nitrides, due to their adequate (although incomplete) thermal and chemical stability at high growth temperatures, excellent structural and surface morphology and availability in large quantities. For the fabrication of light-emitting diodes (LEDs), sapphire has the advantages of being transparent up to 8.8 eV, relatively cheap and available in substrate sizes up to  $6 \text{ in}^2$ . In addition, sapphire substrates are

of interest for the fabrication of surface acoustic wave devices (AlN/Al<sub>2</sub>O<sub>3</sub> heterostructures) because of the high resistivity and the large acoustic wave velocity of about 5600 m s<sup>-1</sup> (section 9.1). 6H-SiC is of increasing interest because of its small lattice mismatch to AlN, the good thermal conductivity and the possibility of n- and p-type doping. For high-temperature and high-power devices like transistors and detectors for high UV irradiation, SiC is the substrate material of choice. Whether alternative substrates could replace sapphire or SiC will depend on the improvements in the crystal growth techniques and polishing procedures, and on whether sapphire and SiC substrates become a limiting factor in producing high-quality optical and electrical devices.

## 4.2. Vapour phase epitaxy (VPE)

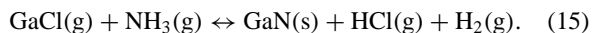
**4.2.1. Vapour phase epitaxy of GaN.** VPE of GaN has a long history and has been widely used because of its high growth rates of up to a few tens of micrometres per hour and its lack of carbon incorporation into the film. Hydride vapour phase epitaxy (HVPE) is attracting renewed interest as a technique for quasibulk materials to provide lattice-matched growth surfaces and thick, strain-relieved buffer layers [89]. The high growth rate offers the possibility of preparing very thick films, which can even be removed from a Al<sub>2</sub>O<sub>3</sub> substrate by polishing or laser-induced thermal decomposition [88] and used as a substrate for homoepitaxy.

In conventional chloride transport VPE of GaN, the Ga source is gallium monochloride (GaCl), which is only stable at temperatures above 600 °C and is produced by the reaction of liquid gallium with hydrogen chloride (HCl) gas. The supply of GaCl is controlled by the Ga cell temperature and the flow rates of the HCl and the carrier gas. The source for nitrogen is ammonia gas, often diluted with a carrier gas [89]. For the widely investigated Ga/HCl/AsH<sub>3</sub>/H<sub>2</sub>, Ga/AsCl<sub>3</sub>/H<sub>2</sub> as well as Ga/HCl/AsH<sub>3</sub>, PH<sub>3</sub>/H<sub>2</sub> systems, several arguments support the assumption of the growth rate being limited by the desorption of chlorine from the growing surface [90–92]. For this process, an activated surface complex involving hydrogen has been considered. In VPE of GaN, with the analogous Ga/HCl/NH<sub>3</sub>/H<sub>2</sub> system, Seifert and co-workers studied the rate limiting steps for the deposition process [92]. The reactor was heated by a two-zone resistance furnace. The Ga source was held at a constant temperature between 850 and 900 °C. Titration of unreacted HCl revealed the conversion efficiency to be between 95 and 96% for the reaction:

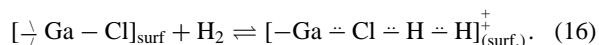


Typical flow rates for HCl, NH<sub>3</sub> and the carrier gas were 15 sccm, 1000 sccm and 2000 sccm respectively. GaN was grown with rates up to 900 μm h<sup>-1</sup> on (10 $\bar{1}$ 2) Al<sub>2</sub>O<sub>3</sub> substrates at atmospheric pressure. The variation of deposition (growth) rate  $r_{\text{dep}}$  as a function of reciprocal substrate temperature  $T_s$  is shown in figure 14. In analogy to the growth rate in VPE of other III–V compounds, there is a temperature (≈950–1050 °C)

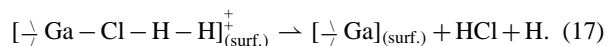
for maximum growth rate. At lower temperatures, the growth rate decreases exponentially due to the decreasing efficiency of the GaCl and NH<sub>3</sub> pyrolysis. At higher temperatures, thermodynamically predicted thermal-induced decomposition is observed and the rate decreases. This is especially evident for growth in a hydrogen ambient. One reason could be the formation of GaH<sub>x</sub> molecules at high deposition temperatures, which is discussed in more detail in section 4.5. The input partial pressure of NH<sub>3</sub> does not significantly influence the growth rate above the generally used pressures around 100 mbar. The growth rate depends approximately linearly on the input partial pressure of GaCl and the deposition of GaN can be described by the overall reaction



A calculation of the thermodynamic equilibrium partial pressures (including the six species HCl, GaCl, NH<sub>3</sub>, GaCl<sub>3</sub>·NH<sub>3</sub>, H<sub>2</sub>, and He) shows that in the temperature region above 800 °C (figure 15), the only Ga species which should be of importance is GaCl; whereas with decreasing temperatures, molecules of GaCl<sub>3</sub>·NH<sub>3</sub> must also be taken into consideration. For a qualitative understanding of the surface kinetics during VPE of GaN at substrate temperatures above 800 °C, Seifert *et al* proposed the following model. It is inferred that the rate-determining step is the formation of an activated complex containing Ga, Cl and H:



The growth rate of GaN is then given by the rate of activated surface complex molecules irreversibly decomposing



The surface-adsorbed Ga atom is then available for further adsorption of N species. This adsorption process should be fast, and not a rate limiting step, because of the high excess of NH<sub>3</sub> in the vapour phase. The hydrogen partial pressure determines the concentration of the activated complex molecules on the growing surface. From this it follows that a reduced hydrogen partial pressure reduces the growth rate, as was also observed in GaAs VPE [94].

Gallium trichloride (GaCl<sub>3</sub>) has also been used as the Ga source, due to its high vapour pressure [95,96]. Hasegawa [96] used an open flow horizontal quartz tube with a single-zone hot wall furnace as the reactor. The crystalline GaCl<sub>3</sub> was molten and heated to 100 °C in a quartz cell by an electrical heater, resulting in a GaCl<sub>3</sub> vapour pressure of about 20 Torr. The GaCl<sub>3</sub> vapour was transported to the reactor by the nitrogen carrier gas. Nitrogen was also used in order to dilute the ammonia and to increase the total gas flow rate. The GaCl<sub>3</sub> supply was controlled by both the cell temperature and the flow rate of the N<sub>2</sub> carrier gas. The typical N<sub>2</sub> flow rate was 100 sccm. The GaCl<sub>3</sub> vapour supply was 3 sccm at atmospheric reactor pressure. During the process 1000–2000 sccm of NH<sub>3</sub> and 1000–2000 sccm N<sub>2</sub> were introduced into the

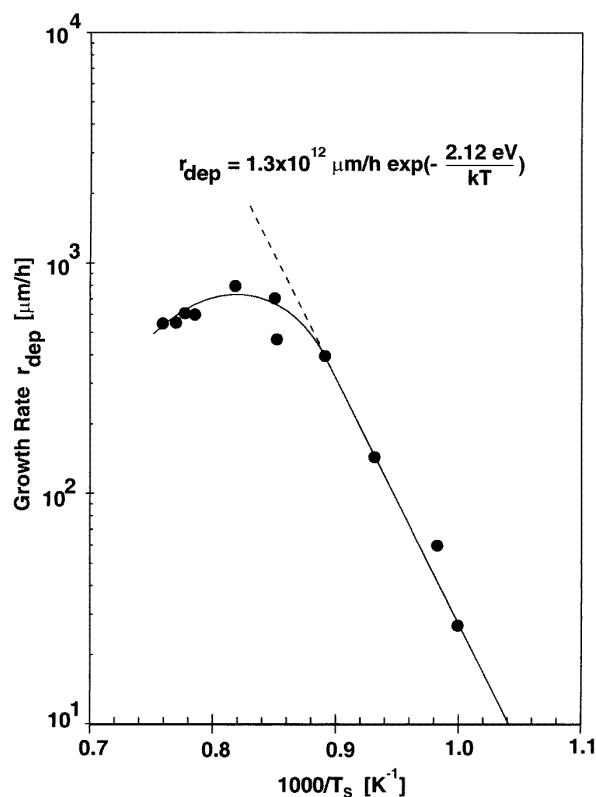


**Figure 14.** Variation of GaN deposition (growth) rate  $r_{\text{dep}}$  as a function of reciprocal substrate temperature. The growth direction of the VPE grown GaN was (1120).

reactor, resulting in a V/III ratio of 500 to 700 (figure 16). GaN grown on  $c\text{-Al}_2\text{O}_3$  at temperatures of 930–1050 °C showed a photoluminescence spectrum dominated by an emission near 3.47 eV. The band edge emission peak had a relatively high FWHM of 60 meV at room temperature and the donor-bound exciton emission had a FWHM of 25 meV at 77 K. According to Hall measurements, the GaN films had high concentrations of free electrons ( $n_e = 10^{19} \text{ cm}^{-3}$ ) and electron mobilities at room temperature between 3 and 50  $\text{cm}^2 \text{ V}^{-1} \text{ s}^{-1}$ , indicating insufficient quality for device applications.

Ilegems [97] succeeded in depositing thick GaN films by VPE with strongly reduced concentrations of free carriers. The vapour deposition apparatus consisted of a 75 cm long, horizontal, single-zone furnace, containing  $\text{SiO}_2$  reaction and insertion tubes. HCl gas, diluted in a He carrier, was passed over an  $\text{Al}_2\text{O}_3$  boat containing liquid Ga, and provided the transport of Ga as GaCl. A second gas stream consisted of  $\text{NH}_3$  diluted in a He carrier, which bypassed the Ga source and discharged directly near the centre of the reaction apparatus. The formation of GaN occurred immediately upon mixing of the (GaCl+He) and ( $\text{NH}_3$ +He) flows; the actual deposition zone was approximately 5 cm long and the temperature over this zone was constant. The growth parameters empirically adapted were: a reaction zone temperature of 1040–1060 °C; a Ga source temperature of 900 °C; and flow rates of 1.6–1.8 sccm for HCl, 360–400 sccm for  $\text{NH}_3$ , 1000 sccm for the HCl carrier and 400 sccm He as the

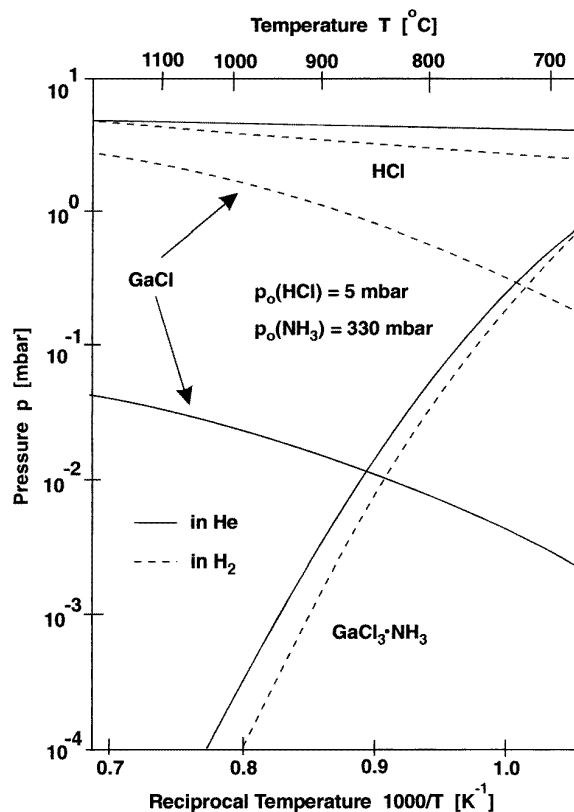


**Figure 15.** Calculated equilibrium partial pressures for input pressures of 5 and 330 mbar for HCl and  $\text{NH}_3$ . The calculation was done for a hydrogen system ( $p(\text{He}) = 0 \text{ mbar}$ ) and a helium system ( $p(\text{H}_2) = 0 \text{ mbar}$ ). For thermodynamic equilibrium, calculated partial pressures including the species HCl, GaCl,  $\text{NH}_3$ ,  $\text{GaCl}_3 \cdot \text{NH}_3$ ,  $\text{H}_2$  and He show that in the high-temperature region GaCl is the important Ga precursor, whereas with decreasing temperature  $\text{GaCl}_3 \cdot \text{NH}_3$  can act as a source for GaN [92].

$\text{NH}_3$  carrier. At atmospheric pressure, deposition rates of 33 to 66  $\mu\text{m h}^{-1}$  were measured on  $c\text{-Al}_2\text{O}_3$  substrates. GaN films up to 250  $\mu\text{m}$  thick were obtained. All undoped films were n-type with carrier concentrations as low as  $n_e = 2 \times 10^{17} \text{ cm}^{-3}$  and mobilities of  $\mu_e = 380 \text{ cm}^2 \text{ V}^{-1} \text{ s}^{-1}$ .

Molnar *et al* [98,99] were able to demonstrate that HVPE is capable of growing thick GaN films on sapphire substrates with greatly improved structural and electronic properties, as compared to heteroepitaxial GaN films grown by MOCVD or MBE. To achieve such properties, the sapphire substrates were prepared with GaCl or ZnO pretreatments [100]. GaN films up to 74  $\mu\text{m}$  thick were deposited at 1050 °C with growth rates of 15  $\mu\text{m h}^{-1}$ . The relatively low dislocation density of  $10^8 \text{ cm}^{-2}$  observed close to the surface of the thick films yielded electron mobilities and concentrations of 845  $\text{cm}^2 \text{ V}^{-1} \text{ s}^{-1}$  and  $7 \times 10^{16} \text{ cm}^{-3}$  at room temperature, comparable to very good thin GaN films grown by MOCVD or MBE (see table 11 later).

Growth by a modified VPE process called the sublimation sandwich method (SSM) was reported by Wetzel and co-workers [101,102] (figure 17). The GaN films were grown from metallic Ga and activated ammonia

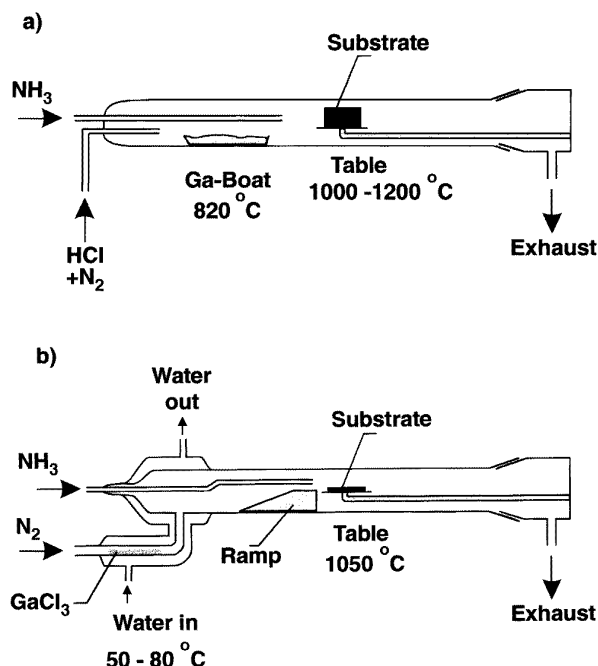


**Figure 16.** Schematic diagram of two VPE systems used to produce epitaxial GaN films from (a) Ga/HCl/NH<sub>3</sub> and (b) GaCl<sub>3</sub>/NH<sub>3</sub> mixtures [94].

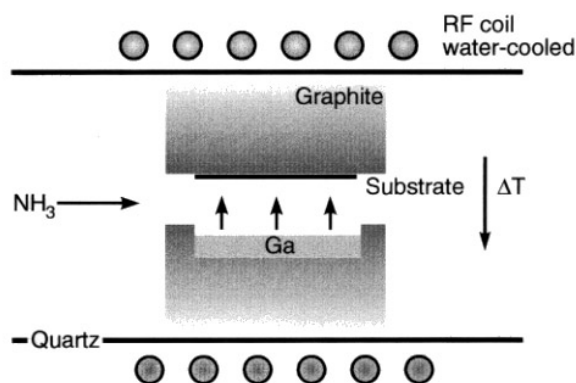


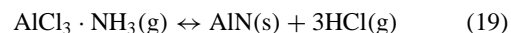
**Figure 17.** Schematic diagram of the high-temperature VPE reactor (sublimation sandwich method). The graphite crucible containing the metallic Ga and the substrate is heated inductively via a water-cooled coil. Ga vapour is transported over a short gap of a few millimetres, passing through the ammonia flow which is parallel to the substrate surface [102].

on (0001) 6H-SiC, using a modification of the sandwich method originally described in [103]. The quartz reactor contains several deposition cells in a row, which share the same ammonia gas stream. Each cell consists of a Ga source and substrate, separated by a gap of only 5 mm. The ammonia flow rate through the gap is 25 000 to 50 000 sccm at atmospheric pressure. Under these conditions, there is an effective mass transport of Ga vapour and activated nitrogen towards the substrates. At growth temperatures between 1170 and 1270 °C, single crystal layers of GaN were obtained at growth rates up to 300 μm h<sup>-1</sup>. GaN epitaxial layers of thickness 60 μm

showed XRD patterns with a GaN (0002) reflection half-width of 360 arcsec and a rocking curve half-width of 450 arcsec. These GaN films also showed n-type conduction with carrier concentrations of  $2 \times 10^{17} \text{ cm}^{-3}$  and electron mobilities in the range from 30 to 80 cm<sup>2</sup> V<sup>-1</sup> s<sup>-1</sup>. Vodakov *et al* [104] succeeded in growing GaN on 6H-SiC substrates by using the SSM technique with deposition rates up to 200–1100 μm h<sup>-1</sup> (table 11). GaN films with thicknesses between 70 and 100 μm showed near-bandgap photoluminescence at 3.48 eV with a FWHM of 8 meV. The FWHM of the (0002)  $\omega$ -scan was measured to be in the range of 270–300 arcsec, indicating good structural quality for films grown at very high rates.

Although the concentrations of free carriers were remarkably low, preliminary efforts by Ilegems, Fischer, Vodakov and co-workers to obtain type conversion in GaN by doping with Mg, Zn or Cd were not successful, which limits the usefulness of GaN grown by VPE and especially by SSM to the preparation of n-type structures and substrates for the homoepitaxy of GaN devices by MOCVD and MBE.

**4.2.2. Vapour phase epitaxy of AlGaIn.** One important advantage of Group III-nitrides in comparison to other wide-bandgap materials is the possibility of bandgap engineering between 1.9 and 6.2 eV by the deposition of InGaIn and AlGaIn alloys. A growth method suitable for the fabrication of transistors or LEDs must allow the preparation of alloys. Using VPE, it has been demonstrated that aluminium nitride films can be grown on fused quartz, silicon (111), and spinel substrates (MgO<sub>1.4</sub>Al<sub>2</sub>O<sub>3</sub> (100)) by the reaction of AlCl<sub>3</sub> with NH<sub>3</sub> or ammonolysis of AlCl<sub>3</sub>·NH<sub>3</sub> [105]. In this pyrolytic process, the reactants are supplied to the reaction zone either separately or in the form of the nearly stoichiometric complex compound AlCl<sub>3</sub>·NH<sub>3</sub>. The decrease in the standard free enthalpy  $\Delta G$  for equilibria,



with increasing temperature (for reaction (18):  $\Delta G(500 \text{ K}) = 16 \text{ kJ mol}^{-1}$ ,  $\Delta G(1500 \text{ K}) = -80 \text{ kJ mol}^{-1}$ ; for reaction (19):  $\Delta G(500 \text{ K}) = 135 \text{ kJ mol}^{-1}$ ,  $\Delta G(1500 \text{ K}) = -40 \text{ kJ mol}^{-1}$ ) demonstrates the shift of equilibrium in favour of AlN formation. In experiments for pyrolytic preparation of AlN films, vertical reactors and substrate temperatures of 700 to 1300 °C have been used. Convenient evaporation temperatures for AlCl<sub>3</sub> and AlCl<sub>3</sub>·NH<sub>3</sub> (vapour pressure: 0.1 to 40 Torr) are 80 to 140 °C and 180 to 400 °C respectively. The vapour was transported into the reaction zone with argon used as carrier gas. Molar ratios of  $n(\text{AlCl}_3)$  to  $n(\text{NH}_3)$  between 0.001 and 1 were then realized by adjusting the NH<sub>3</sub> flow rates. The observed deposition rates of AlN ( $r_{\text{dep}} = 0.6\text{--}6 \text{ μm h}^{-1}$ ) were directly proportional to the partial pressure of the aluminium component, and depended on the substrate temperature and the total flow rate over one order of magnitude.

Fibre-textured (0001) AlN could be produced on Si and quartz; epitaxial (0001) oriented films could be deposited on spinel substrates at 1050 to 1250 °C. The electrical properties of the AlN films were determined by analysing the current–voltage and the rf capacitance–voltage characteristics of the metal–insulator–semiconductor (MIS) structure Al–AlN–Si. The effective carrier density and conductivity were determined to be  $n = 2 \times 10^{12}$ – $8 \times 10^{12} \text{ cm}^{-2}$  and  $\sigma = 2 \times 10^{-16}$ – $1.2 \times 10^{-13} (\Omega \text{ cm})^{-1}$  respectively. The direct bandgap of a 0.5  $\mu\text{m}$  thick AlN film was found to be 5.93 eV at room temperature and the surface roughness to be 30 nm, from reflectance and transmittance studies in the energy range 3.5 to 7.0 eV.

After the successful deposition of GaN and AlN films,  $\text{Al}_x\text{Ga}_{1-x}\text{N}$  ( $x = 0.45$ ) layers were grown via VPE on sapphire substrates at 1050 °C by Baranov and co-workers [106]. A mixture of GaCl, AlCl and ammonia was introduced into the reaction zone. The films were started with GaN. Then AlGaIn with increasing Al content was grown by increasing the temperature of the Al source from 600 to 750 °C. All undoped AlGaIn samples showed n-type conductivity with temperature-independent electron concentrations and mobilities between 77 and 300 K. With increasing Al content up to values of  $x = 0.4$ , the electron concentration decreased from  $5 \times 10^{19} \text{ cm}^{-3}$  to  $10^{19} \text{ cm}^{-3}$  and the mobility from 100 to  $10 \text{ cm}^2 \text{ V}^{-1} \text{ s}^{-1}$ . The reason for the unexpectedly high concentration of carriers was determined by dispersive x-ray microanalysis (EDAX). All samples contained more than 1 at.% silicon atoms, which act as donors (section 5). Therefore the carrier concentration could not be sufficiently reduced by increasing the Al content, and p-doping of the layers was impossible.

To date it has been demonstrated that VPE is a highly suitable growth technique for very thick GaN films because of the high growth rate and the fact that bandgap engineering in the near-UV spectral range is possible by fabrication of AlGaIn/GaN heterostructures. However, the very high growth temperature of VPE processes, between 1000 and 1200 °C, in combination with hydrides used as precursors causes two major problems. Intentionally undoped GaN and AlGaIn films show electron concentrations above  $10^{17} \text{ cm}^{-3}$ , mostly due to silicon and oxygen impurities. One source of Si and O impurities is the quartz tubes used in VPE reactors and which can be affected by chlorides (especially  $\text{AlCl}_3$ ) at high temperatures. It is also difficult to avoid impurities from the substrate holder which is also heated to above 1000 °C in an aggressive environment. As stated above, besides the problem of the high concentration of free carriers which hinders the growth of p-type material, the high growth temperature in VPE makes it very difficult to grow InGaIn alloys. The growth temperature is far above the decomposition temperature of InN, and large overpressures of  $\text{NH}_3$  have to be realized to prevent InGaIn films from decomposing. The lack of p-type GaN and no demonstrated growth of InGaIn layers by VPE has so far kept the technique from the fabrication of LEDs.

### 4.3. Reactive sputtering

Plasma-assisted reactive deposition is often a suitable method for growing materials with high melting points, such as Group III-nitrides, at low substrate temperatures. In most cases, low-temperature processes are more attractive, particularly for use in semiconductor device fabrication. The first reported plasma-assisted deposition of Group III-nitrides was by Fischer and Schröter in 1910. They reacted indium metal with nitrogen in a cathodic discharge to produce InN powder [107]. Kirstenmacher and co-workers used the advantage of low substrate temperatures during reactive sputtering processes for the growth of InN films on AlN buffered (0001) sapphire substrates [108]. The sputtering system employed a pair of 2" diameter planar magnetron sputtering sources. The substrate assembly was rotatable and could place the substrate above either sputtering source to allow for the sequential deposition required for bilayer and multilayer films [109]. The targets were water-cooled Al or In discs of 99.999% purity. Reactive growth was carried out in 99.999% pure  $\text{N}_2$  gas at a pressure of 5 mTorr. To reduce oxygen contamination in the films, the active sputtering area was surrounded by an internal liquid-nitrogen-cooled Meisner trap. For the growth of optimized InN layers, a 40 nm thick AlN nucleation layer was grown at 600 °C by DC sputtering ( $I = 500 \text{ mA}$ ,  $U = 325 \text{ V}$ ,  $t = 15 \text{ min}$ ). Afterwards the temperature of the buffered substrate was set to the InN film growth temperature of 400 °C. The InN overlayer was grown, with a deposition rate of  $0.75 \mu\text{m h}^{-1}$ , by applying rf power of 50 W. The electrical properties were determined by Hall measurements. The concentrations of free electrons in 0.5  $\mu\text{m}$  thick optimized layers were  $2 \times 10^{20} \text{ cm}^{-3}$  with up to  $60 \text{ cm}^2 \text{ V}^{-1} \text{ s}^{-1}$  mobility.

InN with improved electrical properties was grown on  $c\text{-Al}_2\text{O}_3$  using rf sputtering of 99.999% pure In at a nitrogen sputter gas pressure of  $2 \times 10^{-2} \text{ Torr}$  by Hovel and Cuomo [110,111]. Polycrystalline InN layers of thickness up to 5  $\mu\text{m}$  were grown at substrate temperatures at or below 400 °C. The InN films were dark red, with a resistivity in the range of  $5 \times 10^{-3} \Omega \text{ cm}$ . The films were n-type with a Hall mobility of  $250 \pm 50 \text{ cm}^2 \text{ V}^{-1} \text{ s}^{-1}$  and a carrier concentration of  $(5\text{--}8) \times 10^{18} \text{ cm}^{-3}$ . The improved but still high carrier concentration was attributed to a high density of native defects.

Foley and Tansley reported on InN grown by rf sputtering, where progressive nitridization of the In target was observed to control the morphology and structure of the films produced [112]. Films were sputtered from a nominal 99.999% In target which was nitridated for more than 150 h under process conditions in a high-purity nitrogen ambient at  $10^{-2} \text{ Torr}$ . Small growth rates between 0.025 and  $0.09 \mu\text{m h}^{-1}$  on glow-cleaned glass substrates were achieved at substrate temperatures of 80 °C. Polycrystalline InN films with predominantly  $c$ -axis orientation and thicknesses from 0.01 to 2  $\mu\text{m}$  were produced. These films had carrier concentrations between  $3 \times 10^{16}$  and  $3 \times 10^{17} \text{ cm}^{-3}$  and surprisingly high Hall mobilities of up to  $3000 \text{ cm}^2 \text{ V}^{-1} \text{ s}^{-1}$  at room temperature. This is the highest mobility ever reported for



**Table 7.** Typical reactive rf sputtering conditions for GaN film growth.

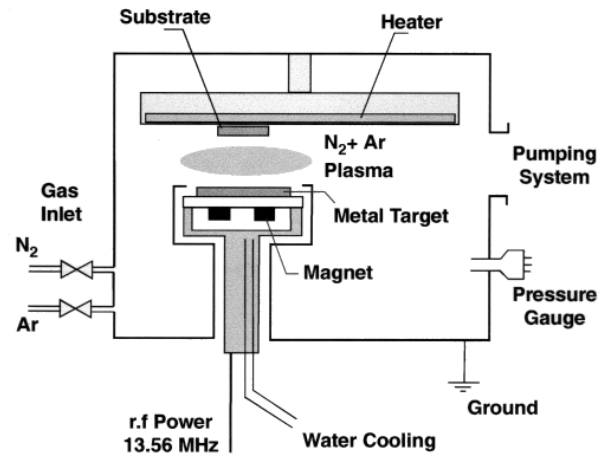
Target	Ga (purity, 99.9999%)
Substrate	Al <sub>2</sub> O <sub>3</sub> , Corning glass
Sputter pressure	$(3-5) \times 10^{-2}$ Torr
Ar/N <sub>2</sub>	0.42
rf power	40 W (13.56 MHz)
Anode voltage	0.7–0.9 kV
Substrate temperature	50–400 °C
Distance anode–cathode	40 mm
Background pressure	$5 \times 10^{-8}$ Torr
DC bias	–150 to +150 V
Deposition rate	$0.35 \mu\text{m h}^{-1}$

nitride semiconductors and has not since been reproduced by any other group.

The reactive sputtering technique has also been employed as a plasma-assisted method for the growth of GaN films at low substrate temperatures by other groups [113, 114]. The resistivity of GaN films prepared this way is high ( $10^8$ – $10^{13} \Omega \text{ cm}$ ), probably because they are strongly compensated by acceptor-like defects. Zembutsu and Kobayashi deposited GaN on aluminium-coated Corning 7059 glass, as well as on *c*-Al<sub>2</sub>O<sub>3</sub> substrates, by reactive sputtering (figure 18) [115]. A mixture of molecular nitrogen and argon was used as nitrogen source and sputtering gas. Argon was introduced in order to increase the sputtering rate of gallium. The sputtering gas pressure was in the range of  $4 \times 10^{-2}$  Torr. Presputtering was carried out for about 4 h in each process in order to clean and stabilize the surface of the gallium target. The reactive sputtering conditions for GaN growth are summarized in table 7. RHEED observations and the XRD pattern of films deposited at 350 °C, with a sputtering voltage of 0.85 kV and a DC bias of –100 V, indicated that *c*-axis oriented polycrystalline material was grown, with grain sizes of 3  $\mu\text{m}$ . The FWHM of the (0002) rocking curve peak was 8.8° (528 min). The resistivity of the GaN film on the aluminium-coated glass substrate was measured in the growth direction by depositing indium onto the surface of the film as an upper electrode. The resistivity was estimated to be greater than  $10^9 \Omega \text{ cm}$ .

Stimulated by the high resistivities of sputtered GaN films, Matsushita and co-workers deposited amorphous gallium nitride films on GaAs MIS structures [116]. The amorphous GaN was used as an insulating layer, to passivate the GaAs surface and reduce the density of surface states. The surface state density on a GaAs MIS structure was determined to be  $7.6 \times 10^{11} \text{ cm}^{-2} \text{ eV}^{-1}$ , much lower than the surface state density with the native oxide. With that experiment the potential of sputtered Group III-nitrides as passivation or protective layers for glass surfaces or electrical devices was demonstrated. Furthermore the advantage of low-temperature plasma induced growth techniques to deposit amorphous Group III-nitrides was realized.

AlN is of special interest for use as a thin film piezoelectric material in microwave acoustic resonator surface acoustic wave devices, as discussed in more

**Figure 18.** Schematic diagram of a planar diode rf reactive sputtering system for the deposition of GaN. The gallium source is a target consisting of a stainless steel cup filled with gallium. A mixture of molecular nitrogen and argon is used as nitrogen source and sputtering gas (rf plasma, 13.56 MHz).

detail in section 9.1. Aita reported the growth of basal-oriented AlN on Si(111) substrates by reactive rf diode sputter deposition at substrate temperatures of 100 °C [117]. Optimized AlN films were prepared from a 99.9995% Al target, using Ar/N<sub>2</sub> mixtures (purity, 99.999%) as sputter gases at a working pressure of  $10^{-2}$  Torr. Optimized films were grown with a deposition rate of  $0.13 \mu\text{m h}^{-1}$  at a power density of  $0.8 \text{ W cm}^{-2}$ . XRD results showed that the crystal structure of the films evolved from multi-oriented Al, to an amorphous structure, to oriented AlN, as the N<sub>2</sub> content of the sputtering gas was increased from 0 to 100%. The smallest value, from an XRD  $\theta/2\theta$  scan of the (0002) AlN diffraction peak half-width, 300 arcsec, was obtained on a 0.4  $\mu\text{m}$  thick film sputtered with 100% nitrogen gas. Liaw and Cronin also deposited AlN films on silicon wafers by the sputtering technique [118]. A 200 nm thick layer of Si<sub>3</sub>N<sub>4</sub> was used between the AlN and the Si(100) substrate as an electrical insulator. The sputtered AlN films exhibit columnar growth in a (0001) direction. For optimized AlN films, the column diameter was 32 nm and the surface roughness (rms) between 3 and 9 nm.

Films of AlN, GaN, InN and AlInN were grown on *c*-plane sapphire by Kubota *et al* using rf sputtering at 13.56 MHz of metallic targets in a reactive nitrogen plasma. The specialty of the sputtering system was that the vacuum chamber had three sputtering guns and a rotatable substrate holder above them [119]. Film thicknesses of the order of 1  $\mu\text{m}$  were obtained with deposition rates between 0.18 and  $0.54 \mu\text{m h}^{-1}$ . The best sputtering conditions and some structural and electrical properties are listed in table 8. Alloy films of Al<sub>x</sub>In<sub>1-x</sub>N were prepared by using a composite target composed of a slotted Al sheet over an In plate. Al<sub>x</sub>In<sub>1-x</sub>N with Al contents between 58 and 100% and bandgaps between 2.6 and 5.9 eV were grown at temperatures of 500 °C. Al<sub>x</sub>In<sub>1-x</sub>N layers are interesting because they offer the possibility of lattice-matched Al<sub>x</sub>In<sub>1-x</sub>N/GaN heterostructures for Al contents

**Table 8.** Optimized sputtering conditions for different Group III-nitrides and some structural and electrical properties of the sputtered films produced [119].

Material	Pressure (mTorr)	Sputter gas N <sub>2</sub> /Ar ratio	rf power (W)	Temperature (°C)	XRD: 2 $\Theta$ / $\omega$ scan (min)	$\omega$ scan (min)	$n_e$ (cm <sup>-3</sup> )	$\mu_e$ (cm <sup>2</sup> V <sup>-1</sup> s <sup>-1</sup> )
AlN	15	9.0	100	500	—	—	—	—
GaN	20	1.5	50	500	14.7	60	$1.2 \times 10^{19}$	8.9
InN	20	1.0	30	400	13.5	180	$4.8 \times 10^{20}$	38
Al <sub>x</sub> In <sub>1-x</sub> N	15	1.0	100	500	—	—	—	—

of  $x \approx 0.8$ , where the layers have different bandgaps and refractive indices. If the Al<sub>0.8</sub>In<sub>0.2</sub>N films are highly resistive, Al<sub>x</sub>In<sub>1-x</sub>N/GaN heterostructures can be used to create two-dimensional electron gases in GaN, like with Al<sub>x</sub>Ga<sub>1-x</sub>N/GaN but with the advantage of good lattice matching.

The advantage of plasma-assisted sputtering methods is the low substrate temperature, which enables the deposition of In-containing alloys, the use of substrate materials such as Si or GaAs, and the reduction of thermally activated diffusion of dopants and interdiffusion at interfaces of multilayer structures. The disadvantage of sputter processes is that the Ga, In and Al targets are usually easily oxidized. The melting point of metallic Ga is very low (29.8 °C); it is necessary to melt the Ga target by presputtering before deposition in order to remove gallium oxide from the target surface. Aluminium oxide causes a very low sputtering yield; the oxide layer surface prevents sputtering of metallic Al. Therefore, these surface oxide layers should be removed by long (several hours) presputtering. Alloys like AlInN are difficult to grow over the whole composition range, because the sputter yields for In and Al are very different. The structural properties of Group III-nitrides grown by sputtering processes at low temperatures are polycrystalline or columnar, which limits the applications, especially for electronic devices.

#### 4.4. High-pressure high-temperature growth of Group III-nitride crystals

The use of Group III-nitride single crystals as substrates for the homoepitaxial growth of thin AlN, GaN or InN films represents the most natural way to overcome difficulties caused by a large lattice mismatch and differences in thermal expansion between the substrate and an epitaxial film. The other attraction of bulk single crystals lies in the opportunity to use them as a standard and reference material. Due to the very high melting temperature of GaN (2791 K) at a correspondingly high equilibrium pressure of nitrogen ( $\approx 4$  GPa), bulk crystals of GaN cannot be obtained by typical equilibrium methods, e.g. Czochralski or Bridgman methods in which stoichiometric melts are used. Therefore, the lower temperature method of growth from a solution has to be applied.

Madar *et al* [57] succeeded in preparing crystals with dimensions below 1 mm and epitaxial films of GaN from solution in Ga. They estimated the solubility of GaN in liquid Ga at 1200 °C and a nitrogen pressure of 8 kbar to be  $10^{-3}$  mol fraction. The low solubility caused the

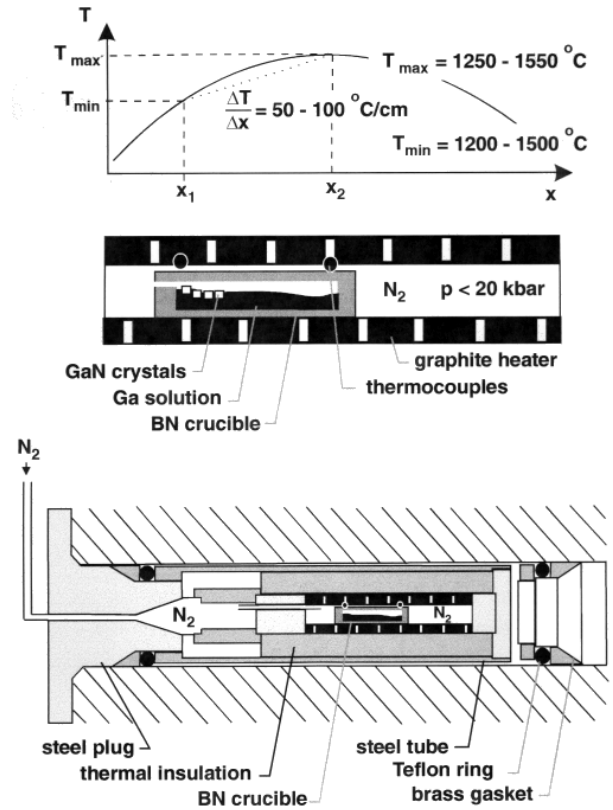


**Figure 19.** Nitrogen gas pressure apparatus for the high-pressure vapour growth (synthesis solid diffusion, SSD) of GaN. The gas pressure cell, the crucible and the temperature profile along the crucible are shown [120–123].

growth rate to be only about  $0.04 \mu\text{m h}^{-1}$ . Grzegory and co-workers determined the atomic fraction of nitrogen at a nitrogen pressure of 20 kbar in liquid Ga and Al at 1800 °C to be 0.01 at.% and 0.05 at.% respectively. At 940 °C and the same nitrogen pressure, a nitrogen fraction of  $5.6 \times 10^{-5}$  at.% in liquid In was determined. Since the solubility of nitrogen in the metal melts was relatively low, the ‘synthesis solid diffusion’ method (SSD) was chosen for crystal growth [120–122]. Crystal growth experiments were carried out in a gas pressure chamber of 30 mm internal diameter [123]. Furnaces with diameters between 10 and 14 mm were equipped with a BN crucible containing Al, Ga or In and fixed in the gas pressure chamber (figure 19). After annealing in vacuum, the system was filled with pure N<sub>2</sub>, compressed and heated. The temperature profile inside the furnace was monitored by a set of thermocouples arranged along the crucible.

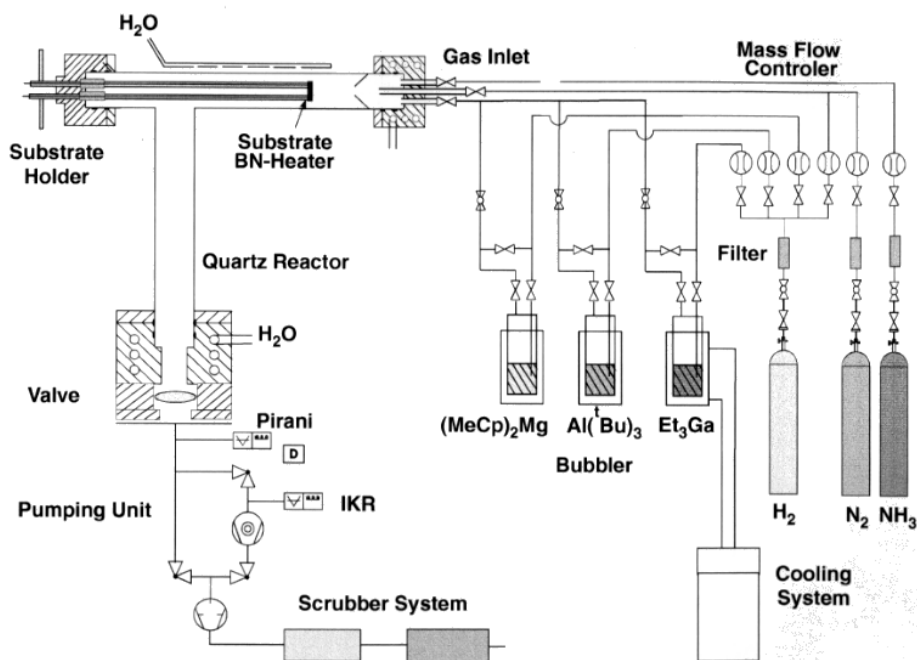


**Figure 20.** Schematic diagram of a low-pressure MOCVD apparatus for the deposition of epitaxial GaN and AlN films. The precursor for the growth of GaN and AlN is  $\text{Et}_3\text{Ga}$  and  $\text{Al}(\text{iBu})_3$  respectively, transported with hydrogen used as carrier gas. Ammonia diluted with nitrogen is used as the nitrogen source.  $(\text{MeCp})_2\text{Mg}$  is the Mg source for producing p-type material. The organometallic precursors and ammonia are pyrolysed at temperatures of  $1000^\circ\text{C}$  at the substrate surface.

Growth should be carried out under conditions where GaN is stable. Use of a high temperature, which requires applying high nitrogen pressure, ensures maximum solubility of nitrogen in the liquid gallium. Therefore the nitrogen pressure was raised to values between 9 and 17 kbar. The temperature of the crucible was increased up to  $1250\text{--}1550^\circ\text{C}$  in the hottest part, with the temperature of the cooler end about  $50^\circ\text{C}$  lower. The formation of a thin polycrystalline GaN film on the Ga surface, and its dissolution and transport into the cooler part of the solution lead to the nucleation and growth of GaN single crystals. The crystals, which grow with a rate under  $100\ \mu\text{m h}^{-1}$ , are of hexagonal structure and high crystalline quality. GaN platelets up to  $1\text{--}10\ \text{mm}$  in size and shaped like elongated hexagons were grown at a nitrogen pressure of 10 kbar and a maximum temperature of  $1400^\circ\text{C}$ . The longest axis was along  $[11\bar{2}0]$ . In all cases, the smallest dimension was in the  $c$ -axis direction. The ratio of length to thickness along the  $c$ -axis could be as large as 100. TEM studies showed that one side of the plate perpendicular to the  $c$ -axis was almost atomically flat (with fluctuations corresponding to bilayer steps of  $10\text{--}15\ \text{\AA}$ ), while the opposite side was rough. It was shown that the smooth facets in single crystals correspond to the  $(0001)$  Ga face, whereas the rough facets correspond to the  $(000\bar{1})$  N face [124]. Planar defects in the form of stacking faults were observed close to the rough surface. The material near the opposite side of the platelets had a very low dislocation density of below  $10^6\ \text{cm}^{-2}$  [125]. X-ray studies using  $(0004)\ \text{CuK}_\alpha$  reflection showed that the quality was related to crystal size. The x-ray rocking curve FWHM was about  $20\text{--}30\ \text{arcsec}$  for crystals not larger than  $1\ \text{mm}$ . For larger crystals ( $1\text{--}3\ \text{mm}$ ), the

rocking curve FWHM was broader, and for crystals of  $3$  to  $10\ \text{mm}$  size, the rocking curve split [126]. The bulk GaN crystals had high concentrations of free electrons ( $n_e = 10^{19}\text{--}10^{20}\ \text{cm}^{-3}$ ), mainly caused by oxygen impurities, and mobilities ranging from  $30$  to  $90\ \text{cm}^2\ \text{V}^{-1}\ \text{s}^{-1}$ . By adding  $0.5\text{--}1\ \text{at.}\%$  of Mg to the Ga melt, it was possible to grow insulating crystals without significant structural degradation, but p-type GaN could not yet be realized.

Even though the melting point of AlN is higher than that of GaN, it is also possible to grow small AlN crystals by the SSD method [126]. The mechanism for the synthesis of AlN crystals from its constituents strongly depends on the nitrogen pressure. When a bulk Al sample is heated at a  $\text{N}_2$  pressure of  $0.1\text{--}6.5\ \text{kbar}$ , a very strong exothermic reaction occurs at temperatures between  $970$  and  $1230^\circ\text{C}$ . This reaction is AlN synthesis, leading to a high degree of conversion of liquid Al into nitride. The product is AlN powder or partially sintered ceramics. For pressures of  $8\ \text{kbar}$  and temperatures between  $1400$  and  $1600^\circ\text{C}$  over a duration of  $9\ \text{h}$ , AlN crystals with grain sizes of  $100\ \mu\text{m}$  were obtained. To grow crystals and platelets with larger sizes, higher growth temperatures will have to be realized.

Experiments for InN growth were carried out at a nitrogen pressure of  $18\text{--}20\ \text{kbar}$  with a maximum temperature of  $950^\circ\text{C}$ , and for a typical duration of  $10\ \text{h}$ . After the process, and careful etching with HCl to remove the residual In, small InN crystallites (grain sizes  $\approx 50\ \mu\text{m}$ ) were observed. The small growth rates suggest that the crystallization of InN by this method is not effective due to the extremely low solubility of nitrogen in liquid indium.

The growth of small single crystals by SSD offers the possibility of homoepitaxial growth of thin epitaxial films

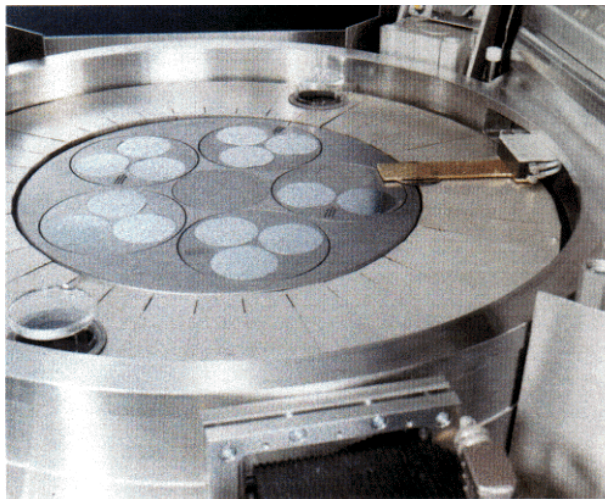


**Figure 21.** Commercial MOCVD planetary reactor (AIXTRON) for 15'' × 2'' substrates, which is in use for the growth of epitaxial Group III-nitride films.

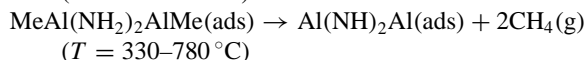
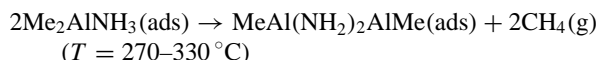
by MBE or MOCVD, which would be very helpful for basic research of the physical and chemical properties of the nitrides. However, to establish the SSD technique for commercial production of Group III-nitride substrates and devices, the crystal sizes must be increased to a minimum of 1'' or 2'' wafers and the concentration of impurities must be reduced to control the electrical conductivity of the samples.

#### 4.5. Metalorganic chemical vapour deposition (MOCVD)

**4.5.1. Precursors and transport gases** The growth of Group III-nitrides by MOCVD entails the transport of gas phase organometallic precursors, hydrides like  $N_xH_y$  for the nitrogen source, and transport gases to a heated substrate on which the precursors are pyrolysed and the nitride film is deposited. The underlying chemical mechanism is complex, involving a combination of gas phase and surface reactions. Although the growth of III–V compound semiconductors by MOCVD has been investigated for two decades, the fundamental reaction mechanism and the related kinetic rate parameters remain poorly characterized, even for the well studied deposition of GaAs. Nevertheless, there has been a concerted effort to develop MOCVD techniques, which have the advantages of large-area growth capability, good conformal step coverage and the precise control of epitaxial deposition (figures 20 and 21).

The deposition of epitaxial MN layers ( $M = \text{In, Ga or Al}$ ) by MOCVD has traditionally been carried out using mixtures of trimethylindium, -gallium, or -aluminium ( $\text{Me}_3\text{M}$ ), and ammonia ( $\text{NH}_3$ ) [127,128]. It is well established [129] that for various radicals,  $R$ ,  $R_3\text{M}$  components react in the gas phase with donors containing acidic hydrogen, such as  $\text{NH}_3$  and  $R'\text{NH}_2$ , to form the adducts  $[\text{R}_3\text{MNH}_3]$  and  $[\text{R}_3\text{MNH}_2\text{R}']$ . These readily eliminate alkane radicals on heating, to form elimination products of the form  $[\text{R}_2\text{MNH}_2]_n$  and  $[\text{R}_2\text{MNH}_2\text{R}']_n$  (where  $n = 2$  or  $3$ ). Thus for example, the growth of AlN from mixtures of  $\text{Me}_3\text{Al}$  and  $\text{NH}_3$  may proceed by the

initial formation of an intermediate gas phase adduct  $[\text{MeAlNH}_3]$ , followed by the elimination of  $\text{CH}_4$  near the hot substrate. Information concerning the surface chemistry occurring during the MOCVD of AlN has been provided by Fourier transform infrared (FTIR) and x-ray photoelectron spectroscopy (XPS) on mixtures of  $\text{Me}_3\text{Al}$  and  $\text{NH}_3$  adsorbed on  $\text{Al}_2\text{O}_3$  [130]. It was concluded that co-adsorption of  $\text{Me}_3\text{Al}$  and  $\text{NH}_3$  at room temperature generates a surface adduct species, proposed to be  $[\text{Me}_2\text{AlNH}_3]$ , together with adsorbed  $\text{NH}_3$ . As the substrate temperature was raised above  $320^\circ\text{C}$ , the appearance of vibrational bands corresponding to AlN indicated the emergence of extended (Al–N) networks on the surface. These  $\text{Al}(\text{NH}_2)_2\text{Al}$  species finally eliminate  $\text{H}_2$  at the surface to form AlN [131], thus:



and



Very few studies into the mechanism of GaN growth from  $\text{Me}_3\text{Ga}$  and  $\text{NH}_3$  mixtures have been carried out. A room-temperature predeposition reaction has been observed [132] during GaN CVD from  $\text{R}_3\text{Ga}$  and  $\text{NH}_3$  ( $R = \text{Me, Et}$ ), and the presence of gas phase adducts  $[\text{R}_3\text{GaNH}_3]$  has been confirmed by infrared spectroscopy [133].  $\text{R}_3\text{Ga}$  compounds are weaker electron acceptors than the corresponding  $\text{R}_3\text{Al}$  compounds, and thus the scarcity of any such adducts with  $\text{NH}_3$ , could be expected due to re-dissociation in the hot zone of the reactor. GaN MOCVD is generally carried out at very high V/III ratios which favour adduct formation, suggesting that amides of the type  $(\text{R}_2\text{GaNH}_2)_n$  may also play a significant role in GaN deposition. The high thermal stability of  $\text{NH}_3$ , although still low compared to  $\text{N}_2$ , is one reason for the use of high substrate temperatures, typically more than  $550^\circ\text{C}$  for InN and above  $900^\circ\text{C}$  for GaN and AlN [134]. The high growth temperature and thus high nitrogen vapour pressure lead to the problem of nitrogen loss from the MN film and to carbon contamination from the decomposition of the organic radical during metalorganic pyrolysis. The loss of nitrogen can be alleviated by the use of high V/III gas ratios during the deposition (e.g.  $>2000:1$ ).

One approach to lower the substrate temperature required for GaN or AlN deposition, and so to reduce the nitrogen loss, is to use alternative nitrogen precursors which are thermally less stable than  $\text{NH}_3$  [135]. Hydrazine ( $\text{N}_2\text{H}_4$ ) has been used in combination with  $\text{Me}_3\text{Al}$  to deposit AlN at temperatures as low as  $220^\circ\text{C}$  [136]. However,  $\text{N}_2\text{H}_4$  is extremely toxic and unstable, which is likely to restrict its large-scale application in MOCVD. More recently, other nitrogen sources such as tert-butylamine ( $\text{t-BuNH}_2$ ) [137], isopropylamine ( $\text{i-PrNH}_2$ ) [138] and trimethylsilylazide ( $\text{Me}_3\text{SiN}_3$ ) [139] have been used with  $\text{Me}_3\text{Al}$  or  $\text{t-Bu}_3\text{Al}$  to deposit AlN films at lower substrate temperatures ( $400\text{--}600^\circ\text{C}$ ) and reduced V/III gas ratios ( $5:1\text{--}70:1$ ). However, the deposited films were invariably contaminated with high levels of residual carbon (up to 11 at.%).

An alternative approach to lowering the deposition temperature of AlN is to use single-source precursors which already contain a direct intramolecular (Al–N) bond. These include  $[\text{Al}(\text{NR}_2)_3]_2$ ,  $[\text{HAl}(\text{NR}_2)_2]_2$  ( $\text{R} = \text{Me}, \text{Et}$ ),  $(\text{Me}_2\text{AlNH}_2)_3$ ,  $(\text{Et}_2\text{AlNH}_2)_3$ ,  $(\text{Me}_2\text{AlNPr}^i)_2$ , and  $(\text{Me}_2\text{AlNH}_2)_3$  [140], from which AlN films have been deposited at moderate substrate temperatures (400–900 °C). The so-called azide precursors,  $[\text{R}_2\text{Ga}(\mu^2\text{-N}_3)]_3$  ( $\text{R} = \text{CH}_3, \text{C}_2\text{H}_5$ ) [141, 142] and  $[(\text{R}_2\text{N})_2\text{Ga}(\eta^1\text{-N}_3)]$  [143], have gained a certain amount of attention because they are less toxic and pyrophoric than the classical precursors. These precursors, however, suffer from a dimeric or trimeric molecular structure, which lowers the vapour pressure and thus the achievable growth rate. The low vapour pressures ( $<1$  Torr at 30 °C) also necessitate the heating of source and reactor lines and the use of high-vacuum CVD equipment. Also N–C and N–H bonded precursors may lead to C impurities and a high NH defect density of the films if those N-containing structural parts are the N source. Miehr *et al* have tested a nitrogen-enriched single-source precursor which is monomeric, highly volatile and free of such features [144]. The prototype of this new class of alternative GaN sources is the bis-azide  $(\text{N}_3)_2\text{Ga}[(\text{CH}_2)_3\text{NMe}_2]$ , which is now in use for the deposition of GaN at temperatures of 500 °C and growth rates above  $0.3 \mu\text{m h}^{-1}$ .

MOCVD of InN is a rather challenging problem because the low-lying onset of decomposition (section 3) is close to the minimum temperature for efficient thermal activation of ammonia, about 550 °C (N–H bond strength, 3.9 eV) (figure 22) [145–148]. There are two reports of alternative single-source precursors for InN. The solid state pyrolysis of polymeric  $[\text{In}(\text{NH}_2)_3]_n$  was studied by Purdy [149], and Fischer and co-workers reported on the air-stable, nonpyrophoric, and volatile single-source precursor  $(\text{N}_3)_2\text{Ga}[(\text{CH}_2)_3\text{NMe}_2]_2$  [150]. This precursor was used to produce amorphous and polycrystalline InN films on 50 nm thick AlN buffer layers on sapphire. Growth rates between  $0.3$  and  $5 \mu\text{m h}^{-1}$  were obtained at substrate temperatures of 300 to 450 °C and a reactor pressure of 0.2 mTorr.

Although there are many different ideas for alternative precursors, only conventional precursors such as  $\text{Et}_3\text{M}$  or  $\text{Me}_3\text{M}$  are commercially available in the quantities and purities necessary to produce epitaxial films with good structural properties and sufficiently low concentrations of impurities and intrinsic defects to allow control of conductivity and doping. Therefore we now concentrate further on MOCVD using commercially available precursors.

Hydrogen, besides nitrogen predominantly used as the transport gas, can influence the chemical reaction mechanism of  $\text{Et}_3\text{M}$  or  $\text{Me}_3\text{M}$  in the gas phase by changing the reaction temperature of the metalorganic compounds or the concentration of reaction products. Hydrogen at the surface of the growing film can influence the growth rate and the structural properties [151, 152]. To obtain a basic understanding of the role of hydrogen in GaN growth, the possible sources of hydrogen and the influence of hydrogen on the chemical reaction mechanism in the gas phase and at the surface need to be discussed.

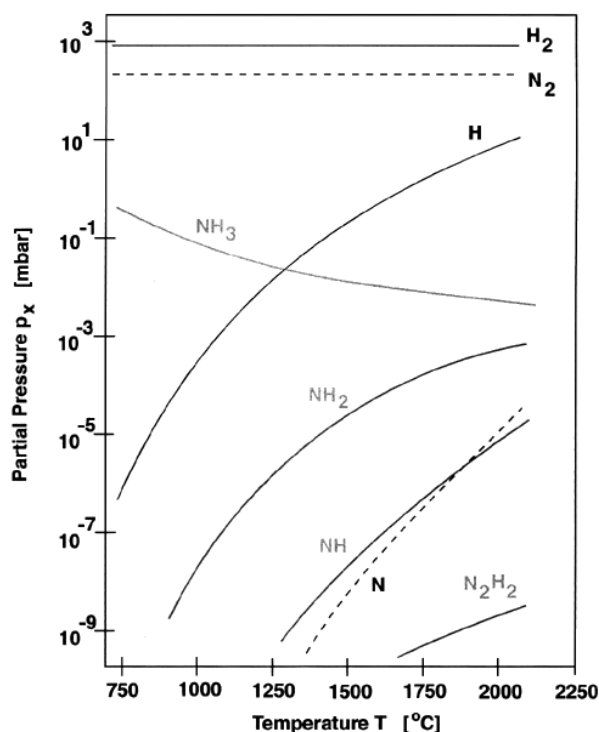


**Figure 22.** Temperature dependence of equilibrium partial pressures of species arising from the decomposition of ammonia (starting condition:  $p(\text{NH}_3) = 10^3$  mbar) [145].

Use of hydrogen as a transport gas and the pyrolysis of highly concentrated  $\text{NH}_3$  result in a high concentration of molecular and atomic hydrogen near the substrate surface. A growth temperature of more than 900 °C is also higher than the decomposition temperature of the metalorganic compounds and their hydrocarbon ligands. This leads to the desired bond breaking between the metal atom and the methyl or ethyl groups of the precursors, but can also cause a pyrolysis of the hydrocarbons with incorporation of hydrogen and carbon into the films. Yoshida *et al* [153] studied the decomposition of  $\text{Me}_3\text{Ga}$  and  $\text{Et}_3\text{Ga}$  in hydrogen and nitrogen atmospheres using a quadrupole mass analyser. The decomposition reaction of the metalorganic precursors is strongly influenced by the presence of molecular hydrogen. The decomposition reactions of  $\text{Me}_3\text{Ga}$  in  $\text{H}_2$  and in  $\text{N}_2$  and of  $\text{Et}_3\text{M}$  in  $\text{H}_2$  and  $\text{N}_2$  take place at temperatures of 400 °C, 500 °C, and 260 °C and 300 °C respectively, showing that molecular hydrogen reduces the reaction temperature (figure 23). The reaction mechanisms are hydrolysis for  $\text{Me}_3\text{Ga}$  in  $\text{H}_2$ , homolytic fission for  $\text{Me}_3\text{Ga}$  in  $\text{N}_2$ , and  $\beta$ -elimination for  $\text{Et}_3\text{M}$  in both  $\text{H}_2$  and  $\text{N}_2$ . By changing the reaction temperature and the reaction mechanism of the metalorganic precursor, the partial pressure of hydrogen influences the deposition rate of GaN and therefore the structural properties of the resulting film, especially at low growth temperatures.

Beaumont *et al* [154] calculated the temperature dependence of equilibrium partial pressures in the gaseous  $\text{Me}_3\text{Ga-NH}_3\text{-H}_2$  system (starting conditions:  $p(\text{Me}_3\text{Ga}) = 0.01$  mbar,  $p(\text{NH}_3) = 40$  mbar,  $p(\text{H}_2) = 1000$  mbar) (figure 24). It appears that  $\text{NH}_3$  is almost completely

**Table 9.** Equilibrium partial pressures of the gaseous  $\text{Me}_3\text{Ga}/\text{NH}_3/\text{H}_2$  system with the following starting conditions:  $p(\text{Me}_3\text{Ga}) = 10^{-2}$  mbar,  $p(\text{NH}_3) = 400$  mbar and  $p(\text{H}_2) = 1000$  mbar at  $900^\circ\text{C}$  [154].

Reaction product	$\text{NH}_3$	$\text{CH}_4$	$\text{GaH}$	$\text{GaCH}_3$	$\text{HCN}$	$\text{H}$	$\text{NH}_2$
Pressure (mbar)	$8 \times 10^{-2}$	$6 \times 10^{-2}$	$10^{-2}$	$5 \times 10^{-3}$	$2 \times 10^{-4}$	$10^{-4}$	$3 \times 10^{-7}$

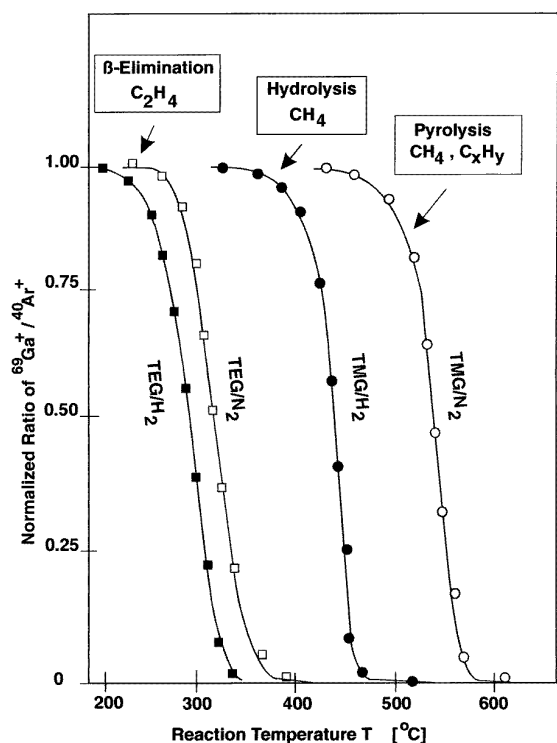


**Figure 23.** The decomposition reactions of  $\text{Me}_3\text{Ga}$  (TMG) and  $\text{Et}_3\text{Ga}$  (TEG) in  $\text{H}_2$  and  $\text{N}_2$ . The concentration of the Ga precursor was measured versus reaction temperature by mass spectrometry and normalized to the partial pressure of argon which was added to the gas phase as reference. It is shown that molecular hydrogen causes a reduction of the  $\text{Me}_3\text{Ga}$  and  $\text{Et}_3\text{Ga}$  reaction temperature [153].

dissociated into inactive  $\text{N}_2$  and  $\text{H}_2$  molecules close to the substrate surface at the growth temperature. From a thermodynamic evaluation, Beaumont *et al* determined that a residual  $\text{NH}_3$  pressure below 0.1 mbar remains at the growth temperature, whereas active molecules like  $\text{NH}$ ,  $\text{NH}_2$  or  $\text{N}$  are at a level below  $10^{-6}$  mbar. Therefore the growth mechanism most likely involves dissociative adsorption of  $\text{NH}_3$  molecules [155,156], which is another reason for the beneficial effects of high V/III gas phase ratios. Significant concentrations of  $\text{CH}_4$ ,  $\text{GaCH}_3$ ,  $\text{HCN}$  and  $\text{H}$  in the gas phase were calculated (table 9), which can be the sources for carbon and hydrogen incorporation into the growing GaN film. At temperatures higher than  $900^\circ\text{C}$ , the formation of gallium hydrides is proposed, preventing the formation of solid GaN and resulting in a reduced deposition rate.

To study the role of hydrogen used as transport gas experimentally, polycrystalline and epitaxial GaN were deposited on  $c\text{-Al}_2\text{O}_3$  substrates without a buffer layer

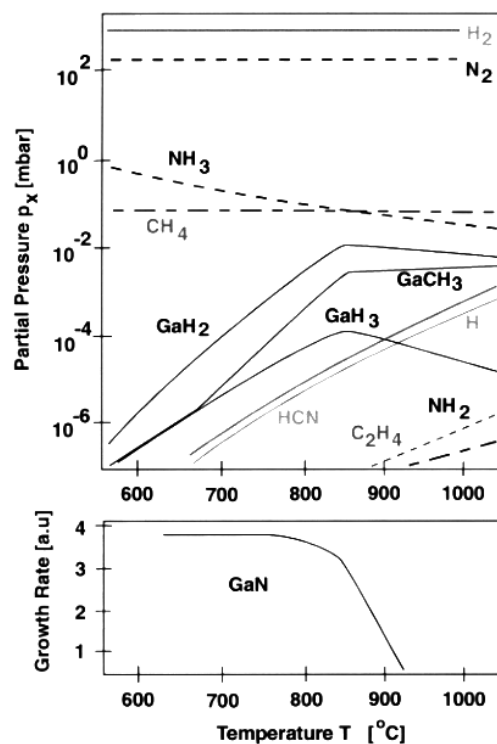


**Figure 24.** Temperature dependence of equilibrium partial pressures of the gaseous  $\text{Me}_3\text{Ga}/\text{NH}_3/\text{H}_2$  system (starting conditions:  $p(\text{Me}_3\text{Ga}) = 10^{-2}$  mbar,  $p(\text{NH}_3) = 400$  mbar,  $p(\text{H}_2) = 1000$  mbar) [154].

by MOCVD, reacting  $\text{Et}_3\text{Ga}$  with  $\text{NH}_3$  in the presence of nitrogen and/or hydrogen [157]. The  $\text{Et}_3\text{Ga}$  flux was fixed at  $1.15 \mu\text{mol}/\text{min}$ , causing a partial pressure of  $1.1 \times 10^{-3}$  mbar at the substrate surface. The substrate temperature ranged from  $600^\circ\text{C}$  to  $1100^\circ\text{C}$ . In figure 25 the deposition rate of GaN versus substrate temperature is shown. The deposition rate increases from  $0.6 \mu\text{m h}^{-1}$  to  $1.5 \mu\text{m h}^{-1}$  when the temperature is increased from  $600^\circ\text{C}$  to  $900^\circ\text{C}$ , caused by the more efficient pyrolysis of  $\text{Et}_3\text{Ga}$  at higher temperatures. For substrate temperatures above  $900^\circ\text{C}$  the deposition rate is constant, indicating that the transport-limited growth regime is reached. If  $\text{H}_2$  is added to the gas phase with a partial pressure of 25 mbar, the growth rate is reduced by approximately 50%, probably due to the change of gas phase reactions caused by hydrogen. Figures 26 and 27 show optical microscope images of the GaN surfaces. The samples were grown under the deposition conditions mentioned above at a substrate temperature of  $950^\circ\text{C}$ . Without hydrogen as the transport gas, a mosaic structure of hexagonal GaN crystals of size  $3 \mu\text{m}$  can be identified (figure 26). When hydrogen is added to the gas phase (figure 27), the deposition rate is reduced from 2 to  $1 \mu\text{m h}^{-1}$  and the crystal shape



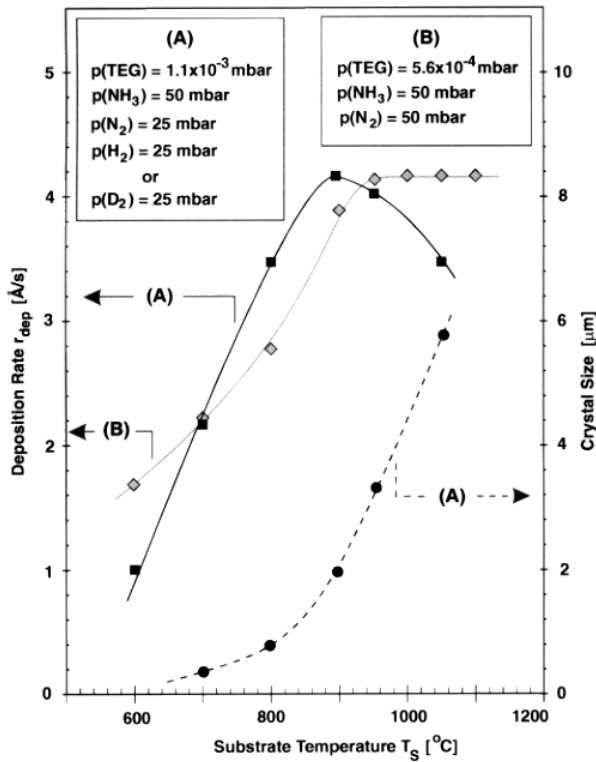


**Figure 25.** Deposition rate and crystallite size of GaN grown by MOCVD on  $c\text{-Al}_2\text{O}_3$  using  $\text{Et}_3\text{Ga}$  and  $\text{NH}_3$  as a function of the substrate temperature. The total gas flow rate through the vacuum chamber was constant at 5000 sccm, producing a gas velocity of  $50 \text{ cm s}^{-1}$  at a pressure of 100 mbar for all deposition experiments. The flow rate of  $\text{NH}_3$  gas was maintained at 2500 sccm. Ammonia and hydrogen gases were diluted with molecular nitrogen to achieve a constant gas velocity with a flow rate of 1250 sccm or, when no hydrogen was used, 2500 sccm [157].

changes to circular, with diameters of  $3\text{--}5 \mu\text{m}$ . In order to reach the same growth rate and to compare the optical and structural properties of GaN films grown with and without hydrogen, the flux of  $\text{Et}_3\text{Ga}$  was increased to  $2.2 \mu\text{mol/min}$ . By changing the substrate temperature from  $600$  to  $900^\circ\text{C}$  the growth rate increased from  $0.35$  to  $1.5 \mu\text{m h}^{-1}$ , but decreased with higher temperatures, possibly due to the formation and desorption of  $\text{GaH}_x$  from the growing surface. The crystal size of the hexagonal GaN deposited in the presence of hydrogen (as determined by scanning electron microscopy (SEM) and atomic force microscopy (AFM)) increases rapidly from  $1$  to  $6 \mu\text{m}$  in the temperature range from  $900$  to  $1100^\circ\text{C}$ . The epitaxial GaN layer grown with hydrogen used as transport gas had a smoother surface (RMS roughness  $< 10 \text{ nm}$ ) and a sharper XRD rocking curve (FWHM:  $300 \text{ arcsec}$  with hydrogen,  $700 \text{ arcsec}$  without hydrogen), indicating improved structural quality in the presence of hydrogen.

Hydrogen used as the transport gas can also significantly affect the composition of Group III-nitride alloys grown by MOCVD, as Piner *et al* [158] and Scholz *et al* [159] found for the In content of InGaIn films grown by low-pressure MOCVD or atomic layer epitaxy (ALE).

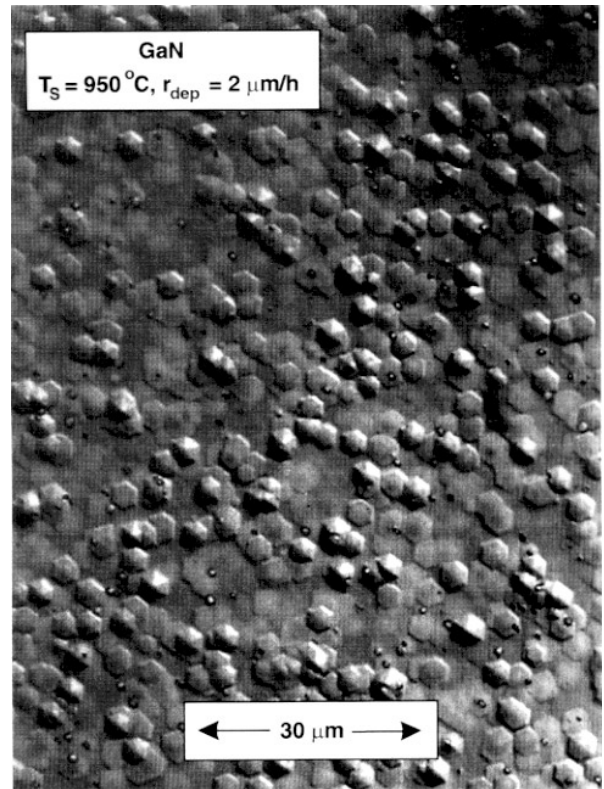


**Figure 26.** Surface micrograph of GaN grown under the deposition conditions mentioned in the text, at a substrate temperature of  $950^\circ\text{C}$ , without use of hydrogen as transport gas. The mosaic structure of hexagonal GaN crystals of size  $3 \mu\text{m}$  can be identified.

For growth temperatures close to  $700^\circ\text{C}$  and a constant set of growth conditions, an increase of up to 40% indium in InGaIn was achieved by reducing the hydrogen partial pressure from 20 to 2 mbar (figure 28). Furthermore an increase of In incorporation with decreasing hydrogen partial pressure was observed for substrate temperatures up to  $800^\circ\text{C}$ , whereas the total concentration of In for a given partial pressure of hydrogen was increased by lowering the temperature. At this time, any effort to explain why hydrogen affects indium incorporation would be speculation. However, hydrogen may have an effect on the lifetime of the reactive indium species at the surface [160]. If hydrogen were to shorten the lifetime (due, for example, to the formation of gaseous  $\text{InH}_x$ ) the surface would be reduced with increased hydrogen partial pressure and increasing temperature, thereby reducing the amount of indium being incorporated into the growing film. Another possibility is that hydrogen affects the concentration of contaminants at the growing surface, such as carbon, which could in turn affect the In content of InGaIn. Apart from hydrogen partial pressure and the substrate temperature, In incorporation can be influenced by the strain and the structural properties of the epitaxial layers [161], which can be controlled by the pretreatment of the substrate and the deposition of nucleation and buffer layers as discussed in the next section.

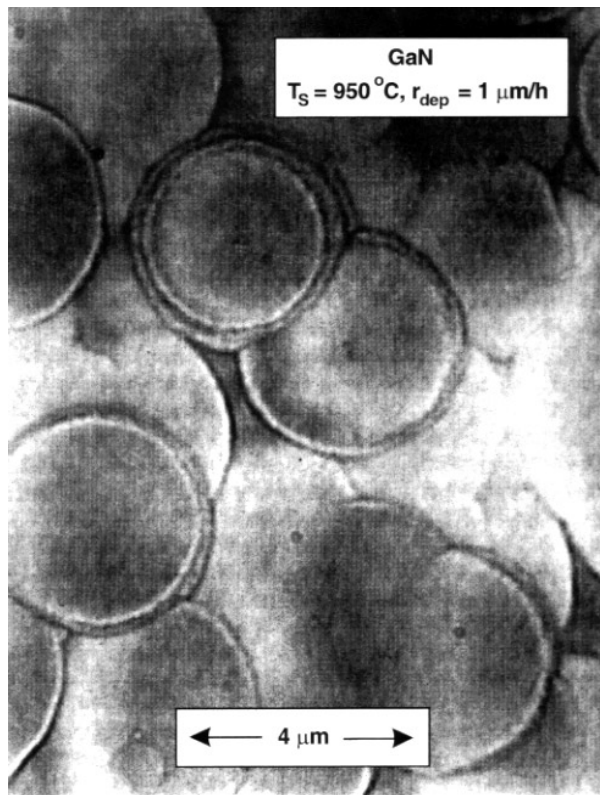


**Figure 27.** Surface micrograph of GaN grown under the deposition conditions mentioned in the text, at a substrate temperature of 950 °C. When hydrogen is added to the gas phase, the deposition rate is reduced from 2 to 1  $\mu\text{m h}^{-1}$  and the crystals become circular with diameters of 3 to 5  $\mu\text{m}$ .

**4.5.2. Buffer and nucleation layers, nitridation of sapphire.** Until 1985, hexagonal GaN grown by MOCVD was deposited directly on sapphire substrates. The fabricated epitaxial GaN films had rough surfaces mainly caused by the three-dimensional growth mode, which resulted in the surface morphology shown in figure 26. In 1986, Amano *et al* succeeded in remarkably improving the surface morphology as well as the electrical and optical properties, by deposition of a 50 nm thick AlN film on  $c\text{-Al}_2\text{O}_3$  as a nucleation layer, before GaN film growth by MOCVD [162]. An AlN layer was deposited at 600 °C and the succeeding GaN at 1000 °C. The surface morphology of the GaN film was improved to a flat surface (RMS roughness  $\leq 1$  nm) free from cracks. The FWHM of the double-crystal x-ray rocking curve (0002), obtained for optimum conditions, was 110 arcsec [163]. The photoluminescence spectrum measured at 4 K showed a very sharp donor-bound exciton line ( $D^0X$  FWHM = 1.1 meV) and sometimes a free exciton line as well. The electron concentration was reduced below  $10^{17} \text{ cm}^{-3}$  and the electron mobility was increased to  $600 \text{ cm}^2 \text{ V}^{-1} \text{ s}^{-1}$  at room temperature. The temperature dependence of the mobility suggested that it was limited by optical phonon scattering at high temperatures and by ionized impurity scattering at low temperatures.

TEM and SEM were used to clarify the growth mechanism connected with the AlN buffer layer. TEM

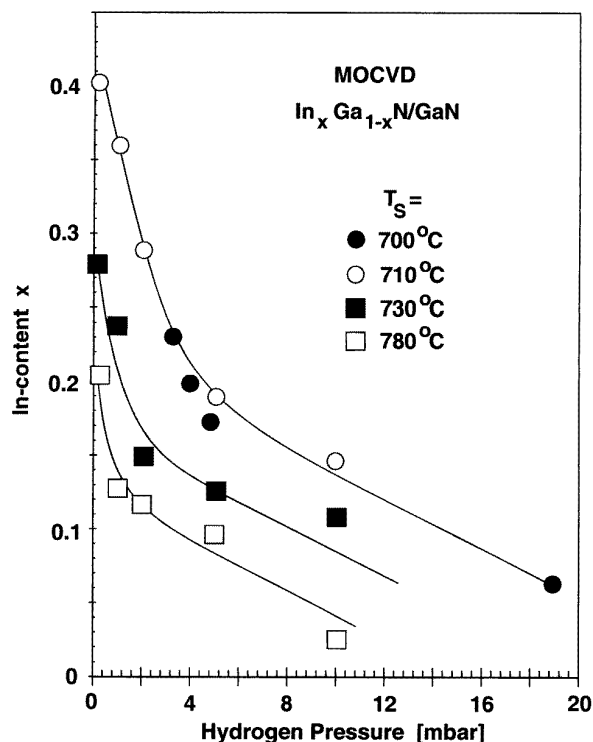


**Figure 28.** In content of MOCVD grown InGa<sub>1-x</sub>N/GaN layers (deposited on GaN) at substrate temperatures between 700 and 780 °C versus the partial pressure of hydrogen during the growth (full circles [158], other symbols [159]).

revealed that GaN has many defects near the GaN/AlN interface, composed of fine columnar crystals and trapezoidal crystals, but the defect density decreases abruptly after a GaN thickness above 300 nm [164]. From knowledge of the fine structure of the GaN/AlN interface, a growth mechanism consisting of the following stages was proposed: generation of nucleation crystallites by depositing a thin low-temperature AlN layer, geometric selection of the crystallographic direction of the columnar crystals and the formation of islands through high-temperature GaN growth, and the coalescence of the islands by the high lateral growth velocity of the trapezoidal islands resulting in a quasi-two-dimensional growth. The growth process is shown schematically in figure 29 [164]. The essential role of a low-temperature buffer layer is both to supply nucleation centres having the same orientation as the substrate and to promote lateral growth of the GaN film due to the decrease in interfacial free energy between the film and the substrate.

The successful concept of low-temperature nucleation or the use of a buffer layer was also used by Nakamura [165]. Nakamura developed the low-temperature deposited GaN nucleation layer method for the growth of epitaxial GaN, having essentially the same principle as that of the AlN nucleation layer technique, to produce the LEDs described in section 9.4 (figure 30). It has been reported that the crystallographic perfection of the GaN nucleation layers is poor but improves during heating to the growth temperature of the epitaxial GaN layer, commonly close to



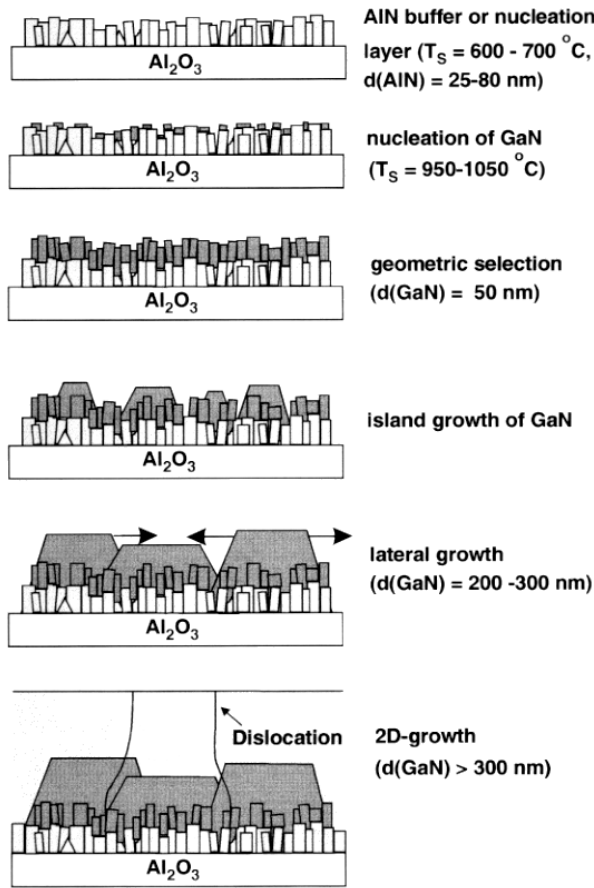


**Figure 29.** Schematic diagram of the growth process proposed by Hiramatsu *et al* [164].

1000 °C [166]. George *et al* [167] and Wu *et al* [168] employed TEM and AFM to examine the as-deposited and thermally annealed nucleation layer. Both reports made the same observation that the average grain size and rms roughness of the nucleation layers increased at the end of the annealing temperature ramp. Grains of comparable size to the as-grown layers persist, along with much larger grains. The formation of these larger grains during annealing causes an improvement in the structural quality of the layer. Keller *et al* [169] speculated that achieving an optimum nucleation layer is a balance between surface roughness and internal defect structure. The defect structure of the nucleation layer significantly influences the dislocation reaction mechanism in the epitaxial GaN film grown on top and therefore the crystallographic quality of the sample.

A further improvement of the structural quality of GaN can be realized with an initial nitridation of the  $\alpha\text{-Al}_2\text{O}_3$  substrate surface using  $\text{NH}_3$  or  $\text{N}_2$  radicals [170–172]. Moustakas *et al* [173] reported that a relaxed AlN layer is formed at 850 °C by exposing the  $\text{Al}_2\text{O}_3$  surface to a nitrogen plasma produced by electron cyclotron resonance (ECR). An improvement in the optical and electrical properties of GaN using nitrided sapphire substrates (10 min, 850 °C,  $\approx 10^{-5}$  mbar  $\text{NH}_3$ ) has also been reported [174, 175]. The conversion of the sapphire surface into

AlN was confirmed by observing that the relaxation of the GaN layer corresponded exactly to the lattice mismatch between GaN and AlN. Uchida *et al* [176] formed a nitrided layer on (0001) sapphire by heating at 1050 °C in  $\text{NH}_3$ . The intensity of the  $\text{N}_{1s}$  peak measured by XPS increased rapidly with nitridation time, reaching saturation in a few minutes. This change was found to correspond to a morphological change revealed by AFM observations, from a flat nitrided layer to high-density ( $10^9\text{--}10^{10}\text{ cm}^{-2}$ ) nitrided protrusions. TEM and EDX measurements showed that the nitridation forms an amorphous layer consisting of  $\text{AlN}_x\text{O}_{1-x}$ . These observations indicate that the source for nitrogen radicals (plasma source,  $\text{NH}_3$ ), the annealing time and the temperature are important parameters for the creation of an AlN layer by conversion of  $\text{Al}_2\text{O}_3$ . Keller *et al* [177] demonstrated a reduction of the dislocation density to  $4 \times 10^8\text{ cm}^{-2}$  by using the combination of  $\text{Al}_2\text{O}_3$  surface nitridation and a low-temperature GaN nucleation layer. Nitridation of the substrate for 60 s at atmospheric pressure and a substrate temperature of 1050 °C followed by the deposition of a 19 nm thick low-temperature GaN nucleation layer results in a reduction of dislocation density by a factor of about a hundred and an increase of electron mobility up to  $650\text{ cm}^2\text{ V}^{-1}\text{ s}^{-1}$  ( $n_e = 2 \times 10^{17}\text{ cm}^{-3}$ ). Under such conditions, short ammonia preflow times (about 1 min) lead to as-grown nucleation layers that are rough, highly faceted and predominantly cubic GaN. This structure is largely sustained after heating to a growth temperature of about 1000 °C. Long ammonia preflow times (about 10 min) lead to similar nucleation layers, except that there is an approximately 5 nm thick hexagonal GaN layer that fully wets the substrate. Upon heating this nucleation layer becomes smooth and hexagonal. The significant reduction of the dislocation density obtained for the rough nucleation layer can be a consequence of reactions between pure edge treading dislocations and Shockley partial dislocations that bound the stacking disorder in the nucleation layer.

The reduction of dislocation density leads to great improvement in the electrical and optical properties needed for the development of devices.

**4.5.3. Selective epitaxial growth and lateral overgrowth of GaN by MOCVD.** Another possibility to reduce the high dislocation density of heteroepitaxial GaN is lateral overgrowth. The lateral epitaxial overgrowth (LEO) technique consists of partially masking a substrate or seed layer and subsequently regrowth over the masked substrate. The potential of LEO for extended defect reduction in the heteroepitaxial growth of III–V semiconductors has been demonstrated in material systems such as GaAs on Si [178, 179], InGaAs on GaAs [180] and InP on Si [181]. Furthermore, selective epitaxial growth enables the controlled deposition of low-dimensional microstructures such as quantum wires and dots [182, 183]. This technique does not cause any damage or contamination of the sample surface, in contrast to patterning by dry etching.

For GaN lateral overgrowth on sapphire, the first step is to grow a conventional low-temperature nucleation layer followed by the deposition of 1–2  $\mu\text{m}$  of GaN at high temperatures by MOCVD as described above. This

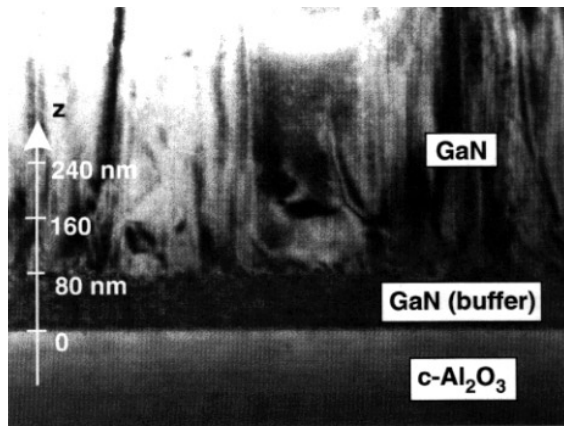


**Figure 30.** Transmission electron microscopy (bright field) cross section of an epitaxial GaN film deposited on  $c\text{-Al}_2\text{O}_3$  using a GaN low-temperature buffer layer. The buffer layer and the high concentration of structural defects (dislocations) in the epitaxial film are visible. The concentration of structural defects decreases with increasing distance from the interface GaN(nucleation layer)/GaN.

produces a GaN surface containing  $10^8\text{--}10^{10}$  dislocations per  $\text{cm}^2$  [184]. The next step is to cover the entire wafer with 100–200 nm of amorphous  $\text{SiO}_2$  or  $\text{Si}_3\text{N}_4$  with *ex situ* techniques such as sputtering, plasma-enhanced chemical vapour deposition (PECVD) or *in situ* by MOCVD using silane and ammonia as precursors [185]. Windows in the  $\text{SiO}_2$  or  $\text{Si}_3\text{N}_4$  layer can be produced by conventional photolithography and etching with hydrofluoric acid (HF) to expose stripes of GaN separated by stripes of the mask or to fabricate a grid of small holes. Prior to lateral overgrowth, the patterned samples are dipped in a 50% buffered HCl solution to remove the surface oxide of the underlying GaN layer.

Regrowth of GaN on such patterned samples takes place under conditions similar to those used for standard GaN growth except for the Ga precursor flow rates. These are set to smaller values to avoid excessively high growth rates resulting from the very efficient collection of Ga atoms on the structured surface. At first, the deposited high-temperature GaN grows selective within the windows more rapidly than it grows on the surrounding dielectric mask, due to a much higher sticking coefficient of the metalorganic precursor and because of the Ga adatoms on the GaN surface rather than on the mask. This is the expected result, as the  $\text{SiO}_2$  and  $\text{Si}_3\text{N}_4$  bond strengths are  $800\text{ kJ mol}^{-1}$  and  $440\text{ kJ mol}^{-1}$  respectively, much higher than those of Ga–N ( $103\text{ kJ mol}^{-1}$ ) or Ga–O ( $353\text{ kJ mol}^{-1}$ ) [186]. Thus it would be unlikely for Ga adatoms to bond to the mask surface in sufficient numbers and for long enough to cause GaN nuclei to form. They would either evaporate or diffuse along the surface to the opening in the mask or to the vertical GaN surfaces which have emerged.

The process of selective growth and the first step of lateral overgrowth of GaN was first experimentally demonstrated and schematically illustrated by Kato *et al* (figure 31) [187]. The observations discussed here were achieved with a  $\text{SiO}_2$  mask patterned to form linear

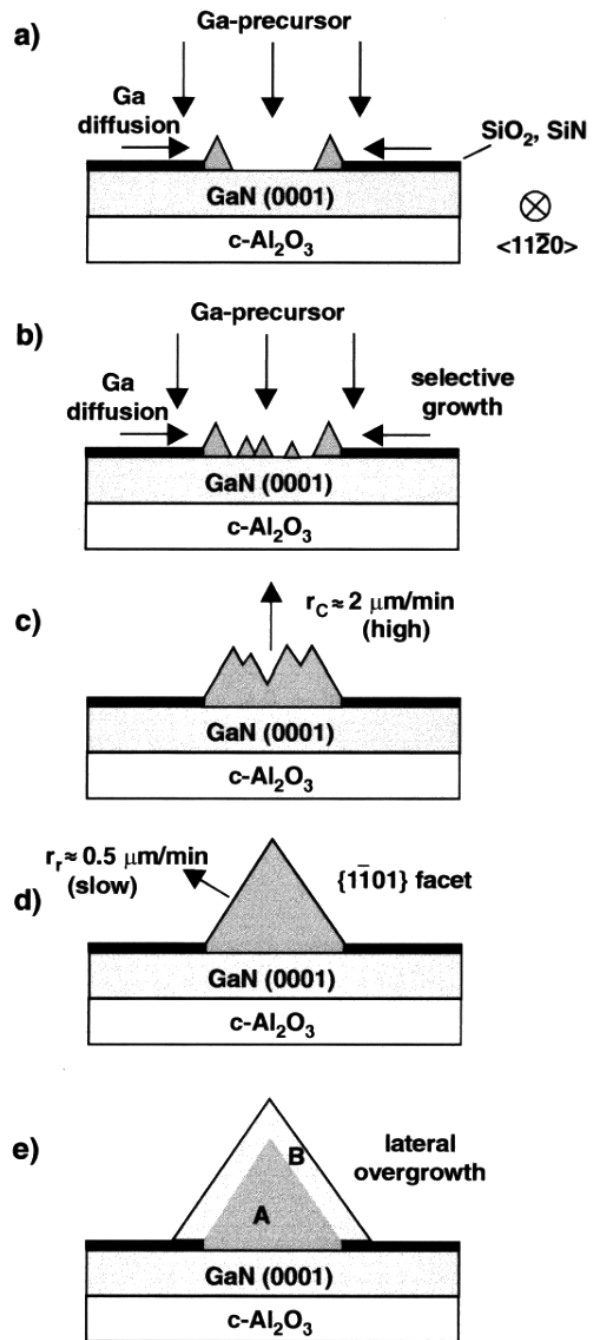


**Figure 31.** Schematic drawing indicating the facet formation process of GaN during selective growth [187].

windows with lengths extending in the  $\langle 11\bar{2}0 \rangle$  direction with widths of  $10\text{ }\mu\text{m}$ . Starting the high-temperature selective growth of GaN on the masked seed layer,  $2\text{ }\mu\text{m}$  wide ridges are first formed at the edges of the window, indicating that the nucleation occurs preferentially at the edges of the mask. In the initial growth stage (figure 31(a)), the source gas concentration becomes high at the ridge region because of the lateral vapour diffusion and the Ga surface diffusion into the window region. Furthermore, the edges of the mask can serve as nucleation centres of GaN. After ridge growth, GaN islands are generated between the

two ridges in the window. Coalescence occurs among the islands, forming a rough structure with many pits on the top. Then, the rough surface on the top grows with high rates in the [0001] direction but the  $\{1\bar{1}01\}$  facets on the side do not grow significantly. The growth rate of these facets is slow because they have stable surfaces. Finally, the GaN has a simple structure composed of two  $\{1\bar{1}01\}$  facets with a length comparable to the widths of the striped window. If growth continues, the facets start to grow over the mask surface in the lateral direction (lateral overgrowth). If the mask is patterned to create holes instead of stripes, the  $\{1\bar{1}01\}$  facets form GaN pyramids with a hexagonal cross section.

Zheleva *et al* [186] evaluated the structural defects in such GaN pyramids. In region A (figure 31(e)) located above the window area, the dislocations have a density comparable to that of the GaN seed layer. Most of the extended dislocations propagate in the growth direction through the GaN. The dislocation density is drastically reduced within a pyramidal volume which ends at approximately one third of the pyramid height. Region B of the triangular or pyramid structure above the mask area surrounding the window, and resulting from lateral growth, is nearly free of observable dislocations. Very few short edge-on dislocations segments parallel to the interface plane and only a few overlapping stacking faults in the vicinity of the GaN/mask interface were observed. High-resolution TEM from the top and from the  $(1\bar{1}01)$  sidewalls of the structures revealed regions essentially free of dislocations.

Marchand *et al* [188] used a 2  $\mu\text{m}$  thick MOCVD GaN layer with a dislocation density of about  $5 \times 10^8 \text{ cm}^{-2}$ , coated with a 200 nm  $\text{SiO}_2$  mask and patterned with 5  $\times 10 \mu\text{m}$  wide stripes as a seed layer. Following the results of Kapolnek *et al* [189], the stripes were oriented in the  $\langle 1\bar{1}00 \rangle$  direction in order to yield a large lateral growth rate. The stripe spacing was varied to give ratios of open width to patterned period of 0.1 to 0.5. Under the chosen growth conditions, the overgrown GaN is bound on top by the (0001) facet and on the edges by vertical  $\{11\bar{2}0\}$  sidewalls, which showed a lateral growth rate of up to  $6 \mu\text{m h}^{-1}$ . Patterns with 10  $\mu\text{m}$  stripes and a ratio of open width to patterned period of 0.5 enabled full coalescence of the overgrown GaN film after 90 min of growth. TEM and AFM observations indicated that the density of mixed character dislocations reaching the surface of the LEO GaN is in the  $10^4$ – $10^5 \text{ cm}^{-2}$  range. The density of pure screw and mixed character threading dislocations in good MOCVD GaN material is about  $5 \times 10^8 \text{ cm}^{-2}$ . Thus the dislocation density at the surface of the overgrown film is reduced by at least three orders of magnitude relative to that of conventionally grown epitaxial GaN films.

These results demonstrate that LEO is a valuable technique to achieve high-quality epitaxial GaN films suitable as a basis layer for electrical and optical devices. However, much work remains because the electron concentrations in LEO films are measured to be high, probably from Si and/or O impurity diffusion from the mask into the GaN films. Several technical issues are still to be investigated, including the gas phase and surface kinetics of the lateral overgrowth mechanism especially with respect to

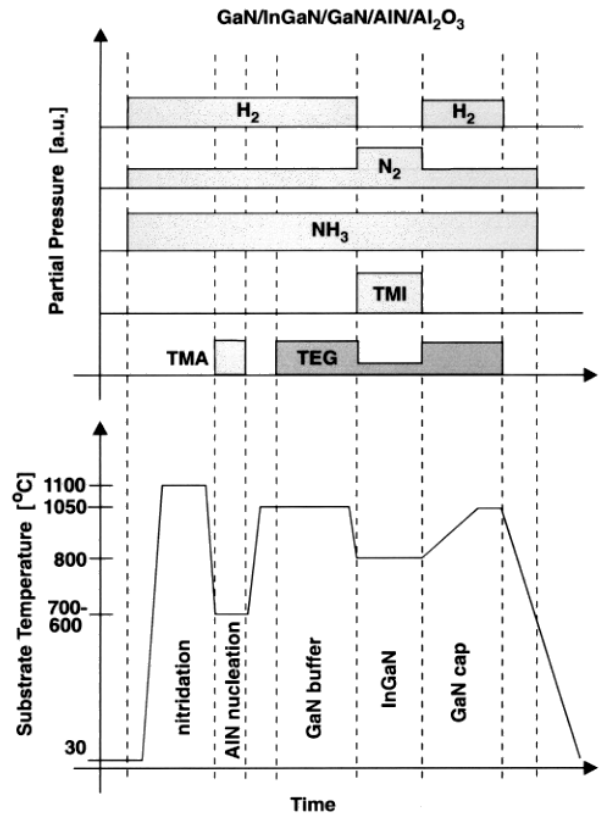


**Figure 32.** Sequence for the growth of a GaN/InGaN/GaN heterostructure using an AlN nucleation layer on top of a nitrided sapphire substrate. The precursors and the growth temperature are changed corresponding to the alloy composition.

enhancing the lateral growth rate, and the nature of strain in the vicinity of the mask and its effect on dislocation propagation. A refined approach to a nearly dislocation-free GaN substrate for devices can be employed by using two successive LEO steps with the mask of the second step positioned over the openings defined by the mask of the first step, thus blocking the defects that grow out of the first windows. This complicated procedure offers the possibility of eliminating the disadvantages of heteroepitaxy in comparison with homoepitaxy and will be important until crystal GaN substrates become available.

#### 4.5.4. Group III-nitride alloys grown by MOCVD.

The growth of InGaN alloys has proven to be extremely challenging, especially for higher concentrations of In in the ternary film ( $>20\%$ ), due to the large difference in interatomic spacing between GaN and InN and the trade-off between the epilayer quality and the amount of In incorporation into the alloy as the growth temperature is changed. Growth using high temperatures of approximately  $800^\circ\text{C}$  typically results in high crystalline quality, but the amount of indium incorporated is limited to low values because of the high volatility of nitrogen and the low decomposition temperature of InN and InGaN. To avoid the large lattice mismatch between InGaN and  $c\text{-Al}_2\text{O}_3$ , most active InGaN layers in devices are grown

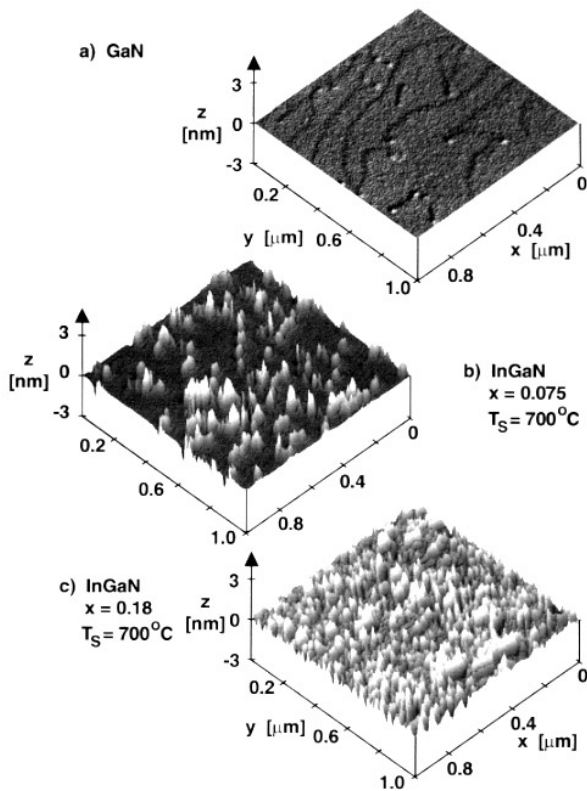


**Figure 33.** Atomic force microscopy measurements of a 2  $\mu\text{m}$  thick GaN film and 100 nm thick InGaN films grown on GaN/AlN/Al<sub>2</sub>O<sub>3</sub> substrates by MOCVD [192].

on high-quality GaN. As a consequence, the deposition temperature has to be changed by more than 200 °C between growths of GaN and InGaN. One procedure to grow a GaN/InGaN/GaN heterostructure by MOCVD using a nitrided sapphire substrate and an AlN nucleation layer is shown schematically in figure 32.

Matsuoka *et al* [190] found that lowering the growth temperature from 800 to 500 °C resulted in an increase of the In content, but at the expense of reduced crystalline quality. Attempts to increase the In concentration by raising the partial pressure of the indium precursor results in a reduction of the structural and surface morphology quality and sometimes in the formation of In droplets on the surface [191]. Figures 33 and 34 show the surface morphology of 100 nm thick GaN and InGaN films obtained by AFM, and the FWHM of the 0002 reflection measured by XRD [192]. These experimental results demonstrate a reduction of structural quality with increasing In content, which is a general observation also made for epitaxial InGaN films grown by other techniques such as sputtering.

Ho and Stringfellow [193] studied the temperature dependence of the binodal and spinodal lines in the InGaN system using a modified valence force field model to predict that, at a growth temperature of 800 °C, the equilibrium solubility of In in GaN would be less than 6%. To explain the experimental results Koukitu *et al* [194] made a thermodynamic analysis of InGaN alloys grown by MOCVD. In contrast to other III–III–V alloy systems where the solid composition is a linear function

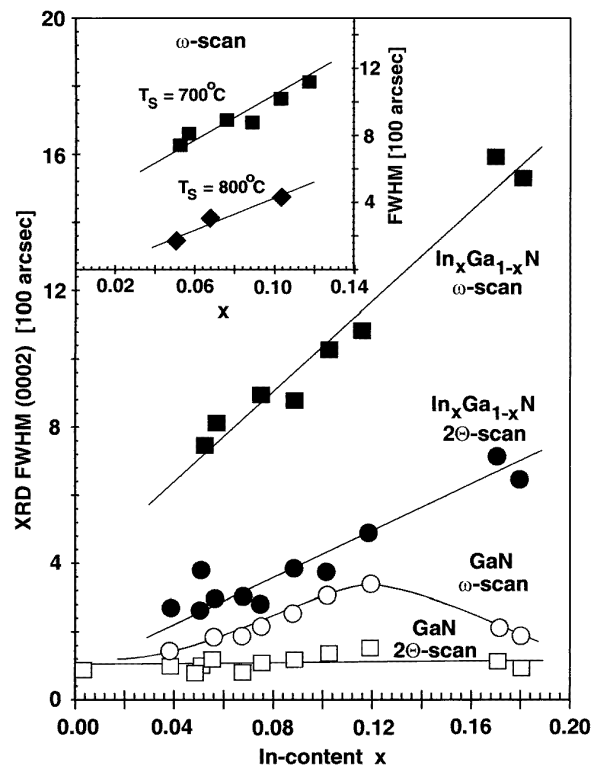


**Figure 34.** FWHM of (0002) x-ray diffraction 2 $\Theta$  and  $\omega$  scans of InGaN/GaN heterostructures versus In content. The insert shows the FWHM of the (0002) rocking curve of 100 nm thick InGaN films grown at substrate temperatures of 700 and 800 °C [192].

of the input mole ratio of the Group III metalorganic precursors at constant partial pressure of Group V gas, the solid composition of InGaN deviates significantly from a linear function at high substrate temperatures. In figure 35, the theoretically predicted compositions of InGaN alloys for different input In and Ga source ratios are compared with the experimental data of Matsuoka *et al* [190] and Sohmer *et al* [192]. For substrate temperatures below 600 °C, the In content increases linearly with the input ratio. Above 600 °C the deviation from the linear relationship increases. The agreement between the experimental and the calculated compositions indicates that the composition of InGaN alloys grown by MOCVD is thermodynamically controlled. One important feature in the figure is that the isothermal lines change in a complex manner at high temperatures. This leads to the conclusion that the deposition of compounds with varying solid compositions is expected for a given ratio of the metalorganic source gases at high substrate temperatures. This effect can be partially reduced by a high input partial pressure of the Group III elements, but is still one important explanation for the observed In fluctuations in InGaN films.

Kawaguchi *et al* [195] reported the InGaN composition pulling effect, where the indium fraction is small at the initial growth stage on a GaN or AlGaIn epitaxial layer and increases with increasing growth thickness, and suggested that this effect is caused by strain due to the lattice mismatch at the interface. It was found that larger

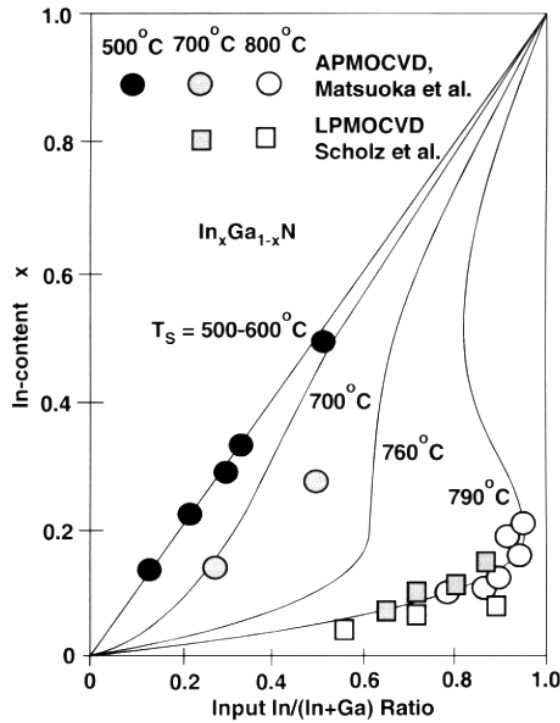


**Figure 35.** Theoretically predicted compositions of InGaN alloys for different input In/(In+Ga) gas phase ratios [194] are compared with experimental data for different substrate temperatures (circles [190], squares [192]).

**Table 10.** General trends of the In content of epitaxial InGaN film growth in dependence of various MOCVD parameters ( $\uparrow$ , increasing;  $\downarrow$ , decreasing;  $\circ$ , weak influence).

MOCVD parameter	In content	
Substrate temperature	$\uparrow$	$\downarrow$
Growth rate	$\uparrow$	$\uparrow$
Input In/(Ga+In) ratio	$\uparrow$	$\uparrow$
Hydrogen partial pressure	$\uparrow$	$\downarrow$
Ammonia partial pressure	$\uparrow$	$\circ$
Total pressure	$\uparrow$	$\circ$
Biaxial compressive stress	$\uparrow$	$\downarrow$

lattice mismatch between InGaN and the bottom epitaxial layers was accompanied by a larger change in In content. This implies that the indium distribution mechanism in InGaN is caused by the lattice deformation due to the lattice mismatch. With increasing thickness, the lattice strain is relaxed due to the formation of structural defects, which weakens the composition pulling effect. Table 10 summarizes general trends between deposition parameters and structural qualities and the In incorporation in InGaN.

The deposition of AlGaN alloys by MOCVD is much easier than the growth of InGaN because of the smaller differences in lattice mismatch, ionic radii, chemical reactivity with nitrogen and higher thermal stability. Bremser *et al* [3] and Ruffenach-Clur *et al* [196] reported growth of AlGaN films over the whole range of compositions at substrate temperatures between 980 and 1150 °C. In contrast to In incorporation, Ruffenach-Clur

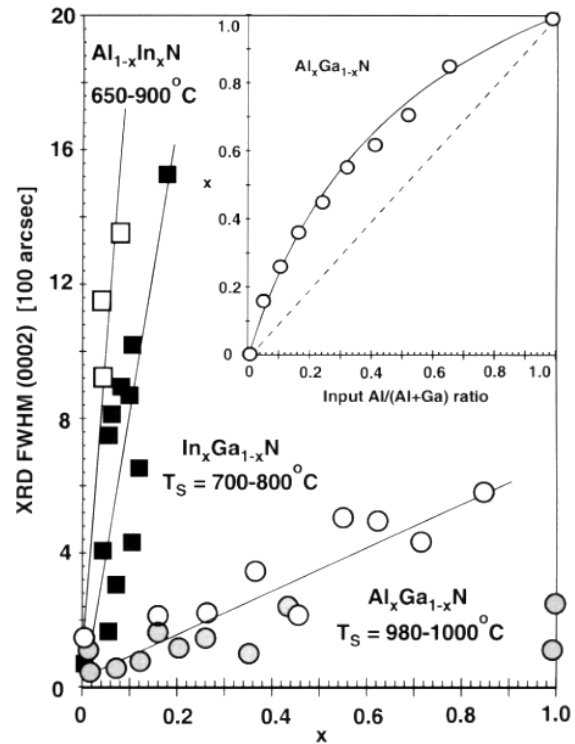


**Figure 36.** FWHM of (0002) x-ray diffraction  $\omega$ -scans of AlGa<sub>x</sub>N, InGa<sub>x</sub>N and AlInN alloys in dependence of the composition  $x$  (black squares [192], white squares [5], white circles [196] and grey circles [197]). The insert shows the Al content  $x$  of AlGa<sub>x</sub>N alloys for different input Al/(Al+Ga) gas phase ratios.

*et al* observed a high efficiency of Al incorporation in AlGa<sub>x</sub>N films grown at 1000 °C. The Al content at a given input Me<sub>3</sub>Al/(Me<sub>3</sub>Al + Me<sub>3</sub>Ga) ratio is above the linear dependence (dotted line in the inset of figure 36) for all compositions. Nevertheless, the structural quality of the AlGa<sub>x</sub>N films observed by Ruffenach-Clur *et al* and Kung *et al* [197] decreased with increasing Al content. The FWHM of the XRD (0002) rocking curve (figure 36) broadened up to 9 arcmin for Al<sub>0.85</sub>Ga<sub>0.15</sub>N. Bremser *et al* [3] determined the optimum growth temperature for AlGa<sub>x</sub>N films with  $x$  above 0.5 to be around 1130 °C. From the published data, one can speculate that the substrate temperature for the deposition of Al<sub>x</sub>Ga<sub>1-x</sub>N films by MOCVD should be increased linearly with  $x$  from 1000–1050 °C at  $x = 0$  to about 1150 °C for  $x = 1$ .

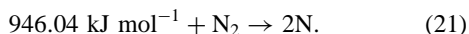
Only a very limited number of publications concerning the deposition of AlInN films, which can be used for growing lattice-matched AlInN/AlGa<sub>x</sub>N or AlInN/InGa<sub>x</sub>N heterostructures, are available. The problems of growing AlInN alloys are similar to or even greater than (higher differences in lattice spacing, thermal stability) those experienced in the deposition of InGa<sub>x</sub>N films. Kim *et al* [5] deposited thin AlInN films with x-ray rocking curve FWHM values between 10 and 20 arcmin. They observed an increase of In content in AlInN of up to 8% by lowering the substrate temperature to 600 °C. A further reduction of substrate temperature during MOCVD is not useful because of the needed efficient pyrolysis of ammonia.

One growth technique which enables the deposition of Group III-nitrides at a lower substrate temperature (because nitrogen radicals are not produced by the thermal cracking of ammonia) is PIMBE. MBE is a growth process operating at relatively low temperatures and far from thermodynamic equilibrium and thus has a chance to improve In incorporation and the structural properties of InGaN and AlInN alloys.

#### 4.6. Plasma-induced molecular beam epitaxy (PIMBE)

MBE is a versatile technique for growing thin epitaxial structures made of semiconductors, metals or insulators. In MBE, thin films crystallize via reactions between thermal molecular or atomic beams of the constituent elements and a substrate surface which is maintained at an elevated temperature in ultrahigh vacuum. The composition of the grown epilayer and its doping level depend on the arrival rates of the constituent elements and dopants. The typical growth rate of 1 monolayer per second ( $\text{ML s}^{-1}$ ) is low enough for surface migration of the impinging species on the growing surface to be possible. MBE growth is carried out under conditions far from thermodynamic equilibrium, and is governed mainly by the kinetics of the surface processes occurring when the impinging beams react with the outermost atomic layers of the substrate crystal. This is in contrast to other epitaxial growth techniques, such as liquid phase epitaxy (LPE) or MOCVD, which proceed at conditions near thermodynamic equilibrium and are most frequently controlled by diffusion processes occurring in the crystallizing phase surrounding the substrate [198].

For nitride growth, the effusion of the metal atoms (Ga, In, Al) and dopants (Si, Mg) from conventional Knudsen effusion cells has to be combined with a source for nitrogen radicals. Nitrogen at room temperature is an inert gas and not very reactive, because of the triple bond between the two nitrogen atoms. The dissociation of one molecule into reactive nitrogen atoms requires a relatively high amount of energy:



Under the influence of a plasma at reduced pressure, a significant dissociation of the nitrogen molecules takes place, as reported by Strutt in 1913 [199–201]. Atomic nitrogen is chemically very active at room temperature and bonds with many metals (mercury, zinc, cadmium, magnesium) creating various nitrides (for example  $3\text{Mg} + 2\text{N} \rightarrow \text{Mg}_3\text{N}_2 + 1408 \text{ kJ mol}^{-1}$ ). Therefore Group III-nitrides can be grown by plasma-assisted molecular beam epitaxy, where the plasma-induced fragmentation of nitrogen molecules is combined with the evaporation of metal atoms from effusion cells.

Moustakas *et al* reported the growth of GaN by electron cyclotron resonance microwave-plasma-assisted molecular beam epitaxy (ECR-MBE) [173]. The deposition system consists essentially of a MBE chamber unit with a compact ECR source (figures 37 and 38(a)) [202] mounted in one of the effusion cell ports. Johnson and co-workers reported on the growth of GaN, AlGaIn and AlN on GaN/SiC substrates [203]. A rf plasma source (13.56 MHz) (figure 38(b)) [204]

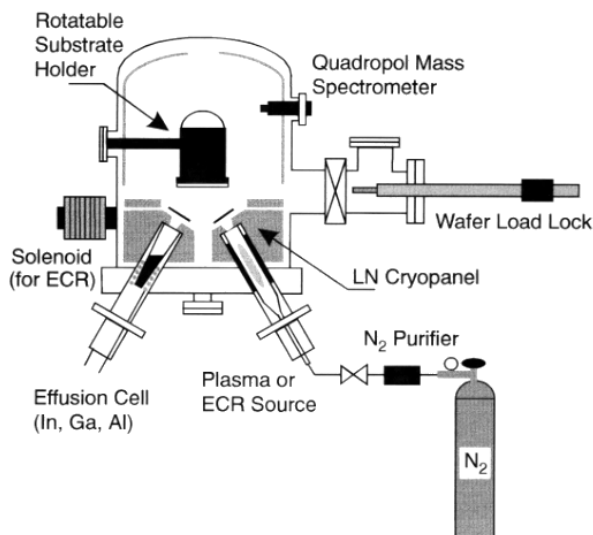


**Figure 37.** Molecular beam epitaxy chamber with a compact electron cyclotron resonance (ECR) source mounted in one of the effusion cell ports. Conventional effusion cells are used for the evaporation of the Group III elements as well as for the dopants. Active nitrogen is produced by passing molecular nitrogen through the plasma source.

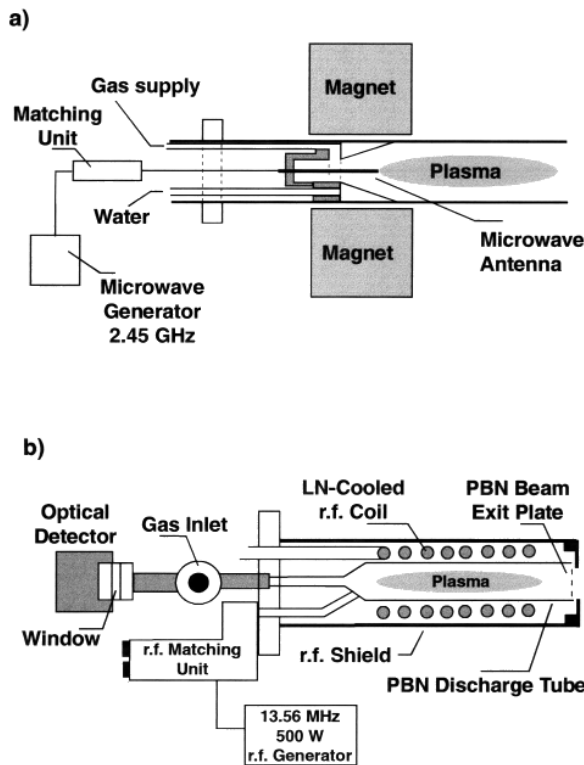


**Figure 38.** (a) Schematic diagram of an ECR source (2.45 GHz) [203] and (b) rf plasma source (13.56 MHz) for producing nitrogen radicals [204].

was used to generate an active nitrogen flux. The plasma sources are operated at nitrogen flow rates which produces a downstream pressure in the MBE chamber of  $5 \times 10^{-6}$  to

$4 \times 10^{-4}$  Torr (base pressure of the chamber  $\leq 10^{-10}$  Torr). The rf plasma can be operated at powers between 150 and 600 W and pressures of 10–100 Torr. The design of the sources promotes efficient electron–nitrogen collisions and results in a high-density plasma with gas ionization efficiencies as high as 10%.

The growth is carried out in the molecular flow regime, where the transport of atoms or molecules in both thermal beams from the effusion cells as well as the beam of activated nitrogen from the plasma source occurs in a collisionless manner. The nitrogen ions created by the plasma sources are poorly confined and reach the substrate because of the pressure difference between the plasma cell and the MBE chamber and perhaps due to attraction by negatively charged substrate [205]. If an ECR source is used, the kinetic energy of the nitrogen ions can be high and displacement of bulk atoms becomes important. The damage threshold of GaN was estimated to be 24 eV [32]. Therefore highly energetic ions leaving the ECR source are diverted from the substrate surface by a magnetic field induced by an external solenoid. Nitrogen radicals leaving the rf plasma source have energies in the region of 2 eV so radiation damage can be neglected.

The starting procedure of GaN deposition by MBE can be very similar to that of the MOCVD process. The first step is cleaning and can be carried out by nitridation of the sapphire substrate in vacuum, by exposing the substrate to a nitrogen plasma at 800 °C for approximately 10 min. The exact mechanism of this nitridation is not well understood, but Moustakas and co-workers observed a thin single crystal film with atomically smooth surface morphology, as indicated by the streakiness of a RHEED pattern. A second possible step is the deposition of a thin GaN nucleation layer (20–30 nm thick) at 550 °C but, in the case of PIMBE, high-quality GaN films have also been grown without any low-temperature nucleation layer [206]. The third step involves the deposition of the epitaxial GaN film at about 700–800 °C. The Ga flux during the growth of GaN is about  $10^{15} \text{ cm}^{-2} \text{ s}^{-1}$  and this results in growth rates between 0.5 and  $1 \mu\text{m h}^{-1}$ .

GaN layers grown with a low III/V flux ratio (N-stable growth) display a faceted surface morphology and a tilted columnar structure with a high density of stacking faults [207]. Under Ga-rich conditions, a dramatic reduction of surface roughness and improvements in structural and electrical properties are observed. Ga-rich conditions (Ga flux close to the value where Ga droplets are formed) appear to promote step flow growth, in which condensing material reaches the growth ledges by surface diffusion before new islands nucleate [208]. GaN films grown under Ga-rich conditions on (0001) sapphire were found to have good structural quality as documented by the x-ray rocking curve FWHM of down to 69 arcsec. MBE GaN growth under N-stable conditions would be expected to result in extended regions in which the surface is terminated primarily by N atoms. Neglecting surface reconstruction, each surface N atom has one bond to the underlying Ga and three available bonds. This high density of dangling bonds should significantly reduce the Ga adatom surface mobility due to the number of Ga–N bonds which must be

partly broken and reformed in order for surface diffusion to occur. In the limiting case where the surface diffusion length is less than the hopping distance between adjacent bonding sites, GaN growth can occur, leading to statistical roughening of the surface and a characteristic columnar structure [207, 209].

The number of structural defects present is reduced significantly for the case of Ga-stable conditions, where the step flow growth mode dominates. In this case the adatoms have a large surface diffusion length and thus move relatively freely within a terrace until incorporation at a step edge. The diffusion length of adatoms increases with increasing substrate temperature, but the surface residence time of adatoms will decrease due to enhanced evaporation. Guha *et al* [210] measured the residence lifetime of Ga adatoms on a GaN surface by mass spectrometry to be between 0.6 and 5 s in the temperature range 695–750 °C. The Ga evaporation rate at 830 °C and the activation energy of Ga desorption was determined to be  $3\text{--}4 \text{ ML s}^{-1}$  and  $2.2 \pm 0.2 \text{ eV}$ . Comparison of the measured Ga desorption rate of about  $\Phi(\text{Ga}) = 6 \times 10^{13} \text{ cm}^{-2} \text{ s}^{-1}$  and the nitrogen effusion rate ( $\Phi(\text{N}) = 2 \times 10^{13} \text{ cm}^{-2} \text{ s}^{-1}$ , as discussed in section 3) from a GaN surface in vacuum at 830 °C, indicates that the maximum substrate temperature in GaN MBE processes is strongly limited by the desorption and decomposition of  $\text{N}_2$  and Ga from the growing surface.

The temperature-dependent gallium and nitrogen fluxes measured by desorption measurements allow calculation of nitrogen loss by the film during growth and determination of the maximum substrate temperature for a given applied nitrogen radical flux at the surface. The number of incident nitrogen radicals ( $\Phi_s$ ) on the film surface must exceed the number of desorbed nitrogen atoms. Figure 39 shows the maximum substrate temperature, at which the flux of desorbed nitrogen atoms equals the number of incident nitrogen radicals. Conventional radical sources are able to generate ion fluxes of  $10^{15}\text{--}10^{16} \text{ cm}^{-2} \text{ s}^{-1}$ , which lead to maximum deposition temperatures ( $T_{\text{Smax}}$ ) of 790–860 °C, 960–1040 °C and 1035–1115 °C for the growth of InN, GaN and AlN by MBE respectively.

AlN films were deposited by Davis and co-workers [211] on 6H–SiC (0001) substrates at 1050 °C by ECR-MBE. Aluminium was evaporated from a standard effusion cell at 1260 °C. Nitrogen was decomposed in the vicinity of the substrate by an ECR plasma operated at 100 W. The growth rate was  $0.1 \mu\text{m h}^{-1}$ . The Al and N adatoms were affected by a potential energy barrier at the step sites [212] caused by the differences in *c*-axis crystallography and bonding characteristics between 6H–SiC and AlN, such that surface migration was hindered. This results in a variation in thickness from the area of coalescence to the centre of the island features on the terrace sides. The majority of the nuclei on the different terrace sites fail to align with their neighbouring nuclei, due to their antiphase-like orientation. Additional studies of the step configuration indicate that some nuclei formed on different levels of the terraces can align with each other without any strain because of the step geometry of the 6H–SiC substrate. An ideal on-axis SiC surface which contains no steps should allow the nucleation and growth of nearly perfect two-dimensional

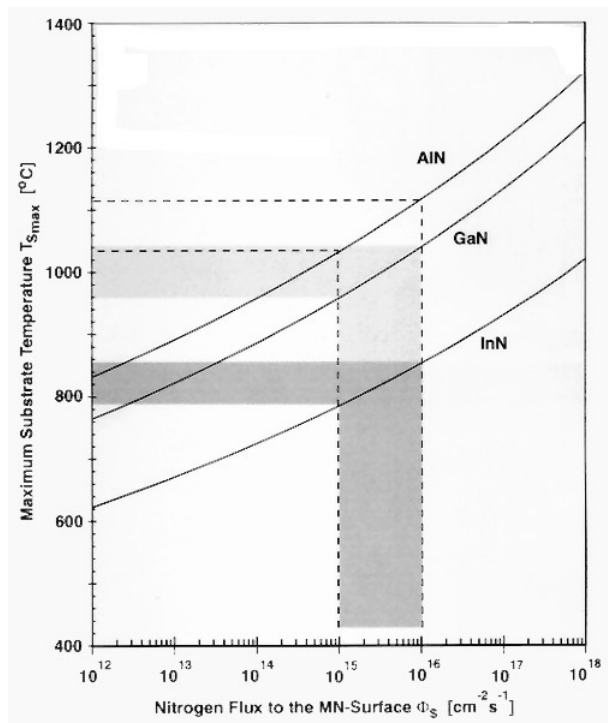


**Figure 39.** Maximum substrate temperature versus nitrogen radical flux to the surface of the growing Group III-nitride film deposited by MBE [61].

AlN film for the first several monolayers. It has been found that continued deposition of AlN films beyond a certain thickness on the on-axis substrates resulted in the onset of three-dimensional growth, but the critical thickness for the onset of this Stranski–Krastanov growth mode in the AlN/SiC system using MBE is still unknown.

GaN deposited on the AlN/SiC bilayer showed indications of low-angle grain boundaries propagating from the interface. HRTEM images along different diffraction vectors also revealed inversion domain boundaries and dislocations [213]. However, the structural and electrical properties of the GaN layer were good enough to grow p-type material without postprocess annealing. The Mg-doped GaN layer had a carrier concentration and Hall mobility of  $10^{18} \text{ cm}^{-3}$  and  $10 \text{ cm}^2 \text{ V}^{-1} \text{ s}^{-1}$  respectively. These results indirectly support the hypothesis of hydrogen-correlated passivation of Mg dopants in GaN as the cause of the difficulty in achieving highly conducting p-type materials using MOCVD or other techniques in which hydrides are used as the nitrogen source.

Lin *et al* also used AlN/SiC ( $d(\text{AlN}) = 10 \text{ nm}$ ) substrates for the deposition of 2.5–3.5  $\mu\text{m}$  thick epitaxial GaN films by ECR-MBE at  $660^\circ\text{C}$  [214]. The photoluminescence of the GaN at 6 K had a peak position at 3.47 eV and a FWHM below 5 meV. The n-type GaN had a carrier concentration of  $2 \times 10^{17} \text{ cm}^{-3}$  with a mobility of up to  $580 \text{ cm}^2 \text{ V}^{-1} \text{ s}^{-1}$  at room temperature. This is the highest mobility of electrons in GaN grown by MBE reported to date and is about half the highest reported mobility, from GaN with carrier concentrations of  $4 \times 10^{16} \text{ cm}^{-3}$  grown by MOCVD ( $\mu_e = 900 \text{ cm}^2 \text{ V}^{-1} \text{ s}^{-1}$ ) [215].

Heterojunction LEDs using rf nitrogen plasma MBE have been realized by Riechert *et al* depositing GaN/InGaN/GaN [216] and by Van Hove *et al* with AlGaIn/GaN/AlGaIn heterostructures [217]. Transistors [218] and surface acoustic wave devices [219] were realized using MBE-grown Group III-nitrides, demonstrating the usefulness of PIMBE for the fabrication of semiconductor devices.

Table 11 summarizes the discussed growth methods with representative deposition conditions and the results of XRD and Hall measurements, to enable a comparison between the different methods used to fabricate epitaxial GaN films. HVPE, MOCVD and MBE methods produce epitaxial films with the best structural and electrical properties, suitable for device applications. HVPE is especially suitable for producing thick films because of the high deposition rate. MOCVD and MBE processes have the advantage of enabling both n-type and p-type device fabrication by doping. Plasma-assisted MBE has the advantage of excellent process control, the absence of hydrogen transport gas and a relatively low growth temperature, which is extremely important for the growth of In-containing alloys with high indium concentrations. MOCVD, especially in combination with the lateral overgrowth technique, produces GaN films of the highest reported quality to date. The dislocation density can be reduced to  $10^8 \text{ cm}^{-2}$ , the electron concentration to  $10^{16} \text{ cm}^{-3}$  and the surface roughness to bilayer steps ( $\text{rms} \approx 0.2 \text{ nm}$ ) over large areas. This is one explanation why most of the Group III-nitride devices discussed below are fabricated by MOCVD. But, although MBE and MOCVD processes are very successful in producing alloys, doped GaN, and complicated heterostructures, there is still controversy about the role of impurities as the origin of the n-type background electron concentration and how to realize efficient doping of Group III-nitride alloys in the future.

## 5. Impurities and dopants

A basic understanding of which elements might act as impurities in Group III-nitrides is important for the growth of films and crystals with optimized optoelectronic properties. Atoms with tetrahedral radii close to those of M ( $M = \text{Al, Ga or In}$ ) and N would be most apt to substitute for these. Values for such radii can be taken from Holleman and Wiberg [220]. Considering only those impurities which would be isoelectronic or act as single donors or acceptors, the criterion of comparable ionic radius (a difference in radii below 10%) indicates that C, O, Ti and Ge should have a high, and Si, In, Zn and Mg should have a moderate to low solubility in the Al and Ga sublattice. The ionic radius of In ( $\approx 1 \text{ \AA}$ ) is larger than those of Ga and Al ( $\approx 0.65 \text{ \AA}$ ), and therefore the solubility of O and C should be smaller. The solubility of Sc, Ti, Cd and Ca should be high and that of Zn, Mg, and Si, moderate in the In sublattice.

A second criterion that should be applied is the stability of the impurity bonds at the growth temperatures used. This means that for C or O to be substitutional impurities, the compounds  $\text{M}_4\text{C}_3$  or  $\text{M}_2\text{O}_3$  should be stable at the growth



**Table 11.** Comparison of growth parameters, structural and electrical properties of GaN films grown by deposition methods discussed in section 4.

Growth method and literature reference	Substrate	Pretreatment	Nucleation layer	Substrate temperature (°C)	Thickness (μm)	Deposition rate (μm h <sup>-1</sup> )
HVPE [98]	c-Al <sub>2</sub> O <sub>3</sub>	GaCl	ZnO	1050	74	15
SSM [104]	6H-SiC	Nitridation	—	1200	70–100	200–1100
Sputtering [119]	c-Al <sub>2</sub> O <sub>3</sub>	Thermal annealing	—	500	1	0.2–0.5
SSD [120–122]	—	—	—	1250–1550	200–400	<100
TFMOCVD [215]	c-Al <sub>2</sub> O <sub>3</sub>	1050 °C H <sub>2</sub>	GaN 510 °C 20 nm	1035	4	4
APMOCVD [169, 177]	c-Al <sub>2</sub> O <sub>3</sub>	Nitridation	AlN 600 °C 20 nm	1080	1.2	2.4
LEO/MOCVD [186]	c-Al <sub>2</sub> O <sub>3</sub>	Nitridation	—	800	3	0.5–1.0
PIMBE [206]	c-Al <sub>2</sub> O <sub>3</sub>	Thermal annealing	—	800	3	0.5–1.0

Growth method and literature reference	ω-scan FWHM 0002 (arcmin)	Dislocation density (cm <sup>-2</sup> )	Free carrier concentration (cm <sup>-3</sup> )	Mobility (cm <sup>2</sup> V <sup>-1</sup> s <sup>-1</sup> )
HVPE [98]	5.0	3 × 10 <sup>8</sup>	7 × 10 <sup>16</sup>	845
SSM [104]	4.5			
Sputtering [119]	60		1.2 × 10 <sup>19</sup>	9
SSD [120–122]	0.5	<10 <sup>6</sup>	10 <sup>19</sup>	90
TFMOCVD [215]	4		3 × 10 <sup>16</sup>	900
APMOCVD [169, 177]	4.5	4 × 10 <sup>8</sup>	10 <sup>17</sup>	600
LEO/MOCVD [186]		<10 <sup>7</sup>	2 × 10 <sup>17</sup>	644
PIMBE [206]	5	10 <sup>9</sup>	8 × 10 <sup>16</sup>	580

temperature. The compound Al<sub>2</sub>O<sub>3</sub> melts congruently at 2051 °C [221]; Al<sub>4</sub>C<sub>3</sub> decomposes peritectically at 2135 °C [222]. Thus both C and O can be expected to act as highly soluble impurities in AlN by substituting for N. Of the possible nitrogen compounds, Mg<sub>3</sub>N<sub>2</sub>, SiN<sub>4</sub> and BeN<sub>2</sub> exist at 1000 °C [223–225], indicating a relatively high solubility of Mg, Si and Be at high temperatures. Thus Mg, Si and Be should be considered as possible substitutes for Al for fabrication of n- and p-type material. It should be pointed out that the existence of Mg<sub>3</sub>N<sub>2</sub>, SiN<sub>4</sub> and BeN<sub>2</sub> is a sign of high solubility of the dopants (Mg, Si and Be), but the formation of such compounds during growth will limit the efficiency of doping.

Oxygen is a well known impurity in AlN. It can be present in high concentrations, up to  $1.5 \times 10^{22} \text{ cm}^{-3}$  [226], and its incorporation has a drastic influence on the structural properties of AlN. Different sites for O in GaN were calculated by Neugebauer and Van de Walle [227] and Mattila and Nieminen [228]. For oxygen on the Ga site, the atomic geometry is similar to the nitrogen anti-site; oxygen moves towards the inequivalent nitrogen neighbour and forms a strong N–O bond. Within the physically allowed range of chemical potentials and Fermi energies, oxygen on a nitrogen site is the energetically preferred configuration. Substituting nitrogen with oxygen causes small elastic strain around the defect, because the O–Ga bond length is only 0.5% larger than the bulk Ga–N bond. Oxygen on a N site has one electron level close to the conduction band which is singly occupied in the neutral charge state. Oxygen therefore acts as a single donor.

For substitution in the Al sublattice, work by Tiede *et al* [229] indicated that up to 5 wt% Si can be put into AlN at 800 °C and a nitrogen partial pressure of 2 bar. More recent work by Kamyshev *et al* [230] indicates a maximum solubility of 0.12 wt% Si or  $8.8 \times 10^{19} \text{ cm}^{-3}$  Si atoms. The addition of Si is reported to make AlN n-type [231], which is the behaviour that would be expected if Si replaces Al. For a Si impurity in GaN, theoretical calculations find [227] that the nitrogen substitutional site and the interstitial configurations are energetically unfavourable. Si in the Ga sublattice is an energetically very stable configuration. It is interesting to note that maximum solubility is not reached under N-rich growth conditions, because such conditions promote the formation of Si<sub>3</sub>N<sub>4</sub>.

The electronic properties of Si donors in heteroepitaxial layers of GaN were investigated by Götz and co-workers [232]. The n-type layers were grown by MOCVD and intentionally doped with Si up to concentration of  $2 \times 10^{19} \text{ cm}^{-3}$ . By increasing the Si concentration in GaN from  $5 \times 10^{17}$  to  $2 \times 10^{19} \text{ cm}^{-3}$ , the concentration of free electrons was increased from  $2 \times 10^{17}$  to  $1.5 \times 10^{19} \text{ cm}^{-3}$ , whereas the mobility of the carriers decreased from 500 to  $135 \text{ cm}^2 \text{ V}^{-1} \text{ s}^{-1}$  at room temperature. The ratio between the concentration of incorporated Si atoms and free electrons was in the range of  $2.0 \pm 0.5$ . The n-type conductivity was found to be dominated by a Si donor with an activation energy between 12 and 17 meV. (A deeper donor level with an activation energy of 34 meV was also present in the GaN samples, and is tentatively assigned to oxygen donors substituting for nitrogen.)

The role of carbon in GaN is controversial. Carbon on a Ga site exhibits a different atomic structure than expected from the chemically similar defect structures such as N or O on a Ga site. Whereas N and O on a Ga site prefer an asymmetric configuration with only one bond to a nitrogen atom, C remains on the substitutional site and forms four nearly symmetric bonds to its neighbours. C on a N site is a shallow acceptor and can be easily incorporated into n-type GaN during growth and partially compensates the n-type conductivity. Hole concentrations up to  $3 \times 10^{17} \text{ cm}^{-3}$  were achieved by Abernathy *et al* in GaN doped with C from a  $\text{CCl}_4$  source, during metalorganic ECR-MBE at  $700^\circ\text{C}$ . The hole mobility was determined to be  $100 \text{ cm}^2 \text{ V}^{-1} \text{ s}^{-1}$  at 300 K [233]. The solubility of carbon or carbon-oxygen complexes in AlN is sufficient to produce p-type crystals of low electrical resistivity [234]. The crystal structure of  $\text{Al}_2\text{CO}$  is the same as that of AlN and solubilities up to 14%  $\text{Al}_2\text{CO}$  in  $\text{Al}_2\text{N}_2$  have been measured [235].

Hydrogen is an impurity in many semiconductors which exhibits very complex behaviour because of its high diffusivity and chemical reactivity. The ability of atomic hydrogen to passivate or compensate both shallow and deep defects and to induce extended defects has a large influence on the mechanical and optoelectronic properties in semiconductor materials [236]. MOCVD-grown GaN is commonly n-type conductive; p-type conductivity has been more difficult to obtain. It was first shown by Amano *et al* [237] that p-type conductivity can be achieved by activating Mg-doped GaN using low-energy electron irradiation. Nakamura *et al* [238], Brandt *et al* [239] and Johnson and Götz [240] demonstrated that the activation of Mg acceptors can also be achieved by thermal annealing in the temperature range of 600 to  $775^\circ\text{C}$ , and that the annealing step is reversible by hydrogenation using a hydrogen plasma at film temperatures above  $500^\circ\text{C}$ . Based on these observations, it was suggested that hydrogen plays a crucial role in passivating the Mg acceptors. For this reason Neugebauer and Van de Walle theoretically investigated Mg-H complexes [241] and concluded that hydrogen does not form a bond to the Mg atom, but prefers the antibonding site of one of the nitrogen neighbours. Thus, the Mg-H complex has a modified H-N bond as its main feature, and the dissociation barrier was estimated to be 1.5 eV. As mentioned above, MBE-grown GaN doped with magnesium is p-type without a thermal activation process, because of the absence of hydrogen and nitrogen-hydrogen radicals during growth. At room temperature, Mg-doped GaN grown by MBE or MOCVD (thermally activated) has free hole concentrations above  $10^{18} \text{ cm}^{-3}$  with mobilities in the range of  $10 \text{ cm}^2 \text{ V}^{-1} \text{ s}^{-1}$ , allowing the realization of p-n junctions [242, 243]. The binding energy of the Mg acceptor, as determined from donor-acceptor (D-A) pair transitions in luminescence, is 250 meV [10]. Temperature-dependent photoluminescence experiments gave thermal ionization activation energies between 155 and 165 meV for the Mg acceptor [244]. The relatively high thermal ionization activation energy is the reason why  $10^{20} \text{ cm}^{-3}$  Mg atoms have to be incorporated in order to yield hole concentrations above  $10^{18} \text{ cm}^{-3}$  (figure 40).

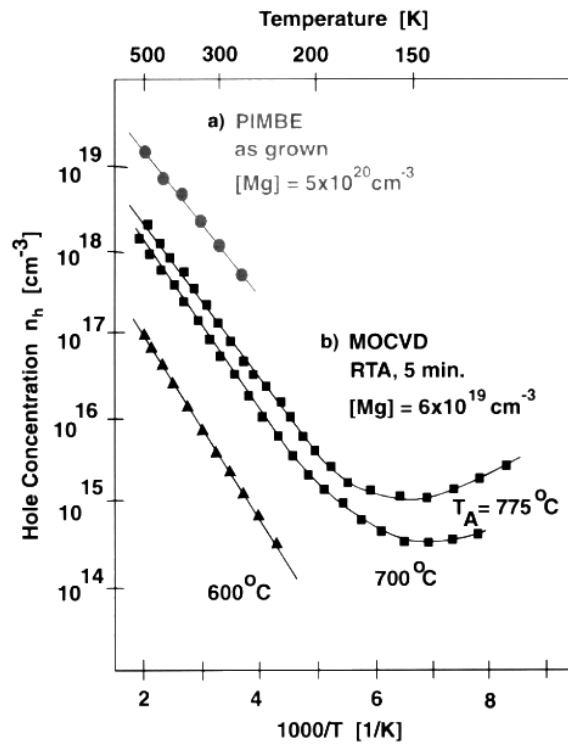


**Figure 40.** Hole concentration versus reciprocal temperature for Mg-doped GaN: (a) produced by PIMBE and (b) grown by low-pressure MOCVD and thermally activated at different temperatures [240].

There is still the question of whether acceptors with smaller binding energies exist, and whether they are suitable dopants that can be incorporated at high concentrations. Zn, Cd, and Be also belong to the Group II elements, like Mg, and can substitute for Ga in GaN. From transient luminescent spectra and time resolved luminescence for Zn:GaN and Cd:GaN, conclusions about the identity of the active recombination centres were drawn by Bergman and co-workers [245]. The dominating centres created by moderate Zn and Cd doping in GaN were identified as the substitutional acceptors,  $\text{Zn}_{\text{Ga}}$  and  $\text{Cd}_{\text{Ga}}$ , with binding energies of 0.34 and 0.55 eV. Those results indicate that the acceptor levels caused by Zn and Cd incorporation in GaN are even deeper than the Mg acceptor level and therefore less efficient in creating free holes at room temperature. Neugebauer and Van de Walle [246] carried out a comprehensive investigation of acceptor impurities in GaN, based on first principles total energy calculations. None of the candidates (Li, Na, K, Be, Zn and Ca) exhibited characteristics which are better than Mg. Only Be emerged as a potential alternative dopant, though it may suffer from more limited solubility and from compensation by Be interstitial donors [246].

Brandt *et al* reported p-type room-temperature conductivities as high as  $50 (\Omega \text{ cm})^{-1}$ , achieved in cubic GaN layers by reactive co-doping [247]. The GaN films were synthesized by MBE on semi-insulating GaAs. p-Type doping was initiated by co-doping with Be evaporated from an effusion cell and oxygen originating from  $\text{H}_2\text{O}$  in the background pressure. At a growth rate of

**Table 12.** Compilation of the acceptor binding energies for C, Mg, Be, Zn and Cd in various III–V semiconductors [255].

Binding energy (meV)	GaAs	InP	GaP	GaN
C	27	41.3	54	230
Be	28	41	55	250
Mg	28.8	48	59.9	250
Zn	30.7	46.4	69.7	340
Cd	34.4	57	102.2	550

0.1 ML  $s^{-1}$  at a temperature of 650 °C, a concentration of  $5 \times 10^{20} \text{ cm}^{-3}$  Be and O atoms was incorporated into the GaN film. Hall measurements yielded p-type conductivity with a hole concentration of  $10^{18} \text{ cm}^{-3}$  and a hole mobility of  $150 \text{ cm}^2 \text{ V}^{-1} \text{ s}^{-1}$ . Zolper *et al* achieved p-type doping in GaN by co-implanting Ca with P at concentrations of  $10^{19} \text{ cm}^{-3}$  and subsequently annealing the sample to 1100 °C for p-type conversion [248]. The measured activation energy of holes was 169 meV for Ca and 171 meV for Mg. The hole mobility measured by Hall experiments was determined to be  $7 \text{ cm}^2 \text{ V}^{-1} \text{ s}^{-1}$ , showing that Ca can be used as a p-dopant. For comparison, possible acceptors with activation energies and representative results of achieved carrier concentrations are summarized in table 12.

To date, Mg and Si are also the most important acceptors and donors for Group III-nitride alloys. The possibility for n-type doping of  $\text{Al}_x\text{Ga}_{1-x}\text{N}$  with Si is demonstrated for the whole range of composition, although the activation energy of the Si donor increases from 27 meV to about 320 meV by changing from GaN to AlN. p-Type doping of AlGaIn with Mg is realized for  $x < 0.27$ , but the hole concentration drops exponentially with increasing Al concentration, due to the increasing activation energy of the Mg acceptor from 160 meV ( $x = 0$ ) to about 360 meV ( $x = 0.27$ ) [249–252]. Si and Mg were also used for doping InGaIn alloys [253] and p-type conduction in InGaIn ( $x = 0.09$ ) doped with Mg ( $2 \times 10^{20} \text{ cm}^{-3}$ ) has been achieved with a hole concentration, mobility and activation energy of  $7 \times 10^{17} \text{ cm}^{-3}$ ,  $2 \text{ cm}^2 \text{ V}^{-1} \text{ s}^{-1}$  (at 300 K) and 204 meV [254] respectively. Although GaN and AlN can be doped both n- and p-type, some interesting applications are limited by the resistivity of p-doped films. The fabrication of low resistance p-contacts (section 8), UV surface-emitting laser structures and the achievement of low turn-on voltages in LEDs and lasers are partially limited by the hole mobility and concentration.

## 6. Band offsets

Knowledge of band discontinuities between nitride materials in heterojunctions is important for assessing the degree of carrier confinement and for designing electronic and optoelectronic devices. Martin *et al* measured the valence band discontinuity  $\Delta E_V$  of  $\text{M}_1\text{N}/\text{M}_2\text{N}$  ( $\text{M}_1, \text{M}_2 = \text{In, Ga and Al}$ ) (0001) heterojunctions by XPS [256, 257]. The samples investigated were of wurtzite crystal structure and were grown on 6H-SiC and  $\text{Al}_2\text{O}_3$  substrates by ECR-MBE. The method first measures the core-level binding

energies with respect to the valence band maximum ( $E_V - E_{CL}$ ) in the bulk films. Then for each heterojunction, the energy difference between two characteristic core levels  $\Delta E_{CL}$  was measured and the valence band discontinuity was calculated by  $\Delta E_V = (E_V - E_{CL})_{\text{MIN}} - (E_V - E_{CL})_{\text{M2N}} + (\Delta E_{CL})_{\text{MIN-M2N}}$ . Six heterojunctions were grown and measured, containing InN, GaN and AlN, and both growth sequences. The heterojunctions InN/GaN and InN/AlN showed a significant asymmetry in  $\Delta E_V$  of 0.34–0.39 eV by reversing the interface order. This asymmetry was explained as a result of strain-induced piezoelectric fields. The values for the band offsets, after applying corrections reported by Martin *et al* for the strain-induced piezoelectric fields, are listed in table 13. (The possible influence of spontaneous polarization on the band offsets was not taken into account.) For GaN/InN and AlN/InN, the measured offset values of 1.05 eV and 1.81 eV are considerably larger than the corresponding values in other III–V systems:  $\Delta E_V(\text{GaX/InX}) \approx 0.1 \text{ eV}$  and  $\Delta E_V(\text{AlX/InX}) \approx 0.6 \text{ eV}$  for  $X = \text{P, As, and Sb}$  [258].

Waldrop and Grant also used XPS in a similar way to determine the valence band offset at an AlN/GaN (0001) heterojunction [259]. GaN and AlN epitaxial films of thickness 200 Å and 50 Å respectively were grown on an n-type Si-face (0001) 6H-SiC wafer by MBE, using  $\text{NH}_3$  and a substrate temperature of 625–650 °C. A valence band offset of  $\Delta E_V = 1.36 \pm 0.07 \text{ eV}$ , corresponding to  $\Delta E_C/\Delta E_V = 52/48$ , was determined. This value agrees with an estimate based on superlattice cathodoluminescence [260], but is in substantial disagreement with the XPS measurements by Martin *et al*,  $0.8 \pm 0.3 \text{ eV}$ . By photoluminescence excitation spectroscopy, the acceptor level of iron in polycrystalline AlN could be located at  $E_V + 3.0 \text{ eV}$ . The corresponding value for iron in GaN is  $E_V + 2.5 \text{ eV}$ . From these values, the valence band offset in AlN/GaN heterojunctions was predicted by Baur *et al* to be  $\Delta E_V = 0.5 \text{ eV}$ , and the conduction band offset 2.3 eV [261]. The experimental results obtained by different groups and methods for the interface between GaN and AlN are thus scattered between 0.5 and 1.36 eV.

There is also a significant disparity between the XPS results of Waldrop and Grant and recent calculations. A self-consistent calculation [262] of the zincblende AlN/GaN (110) interface gave  $\Delta E_V = 0.85 \text{ eV}$  and a conduction band offset of  $\Delta E_C = 0.81 \text{ eV}$  between the  $X_1$  minimum of AlN and the  $\Gamma_1$  minimum of GaN. Hydrostatic strain effects due to lattice mismatch were estimated to be less than 0.2 eV. Albanesi *et al* [262] also calculated the valence band offsets at the zinc blende GaN/InN and InN/AlN (110) interface and for all wurtzite binary heterostructures, using a linear muffin-tin orbital method with up to  $5 + 5$  supercells. Common lattice constants of 4.435 Å for GaN/AlN, 4.670 Å for AlN/InN and 4.735 Å for InN/GaN were used. The results listed in table 13 are identical for the zincblende and wurtzite structures, and for all heterostructures the conduction band offset is always higher than the valence band offset. Wei and Zunger used a first principle, general potential, linearized augmented plane wave (LAPW) method to study crystal field and

**Table 13.** Valence band ( $\Delta E_V$ ) and conduction band offsets ( $\Delta E_C$ ) in cubic (in eV) (c) or hexagonal (h) Group III-nitride heterojunctions.

		InN/GaN		GaN/AlN		InN/AlN	
		c	h	c	h	c	h
Albanesi <i>et al</i> [262]	$\Delta E_V$	0.51	0.51	0.85	0.85	1.09	1.09
Wei and Zunger [263]	$\Delta E_V$	0.26	0.48	0.84	0.81	1.04	1.25
Martin <i>et al</i> [256, 257]	$\Delta E_V$	—	1.05	—	0.7	—	1.81
Baur <i>et al</i> [261]	$\Delta E_V$	—	—	—	0.5	—	—
Waldrop and Grant [259]	$\Delta E_V$	—	—	—	1.36	—	—
Albanesi <i>et al</i> [262]	$\Delta E_C$	1.07	1.09	0.81	1.78	2.15	3.14
Martin <i>et al</i> [256, 257]	$\Delta E_C$	—	0.45	—	2.1	—	2.72
Baur <i>et al</i> [261]	$\Delta E_C$	—	—	—	2.3	—	—
Waldrop and Grant [259]	$\Delta E_C$	—	—	—	1.47	—	—

spin orbit parameters, as well as the unstrained band offsets at the interfaces of cubic and hexagonal Group III-nitrides [263]. The calculated valence band offsets for the lattice-mismatched GaN/InN and AlN/InN interfaces in the wurtzite structure are larger than in the zincblende structure. The difference in zincblende versus wurtzite valence band offset of both interfaces is explained by the strain relaxation at the interface. Therefore in the nearly lattice-matched AlN/GaN system, the wurtzite and zincblende structures have similar offsets.

Murayama and Nakayama calculated the band structure of various semiconductors in both wurtzite (WZ) and zincblende (ZB) structures, using the first principle pseudopotential method within the local density approximation, and then the band offsets at interfaces (111)ZB and (0001)WZ were evaluated for the band edge states around the fundamental gaps. For GaN and AlN, the band offsets between the states at the  $\Gamma_L^{ZB}$  point in cubic material and those at the  $\Gamma^{WZ}$  point in hexagonal material were calculated to be 0.034 and 0.056 eV respectively [264]. The approximate band offsets for wurtzite and zincblende Group III-nitrides and selected substrate materials are shown in figure 41.

The theoretical investigations do not agree with the core level measurements of Waldrop and Grant who found a much larger value of  $\Delta E_V(\text{AlN/GaN}) = 1.36$  eV. Furthermore, the calculated values of  $\Delta E_V(\text{GaN/InN})$  and  $\Delta E_V(\text{AlN/InN})$  are considerably smaller than the recently measured values. Comparing all experimental and calculated results of the valence band offsets of wurtzite Group III-nitride interfaces, we find values of 0.48–1.05 eV, 1.09–1.81 eV and 0.5–1.36 eV for  $\Delta E_V(\text{GaN/InN})$ ,  $\Delta E_V(\text{AlN/InN})$  and  $\Delta E_V(\text{AlN/GaN})$  respectively, showing the necessity for further experiments to determine band offsets with higher accuracy. In particular, the influence of spontaneous and piezoelectric polarization, in pseudomorphically grown and therefore strained heterostructures, on the experimentally determined band offsets has to be clarified in much more detail.

## 7. Etching and patterning of Group III-nitrides

The development of effective low-damage etching techniques for Group III-nitride based device fabrication re-

mains an important field of research. The chemical stability of the nitrides has resulted in very low etch rates with conventional wet etchants (of the order of several  $10 \text{ \AA min}^{-1}$ ) [265]. While a number of dry etching methods (discussed in detail later on) have been shown to be very effective for etching GaN, a number of device etching applications, such as gate recessing for field effect transistors, can be particularly susceptible to ion-induced damage. To minimize the deleterious effects of energetic ions during dry etching, it will be necessary to develop dry etch processes that utilize ion energies well below 100 eV [266]. In addition to these dry etching methods, it is important to explore alternative wet chemical etching techniques due to their simplicity and minimal introduction of surface damage.

Very recently, a number of researchers have demonstrated photo-enhanced wet etching processes that produce etch rates for GaN as high as  $400 \text{ nm min}^{-1}$  at room temperature [267–269]. When illuminated with UV light, an oxide layer of  $\text{Ga}_2\text{O}_3$  is first formed on GaN by reaction with free water molecules. During that process, the UV-excited hot carriers at the GaN/electrolyte interface have excess energy to access the  $\text{H}^+/\text{H}_2$  and  $\text{OH}^-/\text{O}_2$  redox levels in the water and to enhance the oxidation process [270]. The oxide layer is subsequently dissolved in bases or acids of suitable pH concentrations. Youtsey *et al* [266] etched GaN surfaces using a KOH solution and Hg arc lamp illumination. AFM measurements indicated a rms surface roughness of 1.5 nm, which is only slightly higher than the rms roughness of the unaffected surface (0.3 nm). Etch rates of  $50 \text{ nm min}^{-1}$  were obtained using solution concentrations of 0.02 M and an illumination intensity of  $40 \text{ mW cm}^{-2}$ . The extremely low surface roughness reported represents a major improvement over previously reported photo-enhanced wet etching results which could lead to wider applications.

Several dry etch techniques have been successfully applied for device applications. For example, fabrication of laser facets is especially dependent upon dry etching since the majority of epitaxial films are grown on sapphire substrates, which inhibits cleaving as a means of producing facets with reasonable quality.

GaN is not spontaneously etched in chlorine-containing gases at temperatures below at least  $200^\circ\text{C}$ , and thus energetic ions are helpful to break the strong chemical bond of Ga–N. GaN etching has been reported in reactive

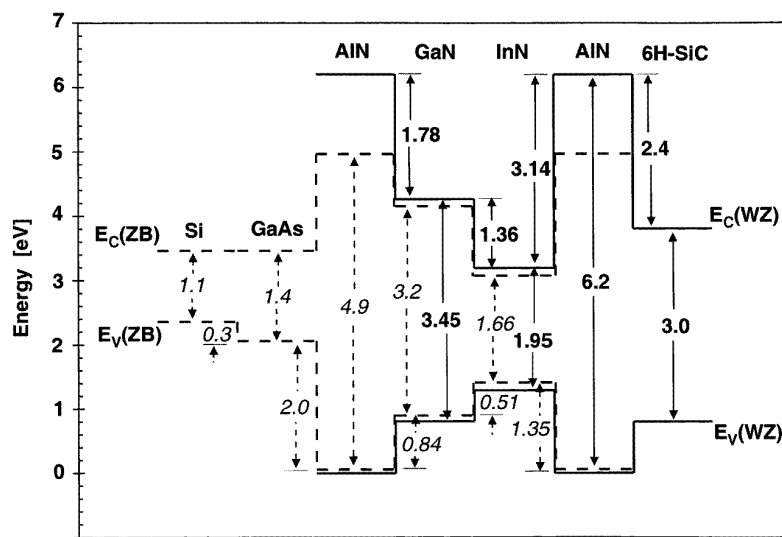


**Figure 41.** The approximate band offsets for wurtzite and zincblende Group III-nitrides and selected substrate materials at room temperature.

ion etch (RIE) systems at etch rates up to approximately  $650 \text{ Å min}^{-1}$  with DC biases of  $-400 \text{ V}$  and pressures between 20 and 80 mTorr [271–274]. GaN etch rates as high as  $3500 \text{ Å min}^{-1}$  were measured in a high-density magnetron reactive ion etch process (RIE(MIE)) at  $-100 \text{ V}$  DC bias using  $\text{BCl}_3$  [275]. Using ion beam techniques, such as chemically assisted ion beam etching (CAIBE), GaN etch rates above  $1000 \text{ Å min}^{-1}$  were obtained with a  $500 \text{ eV}$  Ar ion beam directed onto the sample in a  $\text{Cl}_2$  ambient [276, 277]. ECR etching of GaN has been reported in a variety of chlorine- and methane-based plasmas [278, 279]. Due to the magnetic confinement of electrons in the microwave source, high-density ECR plasmas operate at low pressures (1–10 mTorr) with low plasma potentials and ion energies. Under moderate DC bias conditions ( $\leq -300 \text{ V}$ ), GaN etch rates of approximately  $660 \text{ Å min}^{-1}$  in  $\text{SiCl}_4/\text{Ar}$  [280] and  $90 \text{ Å min}^{-1}$  in  $\text{BCl}_3/\text{Ar}$  [281] have been observed. Inductively coupled plasma (ICP) etch rates using a  $\text{Cl}_2/\text{H}_2/\text{Ar}$  mixture are reported to be as high as  $9800 \text{ Å min}^{-1}$  [282–284]. In the latter example, GaN was overetched by approximately 15%, with highly anisotropic, smooth sidewalls and a rms roughness between 2 and 4 nm, which allows direct application to the fabrication of laser facets. For comparison, the etch rates of MOCVD-grown GaN for the different etch methods are shown in figure 42.

The dry etching characteristics of InN and AlN epitaxial layers have been examined by Pearton *et al* [281] using  $\text{CCl}_2\text{F}_2/\text{Ar}$ ,  $\text{BCl}_3/\text{Ar}$ , and  $\text{CH}_4/\text{H}_2/\text{Ar}$  discharges. In a hybrid ECR-rf system, the Cl-based mixtures readily etch GaN and AlN, while the addition of F to the discharge dramatically reduces the etch rate of AlN. Slow, smooth etching of InN is achieved with the  $\text{CH}_4/\text{H}_2/\text{Ar}$  mixtures. Controlled rates of about  $200 \text{ Å min}^{-1}$  are obtained for all three materials at moderate DC biases ( $\leq -200 \text{ V}$ ), low pressures (1 mTorr), and low microwave power (200 W). For the Cl-based mixtures, the etch products are  $\text{InCl}_x$ ,  $\text{AlCl}_x$  and  $\text{GaCl}_x$  species for the Group III components,

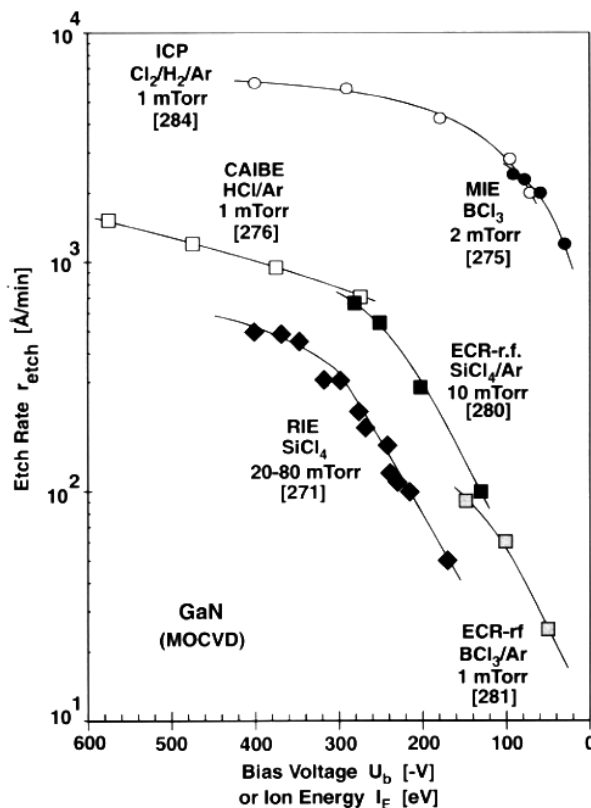


**Figure 42.** Etch rates of MOCVD-grown GaN versus bias voltage (or ion energy) for different plasma processes and gas mixtures (white circles [284], black circles [275], white squares [276], black squares [280], grey squares [281] and black diamonds [271]).

and most likely  $\text{NCl}_3$  and  $\text{CCl}_3\text{N}$  for the nitrogen. For  $\text{CH}_4/\text{H}_2/\text{Ar}$  etching, the Group III products are adducts with methyl or ethyl species, together with  $\text{NH}_3$  for the nitrogen.

**Table 14.** Plasma chemistries for dry etching of epitaxial GaN films [282, 283 and references therein].

Gas mixture	Technique [282]	GaN etch rate ( $\text{\AA min}^{-1}$ )	DC bias (V)
Ar	Ion milling	250	−400
CH <sub>4</sub> /H <sub>2</sub> /Ar	ECR	400	−250
CCl <sub>2</sub> F <sub>2</sub>	ECR	400	−250
BCl <sub>3</sub>	RIE	500	−230
SiCl <sub>4</sub> (Ar, SiF <sub>4</sub> )	RIE	500	−400
HBr (H <sub>2</sub> , Ar)	RIE	600	−400
Cl <sub>2</sub> /SF <sub>6</sub>	ECR	900	−150
HBr/H <sub>2</sub>	ECR	900	−150
Cl <sub>2</sub> /H <sub>2</sub>	ECR	1100	−150
HI/H <sub>2</sub>	ECR	1100	−150
Cl <sub>2</sub> /Ar	CAIBE	2000	−600
Cl <sub>2</sub> /H <sub>2</sub> /Ar	ECR	2200	−100
Cl <sub>2</sub> /CH <sub>4</sub> /H <sub>2</sub> /Ar	ECR	3100	−125
BCl <sub>3</sub>	MIE	3500	−75
Cl <sub>2</sub> /H <sub>2</sub> /Ar	ICP [283]	6875	−400

The selectivity for etching nitrides with respect to GaAs is high for CH<sub>4</sub>/H<sub>2</sub>/Ar discharges, but there is no selectivity with Cl-containing mixtures. If other substrates such as Al<sub>2</sub>O<sub>3</sub>, SiC, or ZnO are used, all of the discharge chemistries described here will yield selective removal of the InN, GaN, and AlN. The plasma-enhanced etch processes are summarized for comparison in table 14.

Another method for etching patterns in GaN films, reported by Kelly *et al* [285], is based on laser-induced thermal decomposition. High-energy laser pulses, with photon energies above the absorption threshold,  $E_{th} \geq 3.5$  eV, are used to locally heat the film above 900 °C, causing rapid nitrogen effusion and decomposition of the GaN. Excess gallium is then removed by conventional etching with HCl gas. At exposures of  $0.4 \text{ J cm}^{-2}$  with 355 nm light, etch rates of 50–70 nm per laser pulse (Nd:Yag third harmonic, Q-switched,  $\tau = 6$  ns) were obtained. Illumination with an interference grating was used to produce trenches as narrow as 100 nm and to rapidly produce one- or two-dimensional arrays of mesas in GaN device structures (figures 43 and 44). Other patterns could be similarly obtained by appropriate masking.

Although Group III-nitrides as wide-bandgap materials have high binding energies, etching and patterning of thin films is possible with wet chemical etching, plasma processes using chlorine mixtures, or by light-induced thermal decomposition. All processes are in principle appropriate for device process steps such as gate recessing for transistors, fabrication of patterned heterostructure optoelectronic devices, or simply for surface preparation prior to ohmic contact metallization.

## 8. Electrical contacts

The quality of Group III-nitride devices, including bright p–n junction LEDs, laser diodes, GaN metal–semiconductor field effect transistors (MESFETs), and modulation-doped field effect transistors (MODFETs), can be limited by parasitic contact resistances. Therefore, in order to attain optimum device performance, minimization of the contact resistance is necessary. Two types of interfaces are

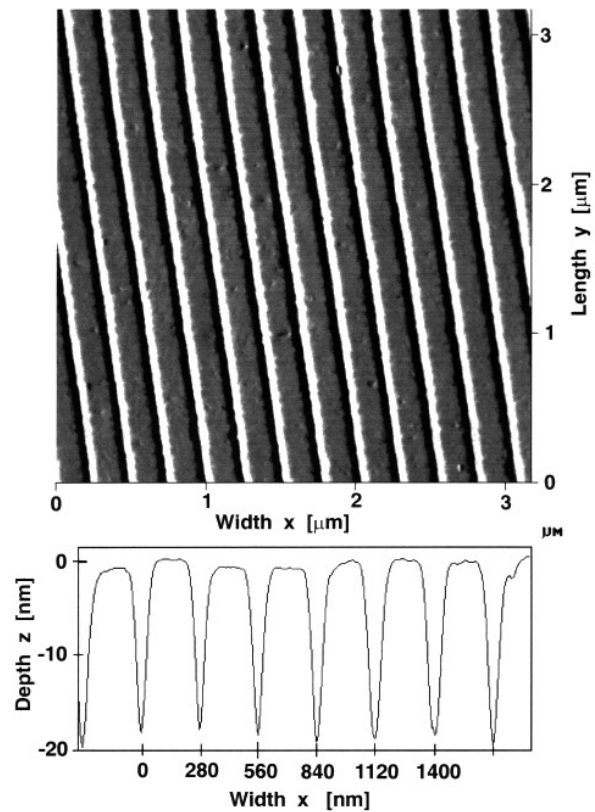


**Figure 43.** Top view and cross section of a one-dimensional array produced by laser-induced thermal decomposition of an epitaxial GaN film. An exposure of  $0.4 \text{ J cm}^{-2}$  with a single laser pulse ( $\lambda = 355$  nm,  $\Delta t = 6$  ns) with an interference grating was used to produce trenches as narrow as 100 nm. Etch rates of 20–70 nm per laser pulse were obtained [285].

associated with low-resistance ohmic contacts, low barrier Schottky contacts (using intermediate or graded bandgap interface material) and tunnelling contacts. Low-resistance ohmic contacts for wide-bandgap materials like GaN and AlN are particularly challenging, when compared to other III–V compounds like GaAs and InP. Tunnelling of carriers

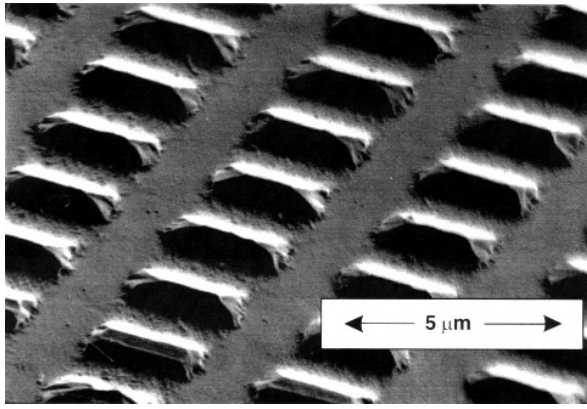


**Figure 44.** Electron micrograph of a structured GaN film, showing the bare sapphire substrate lines and GaN with sloping sidewalls. The GaN film was sequentially structured with two crossed striped interference patterns [285].

to the contact takes place only if the GaN or AlN is so heavily doped in the neighbourhood of the metal–semiconductor interface that there is a very steep band bending, forming a narrow barrier.

One of the first systematic investigations of ohmic contacts fabricated by electron beam evaporation onto n-type GaN films was carried out by Guo *et al* [286]. Si-doped epitaxial films were patterned and covered with bilayer contacts consisting of 15 nm Ti deposited directly on GaN, followed by a 150 nm Ag overlayer. Marlow and Das showed that a metal overlayer can significantly alter the effective contact resistance value [287]. When the carrier concentration of the GaN was larger than  $10^{18} \text{ cm}^{-3}$ , the contact resistance  $\rho_c$  decreased rapidly with increasing doping concentration. A specific contact resistivity of  $6.5 \times 10^{-5} \Omega \text{ cm}^2$  was obtained without thermal annealing at a very high doping concentration of  $N_D = 1.7 \times 10^{19} \text{ cm}^{-3}$  (figure 45).

Lin *et al* reported a metallization process for achieving low-resistance ohmic contacts to MBE-grown n-GaN ( $n_e \approx 10^{17} \text{ cm}^{-3}$ ) using an Al/Ti bilayer. The metals were first deposited via conventional electron beam evaporation, and then thermally annealed at between 500 and 900 °C in a  $\text{N}_2$  ambient using rapid thermal annealing techniques. The lowest value for the specific contact resistivity of  $8 \times 10^{-6} \Omega \text{ cm}^2$  was obtained with 900 °C anneals for 30 s [288]. One explanation for the good quality is the solid phase reaction between Ti and GaN, forming TiN. The annealing temperature of 900 °C is above the decomposition temperature of GaN (section 3), so nitrogen can be extracted from GaN to react with the Ti. Then an accumulation of N vacancies, which are expected to act as donors [289] would be created in the GaN near the semiconductor metal interface. This region would be heavily doped, which provides the configuration needed for tunnelling contacts. Only two monolayers of TiN have to be formed in order to generate a 10 nm layer of GaN with an electron density of  $10^{20} \text{ cm}^{-3}$ .

Fan *et al* combined the advantages of RIE and rapid thermal annealing for the fabrication of very low resistance ohmic contacts to n-GaN [291]. The metallization

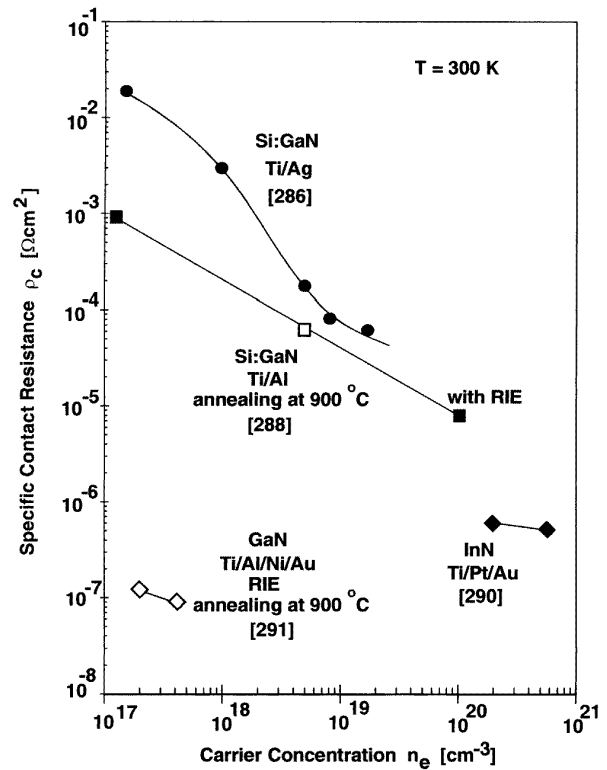


**Figure 45.** Specific contact resistance of different metallization processes for achieving low-resistance ohmic contacts to n-type GaN or InN, versus carrier concentration ( $T = 300 \text{ K}$ ) (black circles [286], black squares [288], black diamonds [290], white diamonds [291]).

technique involved the deposition of a composite metal layer Ti/Al/Ni/Au (150 Å, 2200 Å, 400 Å, 500 Å) on GaN ( $n_e \approx (1-5) \times 10^{17} \text{ cm}^{-3}$ ) preceded by RIE. There are several possible explanations for the reduction of contact resistivity by RIE. First, it provides a method to clean the surface and remove any oxide layer [292]. Second, it increases the GaN surface roughness due to the preferential etching of dislocated material, and thus increases the contact area [293]. Third, RIE causes radiation damage and increases the point defect density in a thin region near the surface. As a result, it makes diffusion of metal into GaN more rapid, even during metal deposition. With annealing at 900 °C for 30 s, contacts with specific resistivity values of  $\rho_c = 8.9 \times 10^{-8} \Omega \text{ cm}^2$  were obtained, which can be used in devices.

By including p-type GaN in devices like LEDs and laser structures, the performance characteristics of these devices, such as operating voltage, are restricted by the high contact resistance on p-type GaN. There are very limited experimental results such as Schottky barrier height and specific contact resistivity for p-type material. Mori *et al* [294] obtained the electrical properties of Pt, Ni, Au and Ti on p-type GaN by current–voltage characteristics. The corresponding contact resistivities were measured to be between 0.01 and 0.03  $\Omega \text{ cm}^2$  and therefore up to five orders of magnitude higher than for ohmic contacts on n-type GaN. The Schottky barriers for the above mentioned contacts were determined to be 0.5, 0.5, 0.57 and 0.65 eV

**Table 15.** Metal work function and electronegativity of Ti, Au, Pd, Ni and Pt and Schottky barrier height between those metals and n- or p-type GaN films determined by electrical measurements.

Contact material	Ti	Au	Pd	Ni	Pt
Metal work function $\Phi_m$ (eV) <sup>f</sup>	4.33	5.1	5.12	5.15	5.65
Metal electronegativity (eV) <sup>f</sup>	1.5	2.4	2.2	2.2	2.2
<b>n-type GaN</b>					
Barrier height $\Phi_B$ (eV)					
$I-V$	—	0.88 <sup>a</sup>	1.11 <sup>a</sup>		1.13 <sup>a</sup>
$C-V$	0.58 <sup>d</sup>	0.94 <sup>c</sup>	1.24 <sup>a</sup>		1.27 <sup>a</sup>
$I-T$	0.59 <sup>d</sup>	0.84 <sup>c</sup>	0.91 <sup>b</sup>		1.03 <sup>b</sup>
Ideality factor $n$	1.28 <sup>d</sup>	1.03 <sup>c</sup> –1.06 <sup>a</sup>	1.09 <sup>a</sup> –1.14 <sup>b</sup>		1.10 <sup>a</sup> –1.21 <sup>b</sup>
Carrier density $n_e$ (cm <sup>-3</sup> )	$3 \times 10^{17}$	$7 \times 10^{16}$	$2 \times 10^{17}$		$1 \times 10^{17}$
Breakdown voltage (–V)	—	<100 <sup>c</sup>	17 <sup>b</sup> –35 <sup>a</sup>		18 <sup>b</sup> –45 <sup>a</sup>
<b>p-type GaN<sup>e</sup></b>					
Barrier height $\Phi_B$ (eV)					
$I-V$	0.65	0.57		0.5	0.5
Ideality factor $n$	1.36	1.27		1.14	1.15
Carrier density $n_h$ (cm <sup>-3</sup> )	$5 \times 10^{17}$	$5 \times 10^{17}$		$5 \times 10^{17}$	$5 \times 10^{17}$
Specific contact resistivity ( $\Omega$ cm <sup>2</sup> )	0.035	0.026		0.015	0.013

<sup>a</sup> From [301].<sup>b</sup> From [300].<sup>c</sup> From [299].<sup>d</sup> From [292].<sup>e</sup> From [294].<sup>f</sup> From [295], [297].

respectively. Although p- and n-type Schottky barrier heights (see table 15 later) should sum approximately to the bandgap of the semiconductor, the obtained barrier heights on p- and n-type GaN are significantly less than 3.42 eV. This could result from the occupation of different interface states or the influence of strong spontaneous and piezoelectrical polarization fields as discussed earlier.

The study of Schottky barrier contacts on GaN and AlGaIn is of great importance in the application of Group III-nitrides to MESFETs and high electron mobility transistors. For the gate contact of such devices, metals which form a Schottky contact with a high barrier are needed. According to the Schottky–Mott model, the electron affinity of the semiconductor  $\chi_S$  for a Schottky barrier on an n-type semiconductor is related to the work function of the metal and the barrier height by  $\chi_S = \Phi_m - \Phi_B$  (for GaN  $\chi_S = 4.1$  eV [296]). This relationship is not so simple in practice because of charges at the junction caused by surface states, metal-induced gap states and chemical reactions at the interface.

The work functions of Pt, Ni, Pd, Au and Ti are 5.65, 5.15, 5.12, 5.1 and 4.33 eV respectively [295, 297]. Therefore those materials are expected to form good Schottky contacts for a stable ionically bonded semiconductor like GaN. Foresi and Moustakas and Hacke

*et al* reported measurements on the nature of gold contacts to GaN [298, 299]. A Schottky barrier on unintentionally doped n-type GaN ( $n_e = 6.6 \times 10^{16}$  cm<sup>-3</sup>) was obtained and characterized by Hacke *et al* using evaporated gold contacts. Good quality diodes were obtained with forward current ideality factors of 1.03 and reverse bias leakage currents below  $10^{-10}$  A at a reverse bias of –10 V. From current–voltage ( $I-V$ ) and capacitance–voltage ( $C-V$ ) test results, the barrier height  $\Phi_B$  was determined to be 0.844 and 0.94 eV respectively.

Guo *et al* deposited thin Pt and Pd layers by electron gun evaporation, to form Schottky contacts on MOCVD-grown GaN ( $n_e = 2 \times 10^{17}$  cm<sup>-3</sup>) [300]. The Schottky barrier heights with Pt were determined to be 1.04 and 1.03 eV, and with Pd to be 0.94 and 0.91 eV, by  $C-V$  and current temperature ( $I-T$ ) measurements respectively. For a diode area of  $5 \times 10^{-5}$  cm<sup>2</sup>, the breakdown voltage of Pt and Pd contacts, defined as the voltage where the leakage current exceeds  $2 \times 10^{-6}$  A, is about 18.1 and 17.5 V respectively. These results (summarized in table 15) are in good agreement with the values determined by Wang *et al* [301].

For high-power transistors and high-temperature operation of devices, thermally stable contacts are essential. Key requirements for GaN-related electrical device technology



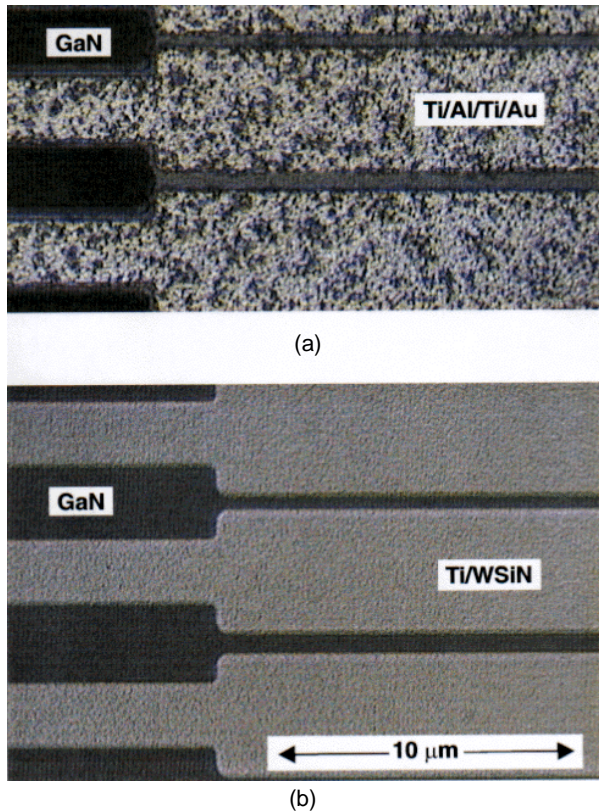


**Figure 46.** Microscope image of (a) Ti/Al/Ti/Au contact on top of GaN after annealing at 800 °C for 1 min and (b) Ti/WSiN contact after annealing at 950 °C for 1 min [304].

which are not yet solved are the achievement of acceptably low ohmic contact resistances and Schottky contacts with high thermal stability. Ti/Al-based metallizations which are commonly used for low-resistance ohmic n-contacts, show rough surfaces [302] due to the formation of complicated phase mixtures in the quaternary Ti–Al–Ga–N system, resulting in grains and voids. Pt and Pd contacts for Schottky barriers tend to change their electrical properties at high temperatures. The grain boundaries support strong diffusion between the contact material and Au-based top layers (needed for bonding) and force device degradation at high temperatures. The increasing surface roughness of contacts during thermal treatment at high temperatures limits further photolithographic processing in the sub-micron range and supports electrical breakdown and noise. Figure 46(a) shows the typical and poor morphology of a conventional Ti/Al/Ti/Au ohmic contact used as source and drain of a GaN MESFET. The size of the grains can reach several 100 nm. The ohmic contacts were annealed at 800 °C for 1 min. This represents the annealing conditions for optimum electrical performance.

Schottky diodes on n-type GaN from PtSi have been fabricated and shown to be more stable than Pt diodes. The electrical characteristics of such diodes did not change after thermal annealing at 500 °C for 1 h in air [303]. W, WSi<sub>x</sub>, WSiN and Ti/Al were all found to produce low-resistance ohmic contacts on n-type GaN, InGaN and InN. W and Ti/WSiN contacts proved to be the most stable (figure 46(b)) and remained smooth up to annealing

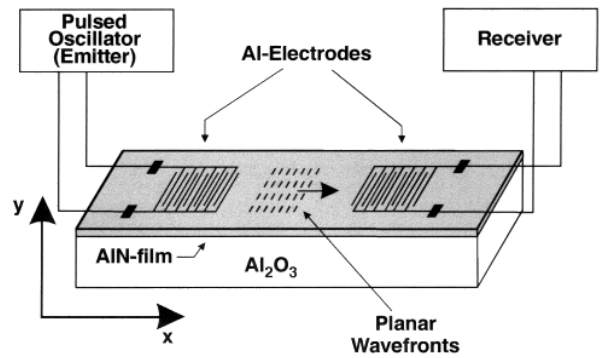


**Figure 47.** Schematic diagram of a surface acoustic wave device. An oscillator is connected to a two-finger contact (IDT) on the AlN film and is coupled piezoelectrically to a propagating surface wave. This surface wave then interacts with the second electrode, inducing an electric field. The period of the contact pattern is made equal to the surface wavelength at the desired frequency of operation.

temperatures of 800 °C for 1 h, although significant diffusion of In, N, and Al, as well as Ti and W were found after the anneal. The lowest resistances were found to be in the range between  $10^{-5}$  and  $10^{-7} \Omega \text{ cm}^2$  [304, 305]. To check whether such contact materials are sufficiently stable for high-temperature and high-power devices, transistors have to be realized and long-term annealing experiments have to be carried out.

Even with many important measurements for the characterization of contacts yet to be carried out and the quality of epitaxial films and interfaces of heterostructures needing further improvement, the Group III-nitride based devices already fabricated and discussed in the next section are surprisingly successful.

## 9. Devices

### 9.1. Surface acoustic wave devices

There is a trend towards higher frequency bands for communication systems, such as portable telephones, mobile telephones and broadcasting satellites, because of the greater bandwidths available. Many components, such as filters, duplexers and resonators, must also conform with these high frequencies. Conventionally, dielectric ceramic and surface acoustic wave (SAW) devices are used for these frequency applications. Piezoelectric SAW devices have become popular on account of their stable characteristics, lack of need for adjustment and compactness [306]. Thin film piezoelectric materials have long been utilized in the field of microwave acoustics. The earliest application of thin film piezoelectrics was in bulk wave transducers. Such materials, like preferentially oriented layers of CdS [307] and ZnO [308], with the *c*-axis parallel to the direction of wave propagation, were found adequate to efficiently generate bulk acoustic waves. Applications of SAW devices, based on LiTaO<sub>3</sub> and LiNbO<sub>3</sub> single crystals, have been developed since 1975 [309]. With this development, a need was soon recognized for thin film piezoelectric materials on insulating low-loss acoustic

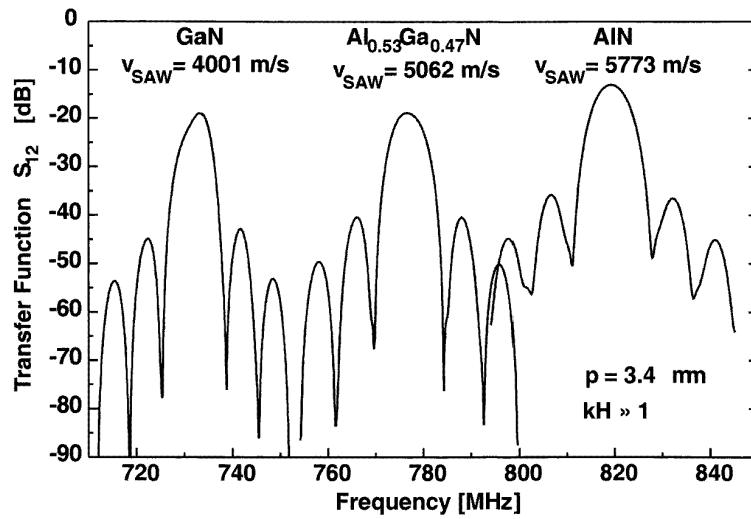


**Figure 48.** Transfer function  $S_{12}$  of SAW devices based on  $\text{Al}_x\text{Ga}_{1-x}\text{N}/\text{Al}_2\text{O}_3$  structures ( $x = 0$ ,  $x = 0.53$  and  $x = 1$ ).

materials, which can be used with microwaves of 1 to 2 GHz [310]. The characteristics required for microwave band material are: high sound velocity, very smooth surface, large electromechanical coupling factor, small transition loss and high temperature stability. Group III-nitrides, especially aluminium nitride, have been considered as an attractive thin film piezoelectric material for the fabrication of on-chip acoustic wave devices [311,312]. Epitaxial films grown by MOCVD or MBE have shown smooth surface morphology and some promising acoustic properties [22,313,314]. These include high SAW velocity (nearly twice that of quartz and  $\text{LiNbO}_3$ ), and a near-zero SAW temperature coefficient of delay.

Inside a SAW device, due to the converse piezoelectric effect, an electric rf signal applied to an interdigital transducer contact (IDT) (figure 47) produces mechanical stress in the film under the IDT. The result is a periodic mechanical displacement accompanied by an electric field, which then travels as a Rayleigh-type wave along the surface. This wave excitation works most efficiently when the acoustic wavelength  $\lambda$  equals the spatial period of the electric field in the IDT grating structure, which, in the case of an unweighted normal-finger IDT, is twice the geometrical period  $p$ . The frequency of maximum excitation (amplitude of the transfer function (figure 48)) is given by  $f_{\max} = v/\lambda = v/2p$ , where the SAW velocity  $v$  is a characteristic property of the material. When the propagating SAW reaches the receiving IDT, the piezoelectric effect generates an electrical response that can be detected. A network analyser can be used to measure the transfer function of this set-up. By using the simple arrangement of two-finger contacts and one Group III-nitride film or crystal, high-quality electrical filters can be created.

By using epitaxial AlGaN films (grown on sapphire), the propagation velocity of the SAW and the frequency  $f_{\max}$  of the transfer function can be changed by varying the Al content of the piezoelectric film. The crystal class of wurtzite  $\text{Al}_x\text{Ga}_{1-x}\text{N}$  is 6 mm which leads to isotropic

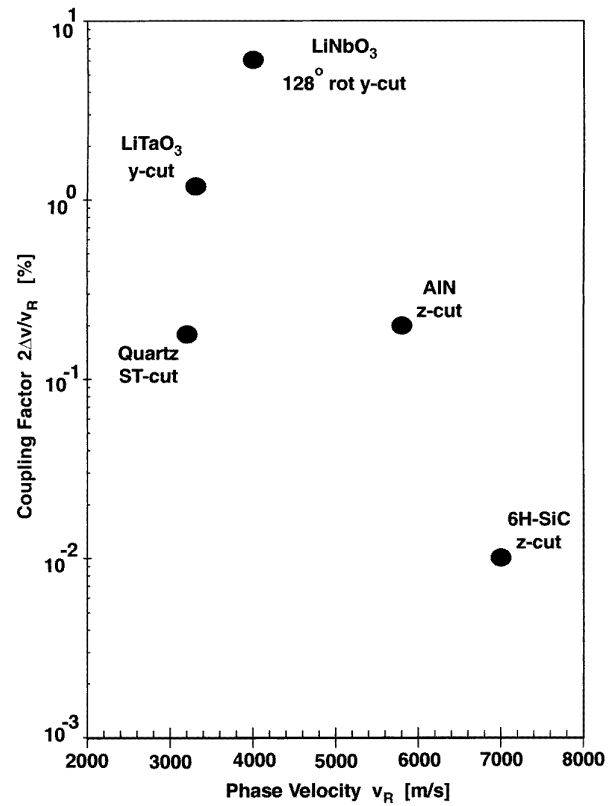


**Figure 49.** Coupling factor and phase velocity of the surface wave for different piezoelectric materials which are used for SAW devices. A high coupling factor and high phase velocity are necessary for high-frequency SAW devices. The SAW coupling coefficient is defined as  $k^2 = 2\Delta v/v_R$ , where  $\Delta v/v_R$  is the relative velocity change produced by short circuiting the surface potential from the open circuit condition.

elastic and piezoelectric properties in the  $c$ -plane, whereas the crystal class of sapphire  $3m$  results in no piezoelectricity and in a sixfold symmetry of the elastic properties in

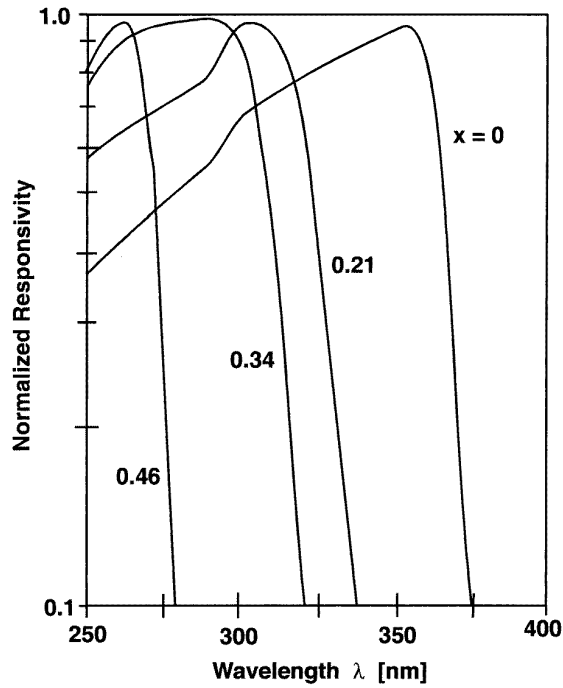


**Figure 50.** Normalized spectral responsivities for  $\text{Al}_x\text{Ga}_{1-x}\text{N}$  photoconductors,  $x$  varying from 0 to 0.46 [321].

the  $c$ -plane. In particular the computing of the SAW velocity of  $c$ -plane sapphire yields values between 5548 and 5687  $\text{m s}^{-1}$ . Experimentally, the waves propagating in the [1120] and [1100] direction of  $\text{Al}_2\text{O}_3$  were investigated because they show the smallest and largest [219] values. Figure 48 shows three transfer functions for different  $\text{Al}_x\text{Ga}_{1-x}\text{N}$  layer,  $x = 0$ ,  $x = 0.53$  and  $x = 1$ . In all cases, the IDTs had a simple finger structure with a periodicity of 3.4  $\mu\text{m}$ . By changing the alloy composition from GaN to AlN, the velocity of the SAW was changed between 4000 and 5770  $\text{m s}^{-1}$  and the frequency  $f_{\text{max}}$  was increased from 735 to 830 MHz. The electromechanical coupling coefficient  $k^2$  ( $k^2 = 2\Delta v/v_R$ ;  $v_R$ , velocity of the surface wave;  $\Delta v$ , change of the velocity caused by the piezoelectric effect) of 0.5 to 0.8% was achieved when AlN was deposited on the  $r$ -plane of  $\text{Al}_2\text{O}_3$  (figure 49) [315].

Lakin *et al* have carried out extensive studies of sputtered AlN for bulk acoustic wave resonators and filters and demonstrated, using optimized contact designs, low-loss filters operating at 1–2 GHz [316]. AlN-based SAW devices in particular have reached frequencies, electromechanical coupling factors, transition losses and high-temperature stabilities which seem to be very useful for technical applications such as cheap electrical filters, sensors (viscosity of fluids, gases) or photorefractive grids.

## 9.2. UV detectors

Detection of UV light ( $\lambda < 400 \text{ nm}$ ) has a wide range of commercial applications, including flame and heat sensors, UV calibration devices, plasma diagnostics, engine monitoring and secure intersatellite communications

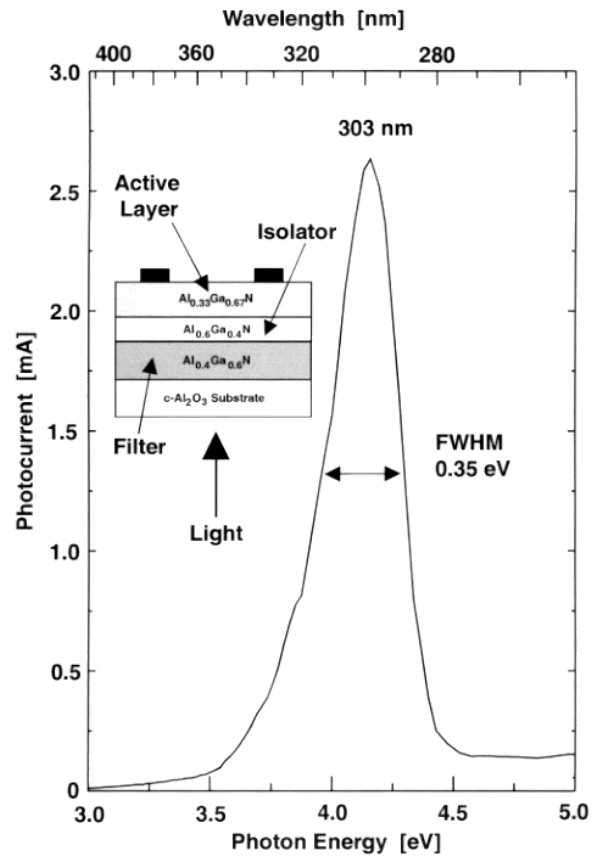


**Figure 51.** Spectrally resolved photocurrent of a self-filtered AlGaIn-based photoconductor with a sensitivity centred at 303 nm.

[317,318]. Most of these applications require a solar blind detector, one which detects only in the UV, but does not sense longer wavelength light. Traditionally, UV detection has been accomplished with a photomultiplier tube or silicon pin photodiode. The complications of a photomultiplier tube include the vacuum tube, which is physically large and fragile, the high voltages required, sensitivity to magnetic fields and high cost. Silicon diodes offer the advantages inherent in a small, solid state device, requiring only small external voltages, but are also very sensitive to infrared and visible light.

**9.2.1. Photoconductive detectors.** The next generation of UV detectors will be based on wide direct bandgap semiconductors ( $E_g > 3.0 \text{ eV}$ ). One promising material system being investigated for this application is GaN and  $\text{Al}_x\text{Ga}_{1-x}\text{N}$ . The first high-quality GaN photoconductive detectors were fabricated by Khan *et al* [319]. The active region of the detector was a 0.8  $\mu\text{m}$  thick epitaxial layer of highly resistive GaN deposited over a 100 nm thick AlN buffer layer by MOCVD. Interdigital, 500 nm thick gold contacts were fabricated on the films for the photoconductive response measurements. The spectral responsivity of GaN rises quickly at 365 nm and then remains constant down to 200 nm. The peak responsivity is about 1000  $\text{A W}^{-1}$ , and the estimated gain-quantum

efficiency product for the detectors is 4800. The response of the simple GaN detector is linear over five orders of incident radiation power, which is important for sensitive UV light measurements over a great range of intensity.

Hexagonal AlGa<sub>x</sub>N with a direct bandgap provides promising materials for UV detectors due to the relatively high mobility of carriers, the sharp cutoff wavelength, and the high quantum efficiency. By changing the Al composition, the cutoff wavelength of AlGa<sub>x</sub>N-based photodetectors can cover the spectrum from 200 to 360 nm at room temperature [320]. Figure 50 shows the spectral responsivity of Al<sub>x</sub>Ga<sub>1-x</sub>N/AlN/Al<sub>2</sub>O<sub>3</sub> photodetectors (normalized to the peak responsivity near the cutoff wavelength) [321]. The maximum current responsivity is about 1 A W<sup>-1</sup> at 360 nm under 8 V bias for the GaN photodetector. Shur and Khan [317] have also fabricated Al<sub>x</sub>Ga<sub>1-x</sub>N photoconductors with Al contents ranging from 5 to 61%. The 61% Al device exhibited a cutoff wavelength of 240 nm and photoresponsivities as high as 300 A W<sup>-1</sup>.

AlGa<sub>x</sub>N-based photoconductors with a photoresponse in a very limited spectral range can be fabricated by using an additional AlGa<sub>x</sub>N layer as an optical filter. Figure 51 shows the spectrally resolved photocurrent of an MBE-grown Al<sub>0.4</sub>Ga<sub>0.6</sub>N/Al<sub>0.6</sub>Ga<sub>0.4</sub>N/Al<sub>0.33</sub>Ga<sub>0.67</sub>N heterostructure illuminated through the sapphire substrate. Light of wavelength shorter than 285 nm travelling through the substrate is absorbed by the 400 nm thick Al<sub>0.4</sub>Ga<sub>0.6</sub>N filter layer. The photoconducting Al<sub>0.33</sub>Ga<sub>0.67</sub>N layer is separated and electrically isolated from the filter by a thin Al<sub>0.6</sub>Ga<sub>0.4</sub>N film. Using Ti/Al contacts on top of the heterostructure the photocurrent can be measured. The photoresponse has an amplitude at 303 nm (FWHM 0.35 eV) of up to 500 A W<sup>-1</sup>. The peak responsivity can be changed by an equidistant shift of the bandgaps of the AlGa<sub>x</sub>N filter, isolator and active layer.

AlGa<sub>x</sub>N-based heterostructures can be used to realize sensitive, tunable and inexpensive detectors (photoconductors) working in the near-UV spectral region. One of the critical issues being addressed is that of electrically active defects and the effect they have on the bandwidth of the photoresponse. As compared to a commercially available silicon photodiode, which can operate at frequencies of 100 kHz, Shur and Khan [317] found that AlGa<sub>x</sub>N- and GaN-based photoconductors can only operate up to 5 kHz, this speed being limited by the charge which is stored at defects in the AlGa<sub>x</sub>N material. Although photoconductive detectors have the desirable property of internal gain, they suffer from some drawbacks which can include high dark currents, DC drift and slow response time.

**9.2.2. Photodiodes.** Recently, relatively fast photovoltaic UV detection using GaN p-n and p-i-n diodes or Schottky diodes has been demonstrated [322–324]. Xu *et al* [325] investigated the spectral response of front-surface illuminated GaN and AlGa<sub>x</sub>N/GaN p-i-n UV photodetectors prepared by MBE on sapphire. The AlGa<sub>x</sub>N/GaN photodiodes (10 nm AlGa<sub>x</sub>N passivation layer, 200 nm p-GaN, 1000 nm GaN, 3000 nm n-GaN and AlN nucleation layer) had a maximum zero-bias responsivity

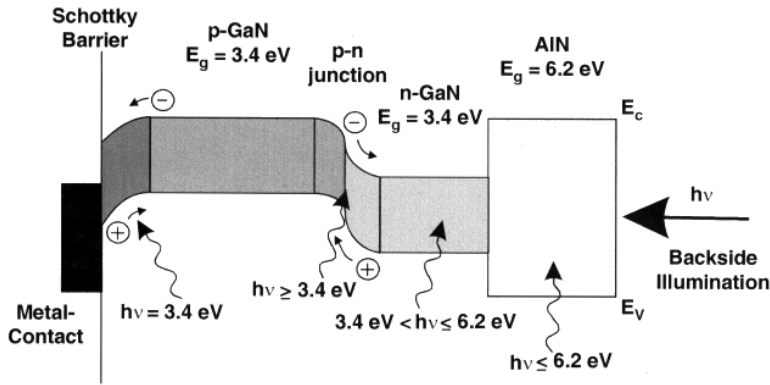
of 0.12 A W<sup>-1</sup> at 364 nm, which decreased by more than three orders of magnitude for wavelengths longer than 390 nm. The rms noise current in a 1 Hz bandwidth was about 1 pA, corresponding to a noise equivalent power of about 8 pW. Extremely fast decay times, in comparison to other Group III-nitride based photodetectors, between 12 and 29 ns were determined, which enable operation for technical applications at sufficient high frequencies.

An interesting device, a self-filtering detector which gives very sharp spectral response, was reported by Zhang *et al* [326]. This detector consists mainly of a 0.5 μm thick n-GaN layer and a 2 μm thick p-GaN layer (figure 52(a)). Utilizing backside illumination, photons with energy between 3.45 eV and 6.2 eV are then absorbed in the n-GaN layer. Because GaN has an absorption coefficient of  $2 \times 10^5 \text{ cm}^{-1}$  above the bandgap, these photons are absorbed within the first 100 nm. The diffusion length of minority carriers in GaN is much less than the thickness of the n-GaN region, so the minority carriers recombine before reaching the p-n junction depletion region, and thus produce no photocurrent. Light which has an energy very close to the bandgap of GaN can penetrate deeper into the device and reach the depletion region, forming electron-hole pairs which in turn produce photocurrent. Therefore, the responsivity of this detector is essentially tuned to the bandgap of GaN. This effect is illustrated in figure 52(b), showing the strong photoresponse at 360 nm. By adding In or Al to the GaN in this detector, it should be possible to shift this response to longer or shorter wavelengths, for blue and UV detectors which are only sensitive in a small wavelength range.

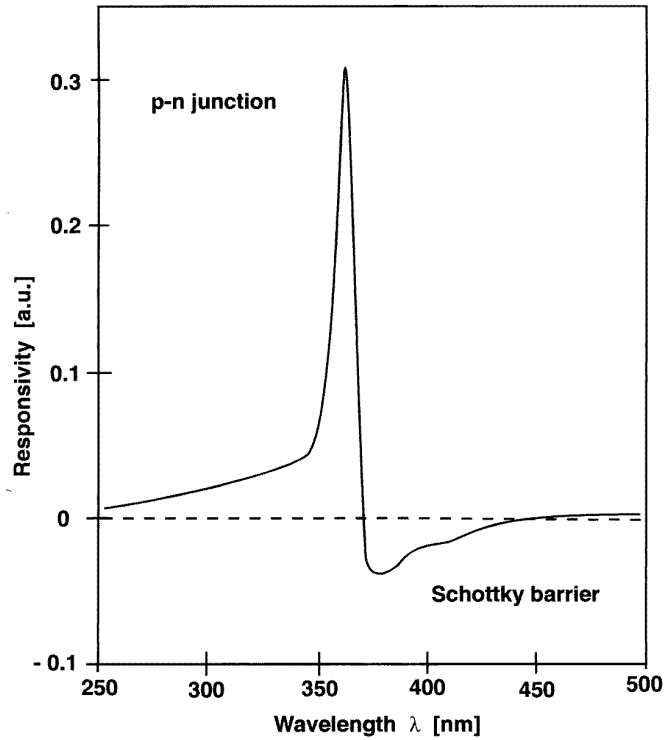
More sophisticated structures which are expected to enter the market are GaN/AlGa<sub>x</sub>N heterostructure field effect transistors (HFETs) as gated solar-blind photodetectors. Figure 53(a) shows a schematic diagram of a GaN/AlGa<sub>x</sub>N HFET. The gated photodetectors are backside illuminated. Electron-hole pairs are generated in the semi-insulating i-GaN layer and in the active n-GaN. The photogenerated holes move towards the i-GaN/sapphire interface, and the photogenerated electrons move towards the transistor channel where they are quickly driven into the drain by the high channel field. The measured and calculated maximum responsivity of 3000 W A<sup>-1</sup> for a HFET photodetector was achieved at a gate voltage of about 1 V [327]. Detectors with such a high sensitivity and responsivity can be used as flame and gas sensors.

### 9.3. Transistors

High electron mobility transistors (HEMTs) are the most mature of a new generation of Group III-nitride transistors which rely on the use of heterojunctions for their operation. The heterojunctions in these devices are formed between semiconductors of different compositions and bandgaps. This is in contrast to conventional Si and GaAs-based field effect (MESFET) and bipolar devices which utilize junctions between like materials, e.g. n- and p-type Si in a bipolar transistor. These novel devices offer potential advantages in microwave, millimetre wave and high-speed digital integrated circuit (IC) applications



(a)



(b)

**Figure 52.** (a) Energy band diagram of a p/n GaN photodiode. (b) Spectral responsivity of the GaN-based UV detector [326].

over the homojunction devices presently in use. With heterojunctions, device designers can vary the band structure (and hence the electric field) as well as the doping level and type in specific parts of the device. Significant improvements in charge transport properties are possible through innovative use of this additional degree of freedom.

As a candidate especially for future microwave power devices, AlGaIn/GaN-based field effect transistors have attracted increasing interest [12]. Besides the advantage of tunable high conduction band offsets in the AlGaIn/GaN system, theoretical simulations have predicted a high peak electron velocity of  $2.7 \times 10^5 \text{ m s}^{-1}$  and a high saturation velocity of  $1.5 \times 10^5 \text{ m s}^{-1}$  at electric fields of about  $150 \text{ kV cm}^{-1}$  (figure 53(b)). A mobility of  $\mu_e \approx 2000 \text{ cm}^2 \text{ V}^{-1} \text{ s}^{-1}$  has been calculated for electrons in the GaN channel at room temperature, at a carrier concentration of  $10^{17} \text{ cm}^{-3}$  [328–332].

Gaska *et al* [333] investigated two-dimensional electron transport in doped AlGaIn/GaN heterostructures. The highest measured Hall mobility at room temperature was  $2019 \text{ cm}^2 \text{ V}^{-1} \text{ s}^{-1}$  and increased approximately fivefold to  $10250 \text{ cm}^2 \text{ V}^{-1} \text{ s}^{-1}$  below 10 K. The measured room-temperature mobility of the two-dimensional electron gas in GaN is much larger than for comparably doped silicon ( $\approx 500 \text{ cm}^2 \text{ V}^{-1} \text{ s}^{-1}$ ) and about half of that for comparably doped GaAs ( $\approx 4000 \text{ cm}^2 \text{ V}^{-1} \text{ s}^{-1}$ ) [334]. The values for electron mobility are high enough to make GaN and GaN-based heterostructures attractive for applications in microwave and millimetre wave devices, which may operate in a wide temperature range because of the wide energy gap and fairly good thermal conductivity ( $1.3 \text{ W cm}^{-1} \text{ K}^{-1}$  [335]). The small electron mobility in comparison to GaAs leads to higher source and drain parasitic series resistances, a lower cutoff frequency, and

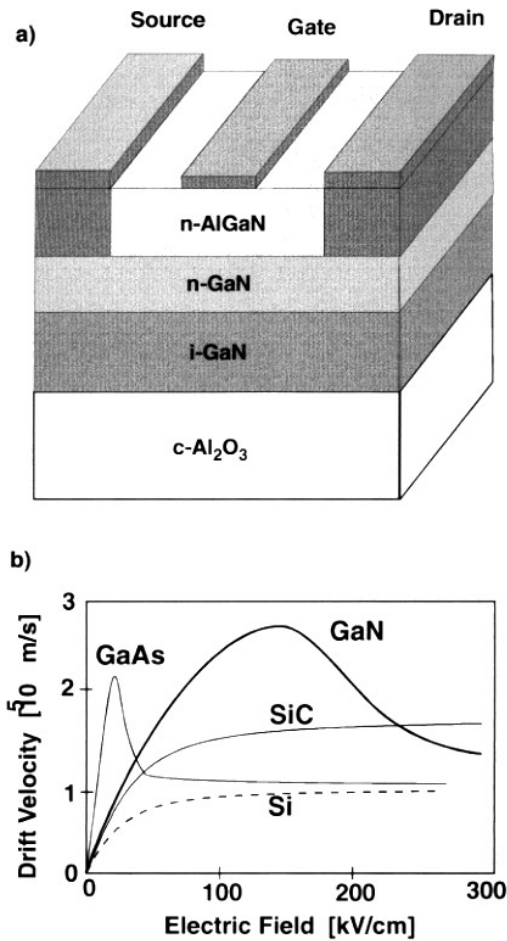


**Figure 53.** (a) Device structure of an AlGaIn/GaN heterostructure field effect transistor (HFET) [327]. (b) Electron drift velocity at 300 K versus electric field in GaN, GaAs, SiC and Si.

a lower maximum frequency of operation. However, recently reported GaN-based transistors have demonstrated outstanding characteristics (table 16), such as high maximum current, transconductance, breakdown voltages, and reasonably high cutoff frequencies. A 0.25  $\mu\text{m}$  gate length AlGaIn/GaN-doped-channel heterojunction FET grown by MOCVD with a cutoff frequency  $f_t$  of 36 GHz and a maximum oscillator frequency  $f_{\text{max}}$  of 70 GHz has been reported by Khan *et al* [336], following the first demonstration of microwave transistors with  $f_t$  at 11 GHz and  $f_{\text{max}}$  at 14 GHz [327]. MODFETs fabricated using heterostructures grown by MBE with excellent DC characteristics, such as a high maximum current of 600  $\text{mA mm}^{-1}$ , transconductance of 200  $\text{mS mm}^{-1}$  and a gate-drain breakdown of up to 200 V with 4  $\mu\text{m}$  gate-drain spacing were reported by Fan *et al* [337]. AlGaIn/GaN MODFETs with high-quality unintentionally doped channels directly grown on sapphire substrates by MOCVD showed the highest reported breakdown voltage of 340 V with 3  $\mu\text{m}$  gate-drain spacing [338,339]. High current levels over 500  $\text{mA mm}^{-1}$ , large transconductances of 160  $\text{mS mm}^{-1}$  and high breakdown voltages of 220 V with 3  $\mu\text{m}$  gate-drain spacing were simultaneously

achieved. At biases higher than 10 V, the  $f_t$  exceeded that reported for GaAs MESFETs with the same gate length. This is consistent with the greater high-field electron velocity of GaN [340].

A power density of about 3  $\text{W mm}^{-1}$  at 2 GHz was achieved with 3  $\mu\text{m}$  gate-drain spacing devices, despite the serious self-heating due to the poor thermal conductivity of the sapphire substrate. The large currents and large voltages required for high-power applications of transistors cause self-heating effects related to power dissipation problems. Growing AlGaIn/GaN structures on SiC substrates decreases the self-heating effects. In HFETs grown on 6H-SiC, the maximum dissipated DC power is at least three times higher than in similar devices grown on sapphire due to the effective heat sinking through a SiC substrate, which has a high thermal conductivity [341]. Further optimization of the growth of transistor heterostructures on SiC is therefore expected to give an additional impulse to the fabrication of AlGaIn/GaN power devices.

Electron concentration profiles have been obtained by Yu *et al* [342] for AlGaIn/GaN FETs. Analysis of the measured electron distributions demonstrates the influence of piezoelectric effects in coherently strained layers on heterostructure device characteristics. Characterization of nominally undoped  $\text{Al}_{0.15}\text{Ga}_{0.85}\text{N/GaN}$  transistors reveals the presence of a high sheet carrier density in the GaN channel which may be explained as a consequence of piezoelectrically induced charges present at the AlGaIn/GaN interface. Depending on the polarity of the heterostructure, electrical fields induced by spontaneous and piezoelectric polarization can lead to an increase or decrease of the electron sheet concentration in the channel of the transistor. In the case of an increase, the piezoelectric field and channel doping can result in an electron sheet concentration as high as  $10^{13} \text{ cm}^{-2}$ . The carriers will be confined more closely to the AlGaIn/GaN interface (which also means closer to the gate contact) which will reduce the turn-off voltage of the transistor. Eastman [343] fabricated piezoelectric HEMTs by using MOCVD-grown intentionally undoped  $\text{Al}_{0.3}\text{Ga}_{0.7}\text{N/GaN}$  heterostructures. A 0.15  $\mu\text{m}$  gate length resulted in a cutoff frequency  $f_t$  of 67 GHz and a maximum oscillator frequency  $f_{\text{max}}$  of 140 GHz. Increasing the gate length to 0.3  $\mu\text{m}$  resulted in transistors with an output power of 1.4  $\text{W mm}^{-1}$  at 3 GHz [343].

The realized transconductances, source-drain currents and cutoff frequencies of AlGaIn/GaN-based HEMTs indicate the great potential of the Group III-nitrides for the next generation of high-temperature and high-power devices. For future applications it will also be very interesting to study the potential of Group III-nitrides for the fabrication of GaN/SiC heterobipolar transistors (HBTs) and static induction transistors (SITs) for high-speed and very high power devices.

#### 9.4. LEDs and displays

Efficient radiative recombination in semiconductors has permitted the development of light-emitting devices. The

**Table 16.** Electrical properties of different AlGaN/GaN-based transistor structures.

Transistor	Heterostructure	Source drain Gate length Gate width ( $\mu\text{m}$ )	$f_t$ (GHz)	$f_{\text{max}}$ (GHz)	Gain (dB)	Power (W mm $^{-1}$ )	Breakdown voltage (V)
HFET [343]	$\text{Al}_{0.3}\text{Ga}_{0.7}\text{N}/\text{GaN}$	0.15–0.33	67	140	12.8	1.4	70
HFET [336]	$\text{Al}_{0.25}\text{Ga}_{0.75}\text{N}/\text{GaN}$	0.25–0.7	37.5	80		2.3–2.8	
DHC MODFET [337]	$\text{Al}_{0.15}\text{Ga}_{0.85}\text{N}/\text{GaN}/$ $\text{Al}_{0.15}\text{Ga}_{0.85}\text{N}/\text{GaN}$	3 1.5–1.75 40					80
MODFET [338]	$\text{Al}_{0.15}\text{Ga}_{0.85}\text{N}/\text{GaN}$	4 1.0–1.5 75	9.6	27.2	5.1	2	230–340
MODFET [303]	$\text{Al}_{0.2}\text{Ga}_{0.8}\text{N}/\text{GaN}$						
MODFET [339]	$\text{Al}_{0.175}\text{Ga}_{0.825}\text{N}/\text{GaN}$	0.4 0.25 100	50	92	6.2	1.7	80
Transistor	$n_e$ (cm $^{-3}$ )	Channel current (mA mm $^{-1}$ )	Trans- conductance (mS mm $^{-1}$ )	Mobility (300 K) (cm $^2$ V $^{-1}$ s $^{-1}$ )			
HFET [343]							
HFET [336]	$1.5 \times 10^{13}$	700	160				
DHC MODFET [337]	$3.7 \times 10^{13}$	1100	270	304			
MODFET [338]		300	130	1500			
MODFET [303]	$1.3 \times 10^{13}$			2019			
MODFET [339]	$8 \times 10^{12}$	800	240	1200			

light-emitting diode (LED) advanced from an exploratory research stage to industrial fabrication and application within a surprisingly short time. Since the LED is a simple, rugged, long-lived and inexpensive device, which efficiently converts electrical energy into incoherent light, it has a growing number of rather diverse applications. LEDs have found application and will continue to expand their applications in displays, lighting, indicator lights, traffic signs and signals, as light sources for accelerated photosynthesis, and in medicine for diagnosis.

Much research has been done to develop high-brightness blue-light-emitting diodes for use in full colour displays and indicators. For these purposes, II–VI materials such as ZnSe [344], SiC [345] and III–V nitride semiconductors have been investigated. The recent performance of II–VI green LEDs includes an output power of 1.3 mW, external quantum efficiency of 5.3% at a forward current of 10 mA, and a peak wavelength of 512 nm [346]. The lifetime of II–VI-based devices is still short and this has hindered commercialization of II–VI optoelectronic devices.

Violet electroluminescence in Mg-doped GaN was obtained 20 years ago [347–350]. The LEDs used were MIS structures in which the semiconductor was highly n-type, undoped GaN, and the insulating region was obtained by doping with deep acceptors. Magnesium doping produced diodes with violet light emitted from discrete microscopic spots, for forward voltages greater than 8 V. Later work resulted in MIS diodes with improved

efficiency: 0.3% for green, 1% for yellow and  $5 \times 10^{-6}\%$  for UV and violet emission at 77 K [351, 352].

As already mentioned, p-type conduction of Mg-doped GaN was realized for the first time by Amano *et al* [237], by low-energy electron beam irradiation (LEEBI). On the basis of these results, p–n junctions were fabricated. Undoped n-type GaN ( $n_e = 2 \times 10^{17}$  cm $^{-3}$ ) with a thickness of 3  $\mu\text{m}$  was grown on a low-temperature AlN buffer layer using  $\text{Me}_3\text{Ga}$  and ammonia. The n-type layer was followed by a 500 nm thick Mg:GaN film with a Mg concentration of  $2 \times 10^{20}$  cm $^{-3}$ . The top layer was treated with LEEBI, and an Al electrode was deposited on the top and on the side of the p–n junction. The electroluminescence spectrum of the LED showed a strong near-band-edge UV emission ( $\approx 370$  nm)—a first for a true p–n junction.

A blue p–n-LED (Si:GaN/Mg:GaN) was developed by Nakamura and co-workers in 1991 [353]. The GaN films were grown by two-flow MOCVD (TF-MOCVD) using  $\text{Me}_3\text{Ga}$ ,  $\text{NH}_3$ ,  $\text{SiH}_4$  and  $\text{Cp}_2\text{Mg}$ . A 4  $\mu\text{m}$  thick n-type GaN layer was grown ( $n_e = 5 \times 10^{18}$  cm $^{-3}$ ) and then a 0.8  $\mu\text{m}$  thick p-type layer ( $n_h = 8 \times 10^{18}$  cm $^{-3}$ ) on top of it was activated by LEEBI. One side of the p-type layer was etched away to expose the n-type layer. A Au contact was evaporated onto the p-layer and an Al contact onto the n-layer. The peak wavelength and the FWHM of the observed electroluminescence were 430 nm and 55 nm respectively. At a forward voltage as low as 4 V and a current of 20 mA, the output power was 42  $\mu\text{W}$  and the external quantum efficiency 0.18% (figure 54).



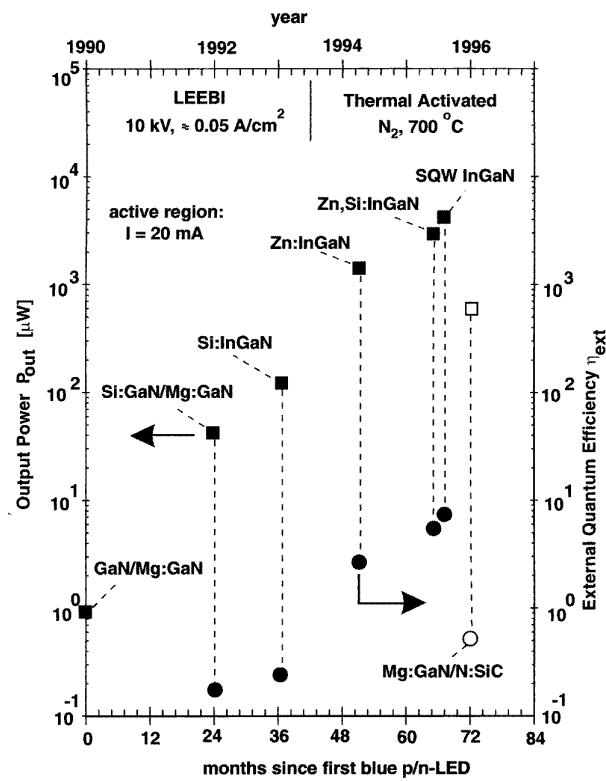


**Figure 54.** Output power and external quantum efficiency of GaN- or InGaN-based LEDs (forward current 20 mA) fabricated by Nakamura *et al* versus time scale [353–356]. The output power and efficiency of a GaN/SiC LED is given for comparison [345].

The next improvement in the blue LED was the growth of a 20 nm thick  $\text{Si:In}_{0.2}\text{Ga}_{0.8}\text{N}$  active layer between the n- and p-type GaN films, at a substrate temperature of 800 °C using  $\text{Me}_3\text{Ga}$ ,  $\text{Me}_3\text{In}$  and  $\text{SiH}_4$ . The p-GaN/n-InGaN/n-GaN double-heterostructure LEDs had an output power of 125  $\mu\text{W}$  and an external quantum efficiency of 0.22% for a forward current of 20 mA and a voltage of 19 V. The electroluminescence had a peak wavelength of 440 nm and a FWHM of 180 meV [253]. A high-brightness InGaN/AlGaIn double-heterostructure LED with luminous intensity over 1 cd, output power of 1500  $\mu\text{W}$ , and an efficiency of 2.7% ( $I = 20$  mA,  $U = 3.6$  V) was then fabricated in 1993 [354]. After GaN growth, a Si-doped  $\text{Al}_{0.15}\text{Ga}_{0.85}\text{N}$  layer was grown to a thickness of 0.15  $\mu\text{m}$ . The deposition temperature was then lowered to 800 °C to grow a 50 nm thick Zn-doped  $\text{In}_{0.06}\text{Ga}_{0.94}\text{N}$  layer as the active region of the diode. To realize electrical confinement in the active region, a  $\text{Mg:Al}_{0.15}\text{Ga}_{0.85}\text{N}$  layer of 0.15  $\mu\text{m}$  thickness was deposited at 1020 °C, followed by the p-type GaN. After growth, thermal annealing in  $\text{N}_2$  was performed (instead of LEEBI) to activate the p-type layers.

Until 1994 a blue LED with a brightness over 1 cd had not been fabricated. Then Nakamura reported highly efficient InGaN/AlGaIn double-heterostructure LEDs with an external quantum efficiency of 5.4%, which were fabricated by co-doping Zn and Si into the InGaN active layer [355]. Ohmic contacts were realized with Ni/Au on the p-type GaN and Ti/Al metallization on the n-type GaN.

The output was as high as 3 mW at a forward current of 20 mA (3.6 V). The peak wavelength and the FWHM of the electroluminescence were 450 and 70 nm respectively. The Zn and Si co-doped  $\text{In}_{0.06}\text{Ga}_{0.84}\text{N}$  layer was grown for 20 min with a deposition rate of 0.8  $\text{\AA s}^{-1}$  ( $d = 100$  nm) at a substrate temperature of 800 °C. The visibility of the violet emission originating from  $\text{In}_x\text{Ga}_{1-x}\text{N}$  ( $x < 0.2$ ) band-to-band recombination was insufficient for display use. Therefore Si and Zn were incorporated, creating donor and acceptor levels 20–30 meV below the conduction band and 0.4–0.5 eV above the valence band, enhancing the radiative recombination and reducing the energy difference between the electron and hole states to approximately 2.8 eV, yielding blue-violet electroluminescence.

Green and yellow LEDs were fabricated for application in displays and traffic lights by increasing the indium fraction of the InGaIn active layer. Without using Zn or Si, the active region of the LEDs was formed by a single quantum well (SQW) structure with a 20  $\text{\AA}$  InGaIn layer. The active undoped InGaIn layer was sandwiched between a 50 nm, Si-doped  $\text{In}_{0.05}\text{Ga}_{0.95}\text{N}$  and a 100 nm  $\text{Mg:Al}_{0.1}\text{Ga}_{0.9}\text{N}$  barrier layer. The Si-doped InGaIn layer was used to reduce strain in the active region. The indium fraction of the active layer was varied between 0.2 and 0.7 in order to change the peak wavelength from blue to yellow. By growing very thin InGaIn layers, it was possible to vary the In content over a wide range and to omit doping by Si and Zn, without a reduction of the efficiency (figures 55 and 56). The peak wavelength (and the FWHM) of the blue, green and yellow LEDs were 450 (20), 525 (45) and 590 nm (90 nm) respectively. At a forward current of 20 mA ( $U \approx 3.0$  V), the output power and external quantum efficiency of blue SQW LEDs are 4 mW and 7.3%; green LEDs, 1.5 mW and 2.1%; and yellow LEDs, 0.5 mW and 1.2% respectively. The conventional green GaP LED with a peak wavelength of 555 nm has an output of 0.04 mW, and the output power of green AlInGaP LEDs with a peak wavelength of 570 nm is 0.4 mW [356]. Therefore the output power of green InGaIn SQW LEDs is much higher than that of conventional yellowish green LEDs.

Nakamura *et al* also introduced a white LED, now being commercialized by Nichia which consists of a blue LED, similar to the LEDs just described, and packaged with a yttrium aluminium garnet (YAG) phosphor to convert blue into white light (figure 57). The white LED has an external quantum efficiency of 3.5% and an output of 1 mW (5 lm  $\text{W}^{-1}$ ). White LEDs are interesting for applications in which small light bulbs are used, because of the longer lifetime and better conversion efficiency of electric power to visible light compared to incandescent lamps.

If LEDs of primary colours can be made with a high output intensity, flat displays can be built for indoor and outdoor applications, consisting of several thousand LEDs [357]. For example, the dimensions of a commercial Toshiba display module are 128 mm  $\times$  256 mm, and it contains 2048 discrete LEDs. A relatively modest panel of 1.28 m  $\times$  2.56 m requires one hundred modules, or 204 800 LEDs. In a Sharp module, the pixels are closer together, because higher resolution is desirable for indoor



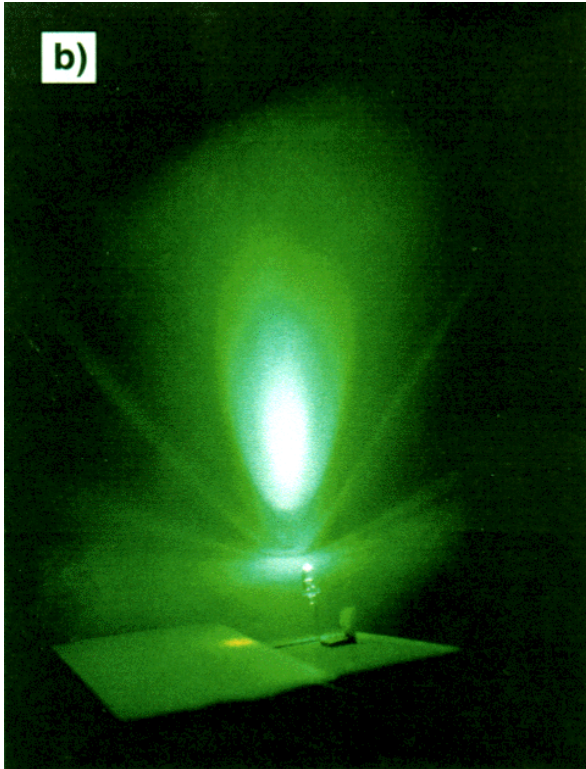
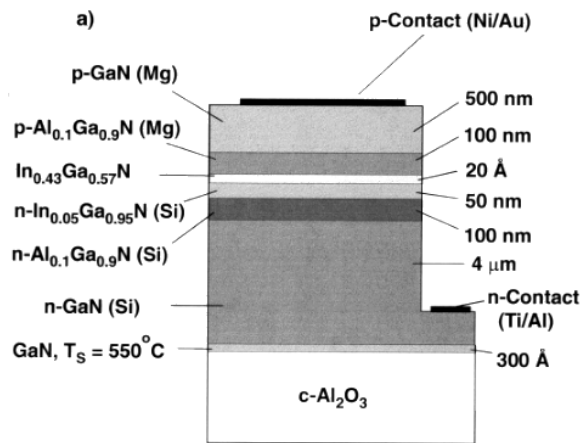


**Figure 55.** (a) The structure of the high-brightness green-light-emitting diode with a 20 Å thick  $\text{In}_{0.43}\text{Ga}_{0.57}\text{N}$  quantum well as active region. (b) The output power, the external quantum efficiency, and the luminous intensity of a green LED at a forward current of 20 mA are 1 mW, 2.1% and 4 cd respectively.

applications. The dimensions are half of the Toshiba module and each contains 512 lamps or 1536 LED chips. For the same panel size as above, 400 modules or 614 400 LEDs would be needed. These numbers give a feeling for how big the market for LEDs really is. In 1994 (before the commercialization of Group III-nitride LEDs), visible wavelength LEDs already accounted for 33%, and infrared LEDs for 26% of the \$4.4 billion compound semiconductor market. Furthermore the successful development and fabrication of green and blue LEDs provided the foundation for growth of nitride-based heterostructures suitable for blue-emitting laser diodes.

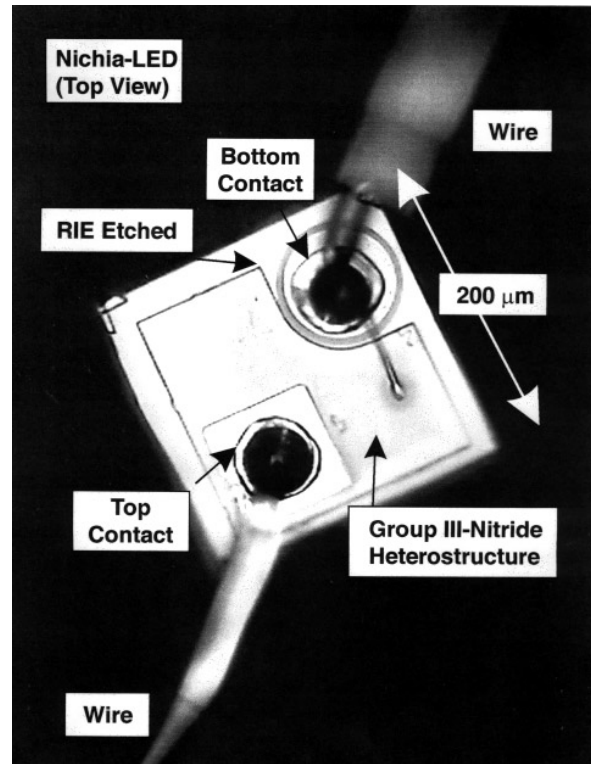


**Figure 56.** Surface micrograph (top view) of a blue LED fabricated by Nichia, without plastic capsule.

### 9.5. Stimulated emission and lasers

At present, a main focus of III-V nitride research is the realization of the shortest wavelength electrically pumped semiconductor laser diode. These diodes, operating in the blue and near-UV spectral range, would be useful in a variety of applications requiring high resolution, such as high-speed laser printers, scanners, and high-density optical data storage devices.

Optically pumped stimulated emission from GaN was first observed in 1971 by Dingle *et al* [358]. Stimulated emission and laser action was observed near 3.45 eV in single-crystal GaN needles with electron concentrations exceeding  $10^{19} \text{ cm}^{-3}$ . The structure of the emitted light was interpreted as Fabry-Pérot modes which appeared for pump beam intensities from a pulsed  $\text{N}_2$  laser above  $0.3 \text{ MW cm}^{-2}$ . Optical gains as high as  $10^5 \text{ cm}^{-1}$  were measured for the highest pumping powers.

Since the development of efficient nitride LEDs, many researchers are again working towards the optimization of laser diode structures. An optically pumped GaN-based vertical cavity surface emitting laser (VCSEL) was demonstrated by Redwing *et al* [359]. Laser emission near 363 nm was observed at room temperature from the surface of the VCSEL structure, optically pumped through a cleaved sample edge with focused light (337 nm) from a pulsed nitrogen laser. The VCSEL structure, which was grown on a  $c\text{-Al}_2\text{O}_3$  substrate by MOCVD, consists of a very thick (10 μm) GaN active region sandwiched between two 30-period,  $\text{Al}_{0.4}\text{Ga}_{0.6}\text{N}/\text{Al}_{0.12}\text{Ga}_{0.88}\text{N}$  (397 Å/372 Å),

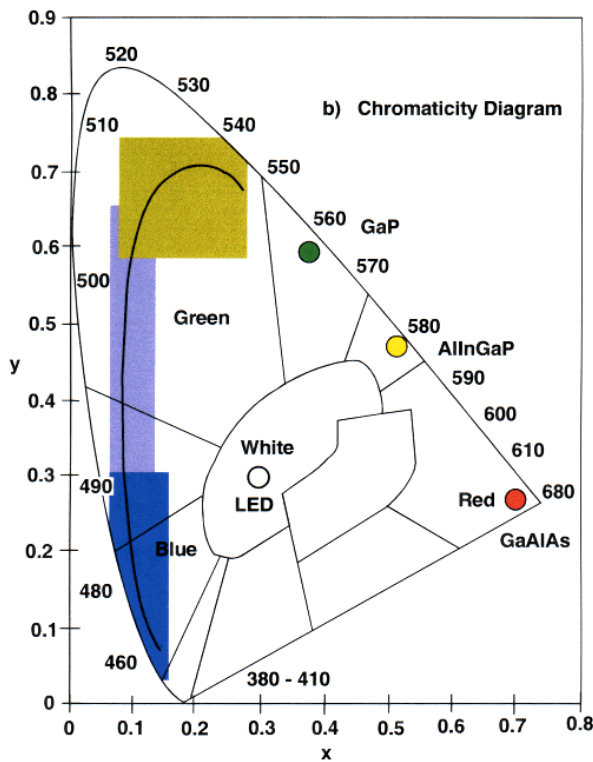


**Figure 57.** Chromaticity diagram. The positions of the GaP, AlInGaP and GaAs LEDs are marked with coloured circles. The region of the diagram which can be covered by InGaN based LEDs is indicated. By combining InGaN with GaAlAs LEDs, nearly the whole visible spectra can be produced. White light is generated by converting the light of a blue LED with yttrium aluminium garnet phosphor.

Bragg reflector stacks. At optical pump intensities above  $2 \text{ MW cm}^{-2}$ , a narrow ( $<5 \text{ Å}$ ) laser mode at  $363.5 \text{ nm}$  emerges from the GaN photoluminescence spectrum. This mode increases very rapidly with increasing pump intensity and becomes the dominant feature of the spectrum at higher pump powers. This was the first unambiguous evidence of laser action in a GaN-based vertical cavity structure.

Room-temperature distributed-feedback (DFB) laser operation was demonstrated by Hofmann *et al* [360]. The GaInN/GaN double heterostructure was grown on a (0001) sapphire substrate by low pressure MOCVD. The double heterostructure consists of a  $450 \text{ nm}$  thick GaN buffer and cladding layer, a  $15 \text{ nm}$   $\text{In}_{0.06}\text{Ga}_{0.92}\text{N}$  active layer and a  $100 \text{ nm}$  GaN top cladding layer. The grating of the DFB structure, with a period of  $161.5 \text{ nm}$ , was defined on the top GaN layer by high-resolution electron beam lithography using PMMA as a resist and dry etching with the ECR-rf plasma method using an  $\text{Ar}/\text{CCl}_2\text{F}_2$  gas mixture. The etch depth of the grating was  $50 \text{ nm}$ , and the lateral confinement of the laser modes was provided by a  $6 \text{ μm}$  wide ridge waveguide. The overall length of the cavity was  $1000 \text{ μm}$ . The DFB resonator was optically pumped with a pulsed XeCl excimer laser ( $308 \text{ nm}$ ), and laser emission was observed in a wavelength range from  $389$  to  $399 \text{ nm}$  for pump power densities above  $100 \text{ MW cm}^{-2}$ .

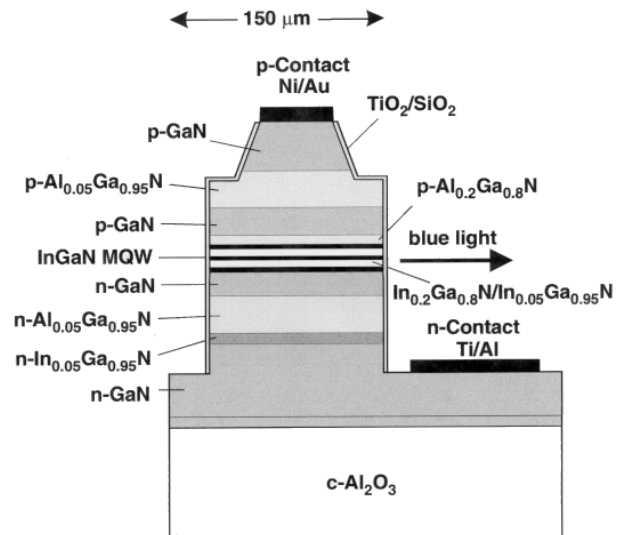


**Figure 58.** Schematic cross section of the continuous wave operating InGaN multiple quantum well structure laser diode [366].

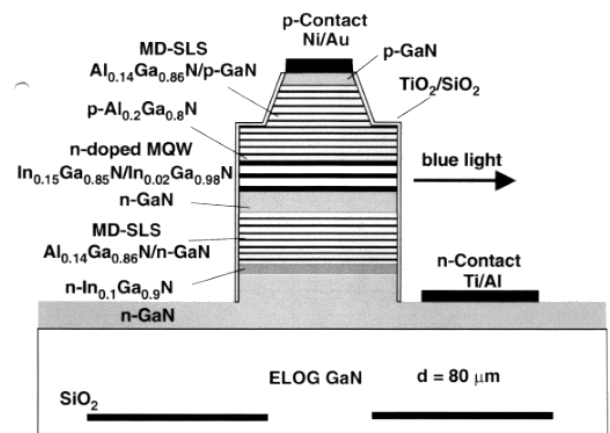


**Figure 59.** Structure of the InGaN MQW structure laser diode grown on a GaN LEO substrate by using AlGaIn/GaN superlattices instead of  $500 \text{ nm}$  thick AlGaIn cladding layers [367, 368].

Edge-emitting InGaN multiple quantum well (MQW) laser diodes were fabricated by Nakamura *et al* [165] and consisted of: a  $30 \text{ nm}$  GaN buffer layer grown at a low temperature of  $550^\circ\text{C}$ ; a  $3 \text{ μm}$  thick layer of n-type GaN:Si; a  $0.1 \text{ μm}$  thick layer of n-type  $\text{In}_{0.1}\text{Ga}_{0.9}\text{N}$ :Si; a  $0.4 \text{ μm}$  thick layer of n-type GaN:Si; 26 periods of a  $\text{In}_{0.2}\text{Ga}_{0.8}\text{N}/\text{In}_{0.05}\text{Ga}_{0.95}\text{N}$  MQW ( $24 \text{ Å}/50 \text{ Å}$ ); a  $20 \text{ nm}$  thick layer of  $\text{Al}_{0.2}\text{Ga}_{0.8}\text{N}$ :Mg; and a  $0.1 \text{ μm}$  thick layer of p-type GaN:Mg. RIE was employed to form mirror cavity facets. The dimensions of the laser cavity were  $30 \times 1500 \text{ μm}^2$ . A Ni/Au contact was evaporated onto the entire area of the p-type GaN layer, and a Ti/Al contact onto the n-type GaN layer. The electrical characteristics of the laser diode were measured under pulsed current-biased conditions (pulse width  $1\text{--}2 \text{ μs}$ , pulse period  $1\text{--}2 \text{ ms}$ ) at room temperature. Stimulated emission at  $417 \text{ nm}$  (FWHM =  $1.6 \text{ nm}$ ) was observed above a threshold current

**Table 17.** Optical and electrical data of pulsed blue-emitting laser diodes grown on different substrate materials (*c*-Al<sub>2</sub>O<sub>3</sub>, *a*-Al<sub>2</sub>O<sub>3</sub> and MgAl<sub>2</sub>O<sub>4</sub>) [361, 362].

	Substrate		
	<i>c</i> -Al <sub>2</sub> O <sub>3</sub>	<i>a</i> -Al <sub>2</sub> O <sub>3</sub>	MgAl <sub>2</sub> O <sub>4</sub> (111)
Wavelength of emission (nm)	417	415.6	410
FWHM of EL (nm)	1.6	0.05	2.1
Number of QWs	26	20	20
Output power per facet (mW)	215	76	44
Forward current (A)	2.3	1.5	1.7
Current density (kA cm <sup>-2</sup> )	4	9.6	8
External voltage (V)	34	26	28
Pulsed current injection:			
pulse width (μs)	2	1	1
pulse period (ms)	2	1	1
Differential quantum efficiency per facet (%)	13	4.2	3.3
Resonator size (μm <sup>2</sup> )	30 × 1500	20 × 1200	20 × 1500
Mirrors	Cavity facets formed by RIE	RIE etching of p-GaN cleaved along (1102)	Polished facets
Electrical contacts:			
for p-type	Ni/Au	Ni/Au	Ni/Au
for n-type	Ti/Al	Ti/Al	Ti/Al

density of 4 kA cm<sup>-2</sup> ( $I \geq 1.7$  A,  $V \geq 34$  V). A differential quantum efficiency of 13% per facet and a pulsed output power of 215 mW per facet were obtained at a current of 2.3 A.

This performance was then improved by using seven InGa<sub>0.12</sub>Ga<sub>0.88</sub>N quantum wells instead of 26. The threshold current density was 9.6 kA cm<sup>-2</sup> ( $I \geq 1.15$  A) and the voltage threshold was reduced to 20 V. The key layer, from the growth perspective, is the 100 nm In<sub>0.1</sub>Ga<sub>0.9</sub>N layer below the Al<sub>0.12</sub>Ga<sub>0.88</sub>N lower cladding layer, which is reported to prevent cracking in the AlGa<sub>0.88</sub>N. Also, a 20 nm Al<sub>0.2</sub>Ga<sub>0.8</sub>N layer is employed directly above the MQW active region to suppress In desorption. GaN lasers were grown on both *a*-face and *c*-face sapphire [361]. Nakamura's very important result was that he could obtain cleaved facets when growing on *a*-face sapphire, because the *r*-face cleavage facet is perpendicular to this surface. The cleaved facets of the epitaxial layers (laser diode) and the substrate were mirror-like and could be used as laser cavity mirrors. The mirrors were subsequently coated for high reflectivity with two pairs of quarter-wave TiO<sub>2</sub>/SiO<sub>2</sub> dielectric multilayers to further reduce the threshold current density (table 17). Besides the devices grown on *a*- or *c*-face sapphire by Nakamura *et al.*, pulsed laser operation has also been demonstrated by other groups on various substrates, for example Al<sub>2</sub>O<sub>3</sub> [362, 363], MgAl<sub>2</sub>O<sub>4</sub> [364] and SiC [365], but to date with higher current thresholds and relatively short device lifetimes.

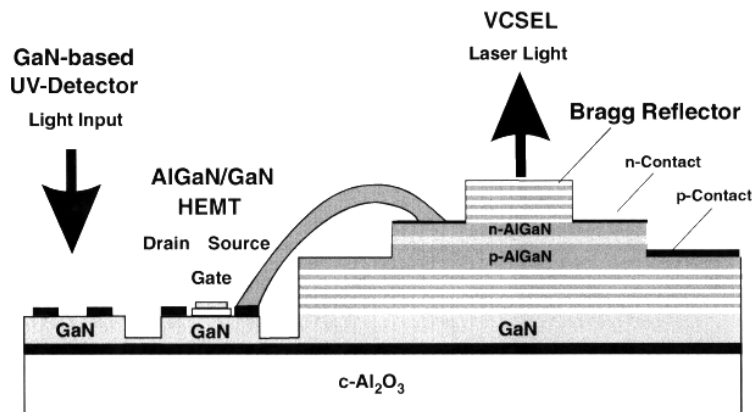
Continuous wave (CW) operation was also demonstrated at 233 K by Nakamura *et al.* [366]. The MQW structure consists of three 40 Å thick undoped In<sub>0.2</sub>Ga<sub>0.8</sub>N well layers forming the gain medium, separated by 80 Å thick undoped In<sub>0.08</sub>Ga<sub>0.92</sub>N barrier layers. The area of the ridge geometry laser diode was modified to 4 × 600 μm<sup>2</sup>, but the rest of the laser structure was almost the same as described previously. A differential quantum efficiency of 8% per facet and an output power of 9.5 mW per facet

were obtained at a current of 250 mA and an operating voltage of 14 V. The threshold current of 210 mA and voltage of 11 V were reduced by improvement of the ohmic contacts and the doping profiles. The laser diodes were destroyed within one second due to heat generation when they were operated at room temperature. Under CW operation at 233 K, the lifetime was longer than 30 min (figure 58, table 18).

By further optimization of the growth, the threshold voltage and current were reduced to 5.5 V and 80 mA respectively and the threshold current density to 3.6 kA cm<sup>-2</sup>. An internal quantum efficiency of 86%, an intrinsic loss of 54 cm<sup>-1</sup>, and a threshold gain of 110 cm<sup>-1</sup> were obtained. Measuring the pulse response of the laser diode, a carrier lifetime of 2.5 ns and a threshold carrier density of 1.3 × 10<sup>19</sup> cm<sup>-3</sup> were determined. The emission wavelength of the laser was around 406 nm and could be measured for an operating time of 36 h at room temperature. The structural quality and the current threshold and lifetime of the laser structures were drastically influenced by the difficulties of growing the thick AlGa<sub>0.88</sub>N cladding layers required for optical confinement, due to the formation of cracks during growth and the high dislocation density inside the active region of the laser diodes. Therefore, in order to prevent the formation of cracks and dislocations due to the lattice mismatch between AlGa<sub>0.88</sub>N and GaN, strained layer superlattices (120 periods of 2.5 nm thick Mg-doped GaN separated by 2.5 nm thick Al<sub>0.14</sub>Ga<sub>0.86</sub>N layers (MD-SLS)) were grown instead of one thick AlGa<sub>0.88</sub>N cladding layer [367]. For further reduction of the dislocation density, the laser diode was grown on top of a LEO substrate (section 4.5.3) [368]. Selective growth of GaN was performed on a 2 μm thick MOCVD GaN layer deposited on a sapphire substrate. A 100 nm thick silicon dioxide mask was patterned to form 4 μm wide stripe windows with a periodicity of 11 μm in the GaN  $\langle 1100 \rangle$  direction. Following a 10 μm GaN growth on the patterned substrate,

**Table 18.** Structure of the continuous-wave operating InGaN MQW-structure laser diode. The thickness and the functionality of the different layers are given [366].

Material/dopant	Thickness (nm)	Function
Al <sub>2</sub> O <sub>3</sub> or MgAl <sub>2</sub> O <sub>4</sub>		Substrate
GaN	30–50	Nucleation layer
GaN:Si	3000	Bottom contact of the LD, reduction of structural defects
In <sub>0.05</sub> Ga <sub>0.95</sub> N:Si	100	Buffer layer for AlGaN, prevents cracking
Al <sub>0.15</sub> Ga <sub>0.85</sub> N:Si or Al <sub>0.05</sub> Ga <sub>0.95</sub> N:Si	500	Cladding layer for optical confinement
GaN:Si	100 or 70	Light-guiding layer
In <sub>0.2</sub> Ga <sub>0.8</sub> N/In <sub>0.05</sub> Ga <sub>0.95</sub> N or In <sub>0.15</sub> Ga <sub>0.85</sub> N/In <sub>0.05</sub> Ga <sub>0.95</sub> N	3 × 4/8	MQW, active region of the LD
Al <sub>0.2</sub> Ga <sub>0.8</sub> N:Mg	20	Prevents dissociation of the MQW during growth of p-type layers
GaN:Mg	100 or 70	Light-guiding layer
Al <sub>0.15</sub> Ga <sub>0.85</sub> N:Mg or Al <sub>0.05</sub> Ga <sub>0.95</sub> N:Mg	500	Cladding layer for optical confinement
GaN:Mg	200	Top contact of the LD
TiO <sub>2</sub> /SiO <sub>2</sub>	Two pairs	High-reflectivity facet coating

**Figure 60.** Schematic cross section of a possible future monolithically integrated photonic switch device using AlGaIn/GaN-based devices such as a UV photoconductor, a MESFET or a VCSEL.

coalescence of the selectively grown GaN made it possible to achieve a flat GaN surface over the entire substrate. GaN growth was continued up to a thickness of 100  $\mu\text{m}$ . Then the sapphire substrate was removed by polishing in order to obtain a pure GaN substrate of thickness about 80  $\mu\text{m}$ . The InGaN MQW laser diode structure shown in figure 59 was grown on the surface of that substrate. Under room temperature CW operation, the threshold current of the laser diode with a cavity length of 450  $\mu\text{m}$  was 53 mA, which corresponds to a threshold current density of 3  $\text{kA cm}^{-2}$ . The operating voltage at the threshold current was 4.9 V. Under a constant output intensity of 2 mW per facet, the best laser structure showed a lifetime of more than 3000 h, and from the very weak increase of operating current with time, the total lifetime of the laser could be estimated to be 10 000 h. If laser diodes with such a long lifetime could be reliably produced, they could be commercialized for applications like optical storage devices. The optimization of blue laser diodes towards higher output intensity would be desirable for optical sensors and scanners.

## 10. Future trends

In the past, the poor quality of material, the lack of p-type doping and the absence of reliable etching procedures thwarted engineers and scientists from fabricating useful devices from Group III-nitrides. All of these obstacles have recently been sufficiently overcome, so that electrical and optical devices fabricated from such materials have been demonstrated and partially commercialized.

Great improvements in device properties were enabled mainly by the use of MOCVD-grown material, due to a dramatic reduction of structural defects in epitaxial layers and heterostructures using low-temperature buffer layers, selective growth and strained layer superlattices. These techniques were necessary to reduce the density of structural defects caused by the large mismatch of lattice constants and thermal expansion coefficients between Group III-nitrides and available substrate materials. A trend for the future is the development of GaN substrates for homoepitaxy by fabricating GaN bulk crystals using high-pressure techniques or by deposition of very thick epitaxial

GaN films by HVPE, SSM or MOCVD. Thick GaN layers can be removed from the substrate by polishing or light-induced thermal decomposition processes and used as substrates. GaN substrates will enable MBE techniques in particular to produce Group III-nitride heterostructures with a high accuracy and at relatively low substrate temperatures. The deposition of nitrides at lower substrate temperatures is particularly advantageous for the growth of InGaN, AlInN and AlInGaN layers with high concentrations of indium. High indium containing alloys offer the possibility of bandgap engineering together with the fabrication of lattice-matched heterostructures. The deposition of lattice-matched structures will lead to a further reduction of structural defects and therefore to an improvement of the electrical and optical properties of complex devices.

High-luminosity yellow, green, blue and white emitting diodes are now commercialized. Optical detectors, GaN-based heterostructures, have demonstrated operation in the blue and near-ultraviolet spectral range. These products should find wide use in applications such as full colour displays, traffic signs, UV detectors, automobile and aircraft lighting. Recent results suggest that the lifetime of the blue GaN CW laser diode can be improved beyond 3000 h with output powers of 2 mW, even at room temperature. Such a laser diode, operating at room temperature with a lifetime of several 1000 h will be instrumental for high-density CD-ROMs with a storage capacity of up to 10 Gbit/inch<sup>2</sup>. There is still potential for further reduction of the laser wavelength to the near-UV spectral range by using GaN or AlGaIn/GaN MQWs as active layers. An additional decrease in wavelength will further enhance the information density of optical storage and perhaps enable the fabrication of optical sensors for molecules with absorbances in the near-UV.

In the electronic device area, field effect transistors, particularly MODFETs with high transconductances and high source-drain currents, should have a promising future because of their potential to operate as high-temperature and high-power microwave devices. To date only a few groups have published results on the successful fabrication of GaN HBT and SIT devices which are suitable for high-speed and very high power devices. A combination and comparison of the electrical properties of SiC- and GaN-based devices for high-power and high-temperature applications would be very interesting.

The development of epitaxial AlN on Al<sub>2</sub>O<sub>3</sub>, for potential use in a composite structure containing both piezoelectric and semiconducting material, would make a number of integrated systems possible. A prime example is a SAW programmable tappable delay line, where both an AlN delay line and silicon diodes and MOS devices are integrated on a Al<sub>2</sub>O<sub>3</sub> substrate. These composite structures are ideal for the fabrication of converters and correlators.

The outstanding physical properties of Group III-nitrides enable the fabrication of LEDs, lasers, detectors, transistors, surface acoustic wave devices and offer a valuable combination of electrical, optical and piezoelectrical behaviour. Monolithic structures (figure 60) open the door for new combinations of different wide-bandgap semiconductor devices fabricated on the same substrate, which cannot be realized by any other group of materials.

## Acknowledgments

I would like to thank Dr M Kelly for encouraging and critically reading the manuscript and my collaborators and colleagues who made much of the work possible. Specifically, thanks go to Professor M Stutzmann, R Dimitrov, Dr W Rieger, Dr H Angerer, Dr T Metzger, Dr M Brandt, Dr A Cros, Dr G Dollinger, Professor R A Fischer, Dr A Miehr and Dr M Albrecht. The author especially thanks Dr Jürgensen (AIXTRON) for the photograph of the MOCVD apparatus and the picture of the LEDs.

## References

- [1] Osamura K, Naka S and Murakami Y 1975 *J. Appl. Phys.* **46** 3432
- [2] Brunner D, Angerer H, Bustarret E, Höppler R, Dimitrov R, Ambacher O and Stutzmann M 1997 *J. Appl. Phys.* **82** 5090
- [3] Bremser M D, Perry W G, Zheleva T, Edwards N V, Nam O H, Parikh N, Aspnes D E and Davis R F 1996 *Mater. Res. Soc. Int. J. Nitr. Semi. Res.* **1** 8
- [4] Koide Y J, Itoh H, Khan M R H, Hiramatsu K, Sawaki N and Akasaki I 1987 *J. Appl. Phys.* **61** 4540
- [5] Kim K S, Saxler A, Kung P, Razeghi R and Lim K Y 1997 *Appl. Phys. Lett.* **71** 800
- [6] Guo Q, Ogawa H and Yoshida A 1995 *J. Crystal Growth* **146** 462
- [7] Shur M, Gelmont B and Khan M A 1996 *J. Electron. Mater.* **25** 777
- [8] Uzawa Y, Wang Z, Kawakami A and Komiyama B 1995 *Appl. Phys. Lett.* **66** 1992
- [9] Yoshida S, Misawa S and Itoh A 1975 *Appl. Phys. Lett.* **26** 462
- [10] Strite S and Morkoc H 1992 *J. Vac. Sci. Technol.* **B 10** 1237
- [11] Strite S, Lin M E and Morkoc H 1993 *Thin Solid Films* **231** 197
- [12] Mohammad S N, Salvador A A and Morkoc H 1995 *Proc. IEEE* **83** 1306
- [13] Ponce F *et al* 1997 *Mater. Res. Soc. Bull.* **22** 17
- [14] Groczyca I, Christensen N E, Perlin P, Grzegory I, Jun J and Bockowski M 1991 *Solid State Commun.* **79** 1033
- [15] Shannon R D and Prewit C T 1969 *Acta Cryst.* **B 25** 925
- [16] Bernardini F, Fiorentini V and Vanderbilt D 1997 *Phys. Rev. B* **56** R10024
- [17] Edgar J H (ed) 1994 *Group III Nitrides* (London: INSPEC)
- [18] Sun C J, Kung P, Saxler A, Ohsato H, Bigan E, Razeghi M and Gaskill D K 1994 *J. Appl. Phys.* **76** 236
- [19] Sasaki T and Zembutzu S 1987 *J. Appl. Phys.* **61** 2533
- [20] Ponce F A, Bour D P, Young W T, Saunders M and Steeds J W 1996 *Appl. Phys. Lett.* **69** 337
- [21] Smith A R, Feenstra R M, Greve D W, Neugebauer J and Northrup J E 1997 *Phys. Rev. Lett.* **79** 3934
- [22] Kazimirov A, Scherb G, Zegenhagen J, Lee T-L, Bedzyk M J, Kelly M K, Angerer H and Ambacher O 1998 *Appl. Phys. Lett.* **84** 1703
- [23] Ewing R E and Greene P E 1964 *J. Electrochem. Soc.* **111** 917
- [24] Nye J F 1985 *Physical Properties of Crystals* (Oxford: Oxford University Press)
- [25] Posternak M, Baldereschi A, Catellani A and Resta R 1990 *Phys. Rev. Lett.* **64** 1777
- [26] Tsubouchi K and Miskoshiba N 1985 *IEEE Trans. Sonics Ultrason.* **32** 634
- [27] O'Clock G D and Duffy M T 1973 *Appl. Phys. Lett.* **23** 55



- [28] Littlejohn M A, Hauser J R and Glisson T H 1975 *Appl. Phys. Lett.* **26** 625
- [29] Bykhovski A D, Gelmont B L and Shur M S 1997 *J. Appl. Phys.* **81** 6332
- [30] Barker A S Jr and Ilegems M 1973 *Phys. Rev. B* **7** 743
- [31] Tsubouchi K, Sugai K and Mikoshiba N 1981 *IEEE Ultrason. Symp.* **1** 375
- [32] Wright A F 1997 *J. Appl. Phys.* **82** 2833
- [33] Takagi Y, Ahart M, Azuhato T, Sota T, Suzuki K and Nakamura S 1996 *Physica B* **219 & 220** 547
- [34] Sheleg A V and Savastenko V A 1979 *Izv. Akad. Nauk. SSSR, Neorg. Mater* **15** 1598
- [35] Kim K, Lambrecht W R L and Segall B 1996 *Phys. Rev. B* **53** 16310
- [36] Böer K W 1990 *Survey of Semiconductor Physics* (New York: Van Nostrand Reinhold) p 566
- [37] Im J S, Kollmer H, Off J, Sohmer A, Scholz F and Hangleiter A 1998 *Mater. Res. Symp. Proc.* **482** 513
- [38] Dal Corso A, Posternak M, Resta R and Baldereschi A 1994 *Phys. Rev. B* **50** 10715
- [39] Zhong W, King-Smith R D and Vanderbilt D 1994 *Phys. Rev. Lett.* **72** 3618
- [40] Yim W M and Paff R J 1974 *J. Appl. Phys.* **45** 1456
- [41] Slack G A and Bartram S F 1975 *J. Appl. Phys.* **46** 89
- [42] Ivanov S N, Popov P A, Egorov G V, Sidorov A A, Kornev B I, Zhukova L M and Ryabov V P 1997 *Phys. Status Solidi* **39** 81
- [43] Maruska H P and Tietjen J J 1969 *Appl. Phys. Lett.* **15** 327
- [44] Ejder E 1974 *Phys. Status Solidi* **a 23** K87
- [45] Lesezczynski M, Suski T, Teisseyre H, Perlin P, Grzegory I, Jun J, Porowski S and Moustakas T D 1994 *J. Appl. Phys.* **76** 4909
- [46] Leszczynski M, Teisseyre H, Suski T, Grzegory I, Bockowski M, Jun J, Palosz B and Porowski S 1996 *Acta. Phys. Polon.* **90** 887
- [47] Wang K and Reeber R R 1998 *Mater. Res. Soc. Symp. Proc.* **482** 863
- [48] Grzegory I, Krukowski S, Jun J, Bockowski M, Wroblewski M and Porowski S 1998 *High. Pressure Res.* at press
- [49] Trainor J W and Rose K 1974 *J. Electron. Mater.* **3** 821
- [50] Guo Q, Kato O and Yoshida A 1993 *J. Appl. Phys.* **73** 7969
- [51] MacChesney J B, Bridenbaugh P M and O'Conner P B 1970 *Mater. Res. Bull.* **5** 783
- [52] Johnson W, Parsons J and Crew M 1932 *J. Phys. Chem.* **36** 2651
- [53] Sime J R and Margrave J L 1956 *J. Phys. Chem.* **60** 810
- [54] Thurmond C D and Logan R A 1972 *J. Electrochem. Soc.* **119** 622
- [55] Lorenz M R and Binkowski B B 1962 *J. Electrochem. Soc.* **109** 24
- [56] Karpinsky J, Jun J and Porowski S 1984 *J. Crystal Growth* **66** 1
- [57] Madar R, Jacob G, Hallais J and Fruchart R 1975 *J. Crystal Growth* **31** 197
- [58] Class W 1968 *NASA Report CR-1171*
- [59] Slack G A and McNelly T F 1976 *J. Crystal Growth* **34** 263
- [60] Van Vechten J A 1973 *Phys. Rev. B* **7** 1479
- [61] Ambacher O, Brandt M S, Dimitrov R, Metzger T, Stutzmann M, Fischer R A, Miehr A, Bergmaier A and Dollinger G 1996 *J. Vac. Sci. Technol. B* **14** 3532
- [62] Redhead P A 1962 *Vacuum* **12** 203
- [63] Peterson N L 1978 *J. Nucl. Mater.* **69 & 70** 3
- [64] Frank W, Gösele U M, Mehrer H and Seeger A 1984 *Diffusion in Crystalline Solids* (New York: Academic) p 53
- [65] Seeger A and Chik K P 1968 *Phys. Status Solidi* **29** 455
- [66] Tan T Y, Gösele U M and Yu S 1991 *Crit. Rev. Solid State Phys.* **17** 47
- [67] Goldstein B 1960 *Phys. Rev. Lett.* **121** 1305
- [68] Palfrey H D, Brown M and Willoughby A F W 1981 *J. Electrochem. Soc.* **128** 2224
- [69] Wang L, Hsu L, Haller E E, Erickson J W, Fischer A, Eberl K and Cardona M 1995 *Phys. Rev. B* **76** 2342
- [70] Ambacher O, Freudenberger F, Dimitrov R, Angerer H and Stutzmann M 1998 *Japan. J. Appl. Phys.* **37** at press
- [71] Briegleb F and Geuther A 1862 *Ann. Chem.* **123** 228
- [72] Ahrons L 1899 *Naturwiss. Rundschau* **14** 453
- [73] Funk H and Boehland H 1964 *Z. Anorg. Allgem. Chem.* **334** 155
- [74] Johnson W C, Parsons J B and Crew M C 1932 *J. Phys. Chem.* **36** 2561
- [75] Ejder E 1974 *J. Crystal Growth* **22** 44
- [76] Li W and Ni W-X 1996 *Appl. Phys. Lett.* **68** 2705
- [77] Kobayashi N P, Kobayashi J T, Daphus P D, Choi W-J, Bond A E, Zhang X and Rich D H 1997 *Appl. Phys. Lett.* **71** 3569
- [78] Hamdani F, Yeadon M, Smith D J, Tang H, Kim W, Salvador A, Botchkarev A E, Gibson J M, Polyakov A Y, Showronski M and Morkoc H 1998 *J. Appl. Phys.* **83** 983
- [79] Kaiser S, Preis H, Gebhardt W, Ambacher O, Angerer H, Stutzmann M, Rosenauer A and Gerthsen D 1998 *Japan. J. Appl. Phys.* **37** 84
- [80] Fischer S, Gisbertz A, Meyer B K, Topf M, Koynov S, Dirnstorfer I, Volm D, Uecker R, Reiche P, Ganschow S and Liliental-Weber Z 1996 *Symp. Proc. EGN-I (Rigi, Switzerland)* 1996
- [81] Kung P, Saxler A, Zhang X, Walker D, Lavado R and Razeghi M 1996 *Appl. Phys. Lett.* **69** 2116
- [82] Okazaki H, Arakawa A, Asahi T, Oda O and Aiki K 1995 *Abstract Topical Workshop on III-V Nitrides (Nagoya)* 1995 SP8
- [83] Kuramata A, Horino K, Domen K, Shinohara K and Tanahashi T 1995 *Appl. Phys. Lett.* **67** 2521
- [84] George T, Jacobsohn E, Pike W T, Chang-Chien P, Khan M A, Yang J W and Mahajan S 1996 *Appl. Phys. Lett.* **68** 337
- [85] Sun C J, Yang J W, Chen Q, Khan M A, George T, Chang-Chien P, and Mahajan S 1996 *Appl. Phys. Lett.* **68** 1129
- [86] Hellman E S, Brandle C D, Schneemeyer L F, Wiesmann D, Brener I, Siegrist T, Berkstresser G W, Buchanan D N E and Hartford E H Jr 1996 *Mater. Res. Soc. Symp. Proc.* **395** 51
- [87] Popovici G, Kim W, Botchkarev A, Tang H, Morkoc H and Solomon J 1997 *Appl. Phys. Lett.* **71** 3385
- [88] Kelly M K, Ambacher O, Dimitrov R, Handschuh H and Stutzmann M 1997 *Phys. Status Solidi* **a 153** R3
- [89] Shaw D W 1975 *J. Crystal Growth* **31** 130
- [90] Cadoret R and Cadoret M 1975 *J. Crystal Growth* **31** 142
- [91] Wu C H, Solomon R, Snyder W L and Larsen T L 1978 *J. Electron. Mater.* **7** 791
- [92] Seifert W, Fitzl G and Butter E 1981 *J. Crystal Growth* **52** 257
- [93] Mizuno D and Watanabe H 1980 *J. Crystal Growth* **50** 702
- [94] Wickenden D K, Faulkner K R and Brandner R W 1971 *J. Crystal Growth* **9** 158
- [95] Rubenstein M and Myers E 1966 *J. Electrochem. Soc.* **113** 365
- [96] Hasegawa F, Yamaguchi H and Katayama K 1988 *Japan. J. Appl. Phys.* **27** L1546
- [97] Ilegems M 1972 *J. Crystal Growth* **13/14** 360
- [98] Molnar R J, Götz W, Romano L T and Johnson N M 1997 *J. Crystal Growth* **178** 147
- [99] Götz W, Romano L T, Walker J, Johnson N M and Molnar R J 1998 *Appl. Phys. Lett.* **72** 1214
- [100] Naniwae K, Ithoh S K, Amano H, Ithoh K, Hiramatsu K and Akasaki I 1990 *J. Crystal Growth* **99** 381

- [101] Wetzel C, Volm D, Meyer B K, Pressel K, Nilsson S, Mokhov E N and Baranov P G 1994 *Appl. Phys. Lett.* **65** 1033
- [102] Fischer S, Wetzel C, Hansen W L, Bourret-Chourchesne E D, Meyer B K and Haller E E 1996 *Appl. Phys. Lett.* **69** 2716
- [103] Vodakov Y A, Karklina M I, Mokhov E N and Roenkov A D 1980 *Inorgan. Mater.* **17** 537
- [104] Vodakov Y A, Mokhov E N, Roenkov A D, Boiko M E and Baranov P G 1998 *J. Crystal Growth* **183** 10
- [105] Bauer J, Biste L and Bolze D 1977 *Phys. Status Solidi a* **39** 173
- [106] Baranov B, Däweritz L, Gutan V B, Jungk G, Neumann H and Raidt H 1978 *Phys. Status Solidi a* **49** 629
- [107] Fischer F and Schröter F 1910 *Ber. Deutsch Chem. Ges.* **43** 1465
- [108] Kirstenmacher T J, Ecelberger S A and Bryden W A 1993 *J. Appl. Phys.* **74** 1684
- [109] Bryden W A, Morgan J S, Kistenmacher T J, Dayan D, Fainchtein R and Poehler T O 1990 *Mater. Res. Soc. Symp. Proc.* **162** 567
- [110] Hovel H J and Cuomo J J 1971 *Appl. Phys. Lett.* **20** 71
- [111] Krishnaswamy S V, Hester W A, Szedon J R and Francombe M H 1985 *Thin Solid Films* **125** 291
- [112] Foley C P and Tansley T L 1985 *Appl. Surf. Sci.* **22/23** 663
- [113] Puychevriev N and Menoret M 1976 *Thin Solid Films* **36** 141
- [114] Lakshmi E, Mathur B and Bhattacharya A B 1980 *Thin Solid Films* **74** 77
- [115] Zembutsu S and Kobayashi M 1985 *Thin Solid Films* **129** 289
- [116] Matsushita K, Matsuno Y, Hariu T and Shibata Y 1981 *Thin Solid Films* **80** 243
- [117] Aita C R 1982 *J. Appl. Phys.* **53** 1807
- [118] Liaw H M and Cronin W 1993 *Ultrason. Symp. Proc. IEEE* 267
- [119] Kubota K, Kobayashi Y and Fujimoto K 1989 *J. Appl. Phys.* **66** 2984
- [120] Grzegory I, Jun J, Krukowski St, Bockowski M and Porowski S 1993 *Physica B* **185** 99
- [121] Karpinski J, Jun J and Porowski S 1984 *J. Crystal Growth* **66** 1
- [122] Karpinski J, Porowski S and Miotkowska S 1982 *J. Crystal Growth* **56** 77
- [123] Porowski S, Grzegory I and Jun J 1989 *High Pressure Chemical Synthesis* ed J Jurczak and B Baranowski (Amsterdam: Elsevier) p 21
- [124] Ponce F A, Bour D P, Young W T, Saunders M and Steeds J W 1996 *Appl. Phys. Lett.* **69** 337
- [125] Liliental-Weber Z *et al* 1996 *Mater. Res. Soc. Symp. Proc.* **395** 351
- [126] Leszczynski M, Suski T, Perlin P, Grzegory I, Bockowski M, Jun J, Porowski S and Major J 1995 *J. Phys. D: Appl. Phys.* **28** A 149
- [127] Nakamura S 1991 *Japan. J. Appl. Phys.* **A 10** L1705
- [128] Morita M, Isogai S, Shimizu N, Tsubouchi K and Mikohiba N 1981 *Japan. J. Appl. Phys.* **19** L173
- [129] Coates G E 1960 *Organometallic Compounds* (London: Methuen) p 88
- [130] Liu H, Bertolet D C and Rogers J W 1994 *Surf. Sci.* **320** 145
- [131] Jones A C, Whitehouse C R and Roberts J S 1995 *Chem. Vap. Dep.* **1** 65
- [132] Swye B S, Schlup J R and Edgar J H 1991 *Chem. Mater.* **3** 737
- [133] Swye B S, Schlup J R and Edgar J H 1991 *Chem. Mater.* **3** 1093
- [134] Guo G, Kato O and Yoshida A 1993 *J. Appl. Phys.* **73** 7969
- [135] Jones A C, Rushworth S A, Houlton D J, Roberts J S, Roberts V, Whitehouse C R and Critchlow W G 1996 *Chem. Vap. Dep.* **2** 1
- [136] Mizuta M, Fujieda S, Jitsukawa T and Matsumoto Y 1987 *Proc. Int. Symp. GaAs and Related Compounds (Las Vegas, Nevada) 1986* (Bristol: Adam Hilger)
- [137] Jones A C, Auld J, Rushworth S A, Houlton D J and Critchlow G W 1994 *J. Mater. Chem.* **4** 1591
- [138] Jones A C, Auld J, Rushworth S A, Williams E W, Haycock P W, Tang C C and Critchlow G W 1994 *Adv. Mater.* **6** 6
- [139] Auld J, Houlton D J, Jones A C, Rushworth S A and Critchlow G W 1994 *J. Mater. Chem.* **4** 1245
- [140] Jones A C, Rushworth S A, Houlton D J, Roberts J S, Roberts V, Whitehouse C R and Critchlow W G 1996 *Chem. Vap. Dep.* **2** 1, and references therein
- [141] Kouvetakis J and Beach D 1989 *Chem. Mater.* **1** 476
- [142] Lakhota V, Neumayer D A, Cowley A H, Jones R A and Ekerdt J G 1995 *Chem. Mater.* **7** 546
- [143] Neumayer D A, Cowley A H, Decken A, Jones R A, Lakhota V and Ekerdt J G 1995 *J. Am. Chem. Soc.* **117** 5893
- [144] Miehr A, Ambacher O, Rieger W, Metzger T, Born E and Fischer R A 1996 *Chem. Vap. Dep.* **2** 51
- [145] Beaumont B, Gibart P and Faurie J P 1995 *J. Crystal Growth* **156** 140
- [146] Gaskill D K, Bottka N and Lin M C 1986 *Appl. Phys. Lett.* **48** 1449
- [147] Bu Y, Lin M C, Gilliland G D, Chen Y, Ralph S E, Fu L P, Chtchekine D G and Stock S R 1995 *Appl. Phys. Lett.* **66** 2433
- [148] Shimizu M, Hiramatsu K and Sawaki N 1994 *J. Crystal Growth* **145** 209
- [149] Purdy A P 1994 *Inorg. Chem.* **33** 282
- [150] Fischer R A, Miehr A, Metzger T, Born E, Ambacher O, Angerer H and Dimitrov R 1996 *Chem. Mater.* **8** 1357
- [151] Takeda F, Mori T and Takahashi T 1981 *Japan. J. Appl. Phys.* **20** L169
- [152] Lee H C, Lee K Y, Yong Y J, Lee J Y and Kim G H, 1995 *Thin Solid Films* **271** 50
- [153] Yoshida M, Watanabe H and Uesugi F 1985 *J. Electrochem. Soc.* **132** 677
- [154] Beaumont B, Gibart P and Faurie J P 1995 *J. Crystal Growth* **156** 140
- [155] Dupuie J L and Gulari E 1992 *J. Vac. Sci. Technol. A* **10** 18
- [156] Meng G Y, Azema N, Cros B, Durand J and Cot L 1993 *J. Crystal Growth* **129** 610
- [157] Ambacher O, Angerer H, Dimitrov R, Rieger W, Stutzmann M, Dollinger G and Bergmaier A 1997 *Phys. Status Solidi a* **159** 105
- [158] Piner E L, Behbehani M K, El-Masry N A, McIntosh F G, Roberts J C, Boutros K S and Bedair S M 1997 *Appl. Phys. Lett.* **70** 461
- [159] Scholz F *et al* 1997 *Mater. Res. Soc. Symp. Proc.* **449** 3
- [160] Horikoshi Y, Yamaguchi H, Briones F and Kawashima M 1990 *J. Crystal Growth* **105** 326
- [161] Kawaguchi Y, Shimizu M, Hiramatsu K and Sawaki N 1997 *Mater. Res. Soc. Symp. Proc.* **449** 89
- [162] Amano H, Sawaki N, Akasaki I and Toyoda Y 1986 *Appl. Phys. Lett.* **48** 353
- [163] Akasaki I, Amano H, Koide Y, Hiramatsu K and Sawaki N 1989 *J. Crystal Growth* **98** 209
- [164] Hiramatsu K, Itoh S, Amano H, Akasaki I, Kuwano N, Shiraishi T and Oki K 1991 *J. Crystal Growth* **115** 628
- [165] Nakamura S 1991 *Japan. J. Appl. Phys.* **30** L1705
- [166] Wickenden A E, Wickenden D K and Kistenmacher T J 1994 *J. Appl. Phys.* **75** 5367
- [167] George T, Pike W T, Khan M A, Kuznia J N and Chang-Chien P 1995 *J. Electron. Mater.* **24** 241
- [168] Wu X H, Kapolnek D, Tarsa E J, Heyning B, Keller S, Keller B P, Mishra U K, DenBaars S P and Speck J S 1996 *Appl. Phys. Lett.* **68** 1371
- [169] Keller S, Kapolnek D, Keller B P, Wu Y, Heying B, Speck J S, Mishra U K, DenBaars S P 1996 *Japan. J. Appl. Phys.* **35** L285

- [170] Kawakami H, Sakurai K, Tsubouchi K and Mikoshiba N 1988 *Japan. J. Appl. Phys.* **27** L161
- [171] Yamamoto A, Tsujino M, Ohkubo M and Hashimoto A 1994 *J. Crystal Growth* **137** 415
- [172] Kikuchi A, Hoshi H and Kishino K 1994 *Japan. J. Appl. Phys.* **33** 688
- [173] Moustakas T D, Lei T and Molnar R J 1993 *Physica B* **185** 39
- [174] Hwang C-Y, Schurman M J and Mayo W E 1995 *J. Vac. Sci. Technol. A* **13** 672
- [175] Grandjean N, Massies J and Leroux M *Appl. Phys. Lett.* **69** 2071
- [176] Uchida K, Watanabe A, Yano F, Kouguchi S, Tanaka T and Minagawa S 1996 *J. Appl. Phys.* **79** 3487
- [177] Keller S, Keller P B, Wu Yu-F, Heying B, Kapolnek D, Speck J S, Mishra U K and DenBaars S P 1996 *Appl. Phys. Lett.* **68** 1525
- [178] Tsaur B-Y, McClelland R W, Fan J C C, Gale R P, Salerno J P, Vojak B A and Bozler C O 1982 *Appl. Phys. Lett.* **41** 347
- [179] Pribat D, Gerard B, Dupuy M and Legagneux P 1992 *Appl. Phys. Lett.* **60** 2144
- [180] Kato K, Kusunoki T, Takenaka C, Tanahashi T and Nakajima K 1991 *J. Crystal Growth* **115** 174
- [181] Parillaud O, Gil-Lafon E, Gerard B, Etienne P and Pribat D 1996 *Appl. Phys. Lett.* **68** 2654
- [182] Fukui T and Ando S 1989 *Electron. Lett.* **25** 410
- [183] Ando S, Honda T and Kobayashi N 1993 *Japan. J. Appl. Phys.* **32** L104
- [184] Ponce F A 1997 *Mater. Res. Soc. Bull.* **22** 51
- [185] Beaumont B, Haffouz S and Gibart P 1998 *Appl. Phys. Lett.* **72** 921
- [186] Zheleva T S, Nam O-H, Bremser D M and Davis R F 1997 *Appl. Phys. Lett.* **71** 2472 and references therein
- [187] Kato Y, Kitamura S, Hiramatsu K and Sawaki N 1994 *J. Crystal Growth* **144** 133
- [188] Marchand H, Ibbetson J P, Fini P T, Kozodoy P, Keller S, DenBaars S, Speck J S and Mishra U K 1998 *Mater. Res. Soc. Inter. J. Nit. Semi. Res.* **3** 3
- [189] Kapolnek D, Keller S, Vetry R, Underwood R D, Kozodoy P, DenBaars S P and Mishra U K 1997 *Appl. Phys. Lett.* **71** 1204
- [190] Matsuoka T, Yoshimoto N, Sakai T and Katsui A 1992 *J. Electron. Mater.* **21** 157
- [191] Shimizu M, Hiramatsu K and Sawaki N 1994 *J. Crystal Growth* **145** 209
- [192] Sohmer A *et al* 1997 *Mater. Res. Soc. Inter. J. Nit. Semi. Res.* **2** 14
- [193] Ho I and Stringfellow G B 1996 *Appl. Phys. Lett.* **69** 2701
- [194] Koukita A, Takahashi N, Taki T and Seki H 1996 *Japan. J. Appl. Phys.* **35** L673
- [195] Kawaguchi Y, Shimizu M, Hiramatsu K and Sawaki N 1997 *Mater. Res. Soc. Symp. Proc.* **449** 89
- [196] Ruffenach-Clur S, Briot O, Gil B, Aulombard R-L and Rouviere J L 1997 *Mater. Res. Soc. Inter. J. Nit. Semi. Res.* **2** 27
- [197] Kung P, Saxler A, Walker D, Zhang X, Lavado R, Kim K S and Razeghi M 1997 *Mater. Res. Soc. Symp. Proc.* **449** 79
- [198] Herman M A and Sitter H 1989 *Molecular Beam Epitaxy, Springer Series in Materials Science* ed M B Panish (New York: Springer)
- [199] Jennings K R and Linnet J W 1958 *Quart. Rev.* **12** 116
- [200] Manella G G 1963 *Chem. Rev.* **63** 1
- [201] Brown C R and Winkler C A 1970 *Angew. Chem.* **82** 187
- [202] Rössner U, Brun-Le Cunff D, Barski A and Daudin B 1996 *J. Vac. Sci. Technol. A* **14** 2655
- [203] Johnson M A L, Fujita S, Rowland W H Jr, Bowers K A, Hughes W C, He Y W, El-Masry N A, Cook J W Jr and Schetzina J F 1996 *J. Vac. Sci. Technol. B* **14** 2349
- [204] Hoke W E, Lemonias P J and Weir D G 1991 *J. Crystal Growth* **111** 1024
- [205] Molnar R J, Singh R and Moustakas T D 1995 *J. Electron. Mater.* **24** 275
- [206] Angerer H, Ambacher O, Dimitrov R, Metzger T, Rieger W and Stutzmann M 1996 *Mater. Res. Soc. Inter. J. Nit. Semi. Res.* **1** 15
- [207] Tarsa E J, Heying B, Wu X H, Fini P, DenBaars S P and Speck J S 1997 *J. Appl. Phys.* **82** 5472
- [208] Peercy P S 1990 *J. Mater. Res.* **5** 852
- [209] Zywiets T, Neugebauer J and Scheffler M 1998 *Appl. Phys. Lett.* **73** 487
- [210] Guha S, Bojarczuk N A and Kisker D W 1996 *Appl. Phys. Lett.* **69** 2879
- [211] Davis R F, Tanaka S, Rowland L B, Kern R S, Sitar Z, Ailey S K and Wang C 1996 *J. Crystal Growth* **164** 132
- [212] Ghez R and Iyer S S 1988 *IBM J. Res. Develop.* **32** 804
- [213] Sitar Z, Paisley M J, Yan B and Davis R F 1990 *Mater. Res. Soc. Symp. Proc.* **162** 537
- [214] Lin M E, Sverdlov B, Zhou G L and Morkoc H 1993 *Appl. Phys. Lett.* **62** 3479
- [215] Nakamura S, Mukai T and Senoh M 1992 *J. Appl. Phys.* **71** 5543
- [216] Riechert H, Averbeck R, Graber A, Schienle M, Strauß U and Tews H 1997 *Mater. Res. Soc. Symp. Proc.* **449** 149
- [217] Van Hove J M, Carpenter G, Nelson E, Wowchak A and Chow P P 1996 *J. Crystal Growth* **164** 154
- [218] Nguyen N X, Nguyen C and Grider D E 1998 *Electr. Lett.* **34** 309
- [219] Deger C, Born E, Angerer H, Ambacher O, Stutzmann M, Hornsteiner J, Riha E and Fischerauer G 1998 *Appl. Phys. Lett.* **72** 2400
- [220] Holleman A F and Wiberg N 1985 *Lehrbuch der Anorganischen Chemie* (Berlin: de Gruyter)
- [221] Schneider S J and McDaniel C L 1967 *J. Res. Nat. Bur. Stand. A* **71** 317
- [222] Gitlesen G, Herstad O and Motzfeldt K 1966 *Chem. Abstr.* **65** 9819h
- [223] Olette M and Ancey-Moret M F 1963 *Rev. Met.* **60** 569
- [224] Anderson R N and Parlee N A D 1970 *High Temp. Sci.* **2** 289
- [225] MacChesney J B, Bridenbaugh P M and O'Conner P B 1970 *Mater. Res. Bull.* **5** 783
- [226] Slack G A 1973 *J. Phys. Chem Solids* **34** 321
- [227] Neugebauer J and Van de Walle C G 1994 *Mater. Res. Soc. Symp. Proc.* **339** 687
- [228] Mattila T and Nieminen R M 1996 *Phys. Rev. B* **54** 16676
- [229] Tiede E, Thimann M and Senns K 1928 *Ber. Deutsch. Chem. Ges. B* **61** 1568
- [230] Kamyshev V M, Gorbato A G and Agibalova G I 1973 *Chem. Abstr.* **79** 118944v
- [231] Gorbato A G and Kamyshev V M 1973 *Chem. Abstr.* **79** 108947j
- [232] Götz W, Johnson N M, Chen C, Liu H, Kuo C and Imler W 1996 *Appl. Phys. Lett.* **68** 3144
- [233] Abernathy C R, MacKenzie J D, Pearton S J and Hobson W S 1995 *Appl. Phys. Lett.* **66** 1969
- [234] Kawabe K, Tredgold R H and Inuishi Y 1967 *Elect. Eng. Japan* **87** 62
- [235] Taylor K M and Leniez C 1960 *J. Electroch. Soc.* **107** 308
- [236] Pankove J I and Johnson N M (eds) 1991 *Hydrogen in Semiconductors* (Boston: Academic)
- [237] Amano H, Kito M, Hiramatsu K and Akasaki I 1989 *Japan. J. Appl. Phys.* **28** L2112
- [238] Nakamura S, Iwasa N, Senoh M and Mukai T 1992 *Japan. J. Appl. Phys.* **31** 1258
- [239] Brandt M S, Johnson N M, Molnar R J, Singh R and Moustakas T D 1994 *Appl. Phys. Lett.* **64** 2264
- [240] Götz W and Johnson N M 1996 *Appl. Phys. Lett.* **68** 667
- [241] Neugebauer J and Van de Walle C G 1995 *Phys. Rev. Lett.* **75** 4452
- [242] Myoung J M, Shim K H, Kim C, Gluschenkov O, Kim K, Kim S, Turnbull D A and Bishop S G 1996 *Appl. Phys. Lett.* **69** 2722



- [243] Amano H, Akasaki I, Hiramatsu K, Koide N and Sawaki N 1988 *Thin Solid Films* **163** 1156
- [244] Akasaki I, Amano H, Kito M and Hiramatsu K 1991 *J. Luminescence* **48 & 49** 666
- [245] Bergman P, Ying G, Monemar B and Holtz P O 1987 *J. Appl. Phys.* **61** 4589
- [246] Neugebauer J and Van de Walle C G 1998 *Japan. J. Appl. Phys.* at press
- [247] Brandt O, Yang H, Kostial H and Ploog K H 1996 *Appl. Phys. Lett.* **69** 2707
- [248] Zolper J C, Wilson R G, Pearton S J and Stall R A 1996 *Appl. Phys. Lett.* **68** 1945
- [249] Stutzmann M *et al* 1997 *Mater. Sci. Eng. B* **50** 212
- [250] Korakakis D, Ng H M, Ludwig K F and Moustakas T D 1996 *Mater. Res. Soc. Symp. Proc.* **449** 233
- [251] Akasaki I and Amano H 1995 *J. Crystal Growth* **146** 455
- [252] Murakami H, Asahi T, Amano H, Hiramatsu K, Sawaki N and Akasaki I 1991 *J. Crystal Growth* **115** 648
- [253] Nakamura S, Mukai T and Senoh M 1993 *Japan. J. Appl. Phys.* **32** L16
- [254] Yamasaki S, Asami S, Shibata N, Koike M, Manabe K, Tanaka T, Amano H and Akasaki I 1995 *Appl. Phys. Lett.* **66** 1112
- [255] *Landolt-Börnstein, New Series* 1982 Semiconductors, Group III, vol 17a, ed O Madelung (Berlin: Springer)
- [256] Martin G, Strite S, Botchkarev A, Agarwal A, Rockett A, Morkoc H, Lambrecht W R L and Segall B 1994 *Appl. Phys. Lett.* **65** 610
- [257] Martin G, Botchkarev A, Rockett A and Morkoc H 1996 *Appl. Phys. Lett.* **68** 2541
- [258] Yu E and McGill T 1992 *Solid State Physics* vol 46, ed H Ehrenreich and D Turnbull (Boston: Academic) p 1
- [259] Waldrop J R and Grant R W 1996 *Appl. Phys. Lett.* **68** 2879
- [260] Sitar Z, Paisley M J, Yan B, Davis R F, Ruan J and Choyke J W 1991 *Thin Solid Films* **200** 311
- [261] Baur J, Maier K, Kunzer M, Kaufmann U and Schneider J 1994 *Appl. Phys. Lett.* **65** 2211
- [262] Albanesi E A, Lambrecht W R L and Segall B 1994 *J. Vac. Sci. Technol. B* **12** 2470
- [263] Wei S-H and Zunger A 1996 *Appl. Phys. Lett.* **69** 2719
- [264] Murayama M and Nakayama T 1994 *Phys. Rev. B* **49** 4710
- [265] Mileham J R, Pearton S J, Abernathy C R, MacKenzie J D, Shul R J and Kilcoyne S P 1995 *Appl. Phys. Lett.* **67** 1119
- [266] Youtsey C, Adesida I, Romano L T and Bulman G 1997 *Appl. Phys. Lett.* **72** 560
- [267] Minsky M S, White M and Hu E L 1996 *Appl. Phys. Lett.* **68** 1531
- [268] Lu H, Wu Z and Bhat I 1997 *J. Electrochem. Lett.* **33** L8
- [269] Youtsey C, Adesida I and Bulmann G 1997 *Electron. Lett.* **33** 245
- [270] Peng L-H, Chuang C-W, Ho J-K, Huang C-N and Chen C-Y 1998 *Appl. Phys. Lett.* **72** 939
- [271] Adesida I, Mahajan A, Andideh E, Khan M A, Olson D T and Kuzina J N 1993 *Appl. Phys. Lett.* **63** 2777
- [272] Lin M E, Fan Z F, Ma Z, Allen L H and Morkoc H 1994 *Appl. Phys. Lett.* **64** 887
- [273] Ping A T, Adesida I, Khan M A and Kuzina J N 1994 *Electron. Lett.* **30** 1895
- [274] Lee H, Oberman D B and Harris J H Jr 1995 *Appl. Phys. Lett.* **67** 1754
- [275] McLane G F, Casas L, Pearton S J and Abernathy C R 1995 *Appl. Phys. Lett.* **66** 3328
- [276] Adesida I, Ping A T, Youtsey C, Dow T, Khan A A, Olson D T and Kuzina J N 1994 *Appl. Phys. Lett.* **65** 889
- [277] Ping A T, Adesida I and Khan M A 1995 *Appl. Phys. Lett.* **67** 1250
- [278] Pearton S J, Abernathy C R and Ren F 1994 *Appl. Phys. Lett.* **64** 2294
- [279] Pearton S J, Abernathy C R, Ren F, Lothian J R, Wisk P W, Katz A and Constantine C 1993 *Semicond. Sci. Technol.* **8** 310
- [280] Zhang L, Ramer J, Brown J, Zheng K, Lester L F and Hersee S D 1996 *Appl. Phys. Lett.* **68** 367
- [281] Pearton S J, Abernathy C R, Ren F, Lothian J R, Wisk P W and Katz A, 1993 *J. Vac. Sci. Technol. A* **11** 1772
- [282] Vartuli C B, Pearton S J, Abernathy C R, Shul R J, Howard A J, Kilcoyne S P, Parmeter J E and Hagerott-Crawford M 1996 *J. Vac. Technol. A* **14** 1011, and references therein
- [283] Smith S A, Wolden C A, Bremser M D, Hanser A D, Davis R F and Lampert W V 1997 *Appl. Phys. Lett.* **71** 3631
- [284] Shul R J, McClellan G B, Casalnuovo S A, Rieger D J, Pearton S J, Constantine C, Barratt C, Karlicek R F Jr, Tran C and Schurman M 1996 *Appl. Phys. Lett.* **69** 1119
- [285] Kelly M, Ambacher O, Dahlheimer B, Gros G, Dimitrov R, Angerer H and Stutzmann M 1996 *Appl. Phys. Lett.* **69** 1749
- [286] Guo J D, Lin C I, Feng M S, Pan F M, Chi G C and Lee C T 1996 *Appl. Phys. Lett.* **68** 235
- [287] Marlow G S and Das M B 1982 *Solid-State. Electron.* **25** 91
- [288] Lin M E, Ma Z, Huang F Y, Fan Z F, Allen L H and Morkoc H 1994 *Appl. Phys. Lett.* **64** 1003
- [289] Jenkins D W and Dow J D 1989 *Phys. Rev. B* **39** 3317
- [290] Abernathy C R, Pearton S J, Ren F and Wisk P W 1993 *J. Vac. Sci. Technol. B* **11** 179
- [291] Fan Z, Mohammad S N, Kim W, Aktas Ö, Botchkarev A E and Morkoc H 1996 *Appl. Phys. Lett.* **68** 1672
- [292] Binari S C, Dietrich H B, Kelner G, Rowland L B, Doverspike K and Gaskill D K 1994 *Electron. Lett.* **30** 909
- [293] Ruvimov S, Liliental-Webert Z, Washburn J, Duxstad K J, Haller E E, Fan Z-F, Mohammad S N, Kim W, Botchkarev A E and Morkoc H 1996 *Appl. Phys. Lett.* **69** 1556
- [294] Mori T, Kozawa T, Ohwaki T, Taga Y, Nagai S, Yamasaki S, Asami S, Shibata N and Koike M 1996 *Appl. Phys. Lett.* **69** 3537
- [295] Weast R C *et al* (eds) 1990 *CRC Handbook of Chemistry and Physics* (Boca Raton, FL: CRC)
- [296] Pankove J I and Schade H E 1974 *Appl. Phys. Lett.* **25** 53
- [297] Michaelson H B 1994-95 *CRC Handbook of Chemistry and Physics* 75th edn, ed D R Lide (Boca Raton, FL: CRC) pp 12-113
- [298] Foresi J S and Moustakas T D 1993 *Appl. Phys. Lett.* **62** 2859
- [299] Hacke P, Detchprohm T, Hiramatsu K and Sawaki N 1993 *Appl. Phys. Lett.* **63** 2676
- [300] Guo J D, Feng M S, Guo R J, Pan F M and Chang C Y 1995 *Appl. Phys. Lett.* **67** 2657
- [301] Wang L, Nathan M I, Lim T-H, Khan M A and Chen Q 1996 *Appl. Phys. Lett.* **68** 1267
- [302] Cordes H and Chang Y A 1997 *Mater. Res. Soc. Inter. J. Nit. Semi. Res.* **2** 2
- [303] Liu Q Z, Yu L S, Lau S S, Redwing J M, Perkins N R and Kuech T F 1997 *Appl. Phys. Lett.* **70** 1275
- [304] Rieger W *et al* 1998 *Proc. 22nd Workshop on Compound Semiconductor Devices and Integrated Circuits (Zeuthen, Germany)* 24-27 May 1998
- [305] Vartuli C B, Pearton S J, Abernathy C R, MacKenzie J D, Shul J R, Zolper J C, Lovejoy M L, Baca A G and Hagerott-Crawford M 1996 *J. Vac. Sci. Technol. B* **14** 3520
- [306] Campbell C 1989 *Surface Acoustic Wave Devices and their Signal Processing Applications* (New York: Academic)
- [307] Foster N F 1964 *Trans. AIME* **230** 1503
- [308] Foster N F and Rozgonyi G A 1966 *Appl. Phys. Lett.* **8** 221

- [309] Kuwano Y and Tanmatsu K 1977 *Television* **31** 845
- [310] Hickernell F S 1971 *IEEE Ultrason. Symp.* P-1
- [311] Okano H, Takahashi Y, Tanaka T, Shibata K and Nakano S 1992 *Japan. J. Appl. Phys.* **31** 3446
- [312] Tsubouchi K and Mikoshiba N 1983 *Ultrason. Symp. Proc. IEEE* 299
- [313] Duffy M T, Wang C C, O'Clock G D Jr, McFarlane S H III and Zanzucchi P J 1973 *J. Electron. Mater.* **2** 359
- [314] Liu J K, Lakin K M and Wang K L 1975 *J. Appl. Phys.* **46** 3703
- [315] Lakin K M, Wang J S, Kline G R, Landin A R, Chen Y Y and Hunt J D 1982 *Ultrason. Symp. Proc. IEEE* 466
- [316] Lakin K M, Kline G R, Ketcham R S, Martin J T and McCarron K T 1989 *43rd Annual Symp. on Frequency Control* p 536
- [317] Shur M S and Khan M A 1995 *Electrochem. Soc. Proc.* **95-21** 128
- [318] Razeghi M and Rogalski A 1996 *J. Appl. Phys.* **79** 7433
- [319] Khan M A, Kuzina J N, Olson D T, Van Hove J M, Blasingame M and Reitz L F 1992 *Appl. Phys. Lett.* **60** 2917
- [320] Yoshida S, Misawa S and Gong S 1982 *J. Appl. Phys.* **53** 6844
- [321] Walker D, Zhang X, Kung P, Saxler A, Javadpour S, Xu J and Razeghi M 1996 *Appl. Phys. Lett.* **68** 2100
- [322] Van Hove J M, Hickman R, Klaassen J J, Chow P P and Ruden P P 1997 *Appl. Phys. Lett.* **70** 2282
- [323] Chen Q, Yang J W, Osinsky A, Gangopadhyay S, Lim B, Anwar M Z, Khan M A, Kuksenkov D and Temkin H 1997 *Appl. Phys. Lett.* **70** 2277
- [324] Zhu G Y, Salvador A, Kim W, Fan Z, Lu C, Tang H, Morkoc H, Smith G, Estes M, Goldenberg B, Yang W and Krishnankutty S 1997 *Appl. Phys. Lett.* **7** 2154
- [325] Xu G Y, Salvador A, Kim W, Fan Z, Lu C, Tang H, Morkoc H, Smith G, Estes M, Goldenberg B, Yang W and Krishnankutty S 1997 *Appl. Phys. Lett.* **71** 2154
- [326] Zhang X, Kung P, Walker D, Piotrowski J, Rogalski A, Saxler A and Razeghi M 1995 *Appl. Phys. Lett.* **67** 2028
- [327] Khan M A, Kuznia J N, Olson D T, Schaff W, Burm J and Shur M 1994 *Appl. Phys. Lett.* **65** 1121
- [328] Littlejohn M A, Hauser J R and Glisson T H 1975 *Appl. Phys. Lett.* **26** 625
- [329] Gelmont B L, Kim K S and Shur M S 1993 *J. Appl. Phys.* **74** 1818
- [330] Chin V W L, Tansley T L and Osotchan T 1994 *J. Appl. Phys.* **75** 7365
- [331] Rode D L and Gaskill D K 1995 *Appl. Phys. Lett.* **66** 1972
- [332] Foutz B E, Eastman L F, Bhapkar U V and Shur M S 1997 *Appl. Phys. Lett.* **70** 2849
- [333] Gaska R, Yang J W, Osinsky A, Chen Q, Khan M A, Orlov A O, Snider G L and Shur M S 1998 *Appl. Phys. Lett.* **72** 707
- [334] Lin C F, Cheng H C, Huang J A, Feng M S, Guo J D and Chi G C 1997 *Appl. Phys. Lett.* **70** 2583
- [335] Sichel E K and Pankove J I 1977 *J. Phys. Chem. Solids* **38** 330
- [336] Khan M A, Chen Q, Shur M S, Dermott B T, Higgins J A, Burm J, Schaff W and Eastman L F 1996 *Electron. Lett.* **32** 357
- [337] Fan Z, Mohammad S N, Aktas O, Botchkarev A E, Salvador A and Morkoc H 1996 *Appl. Phys. Lett.* **69** 1229
- [338] Wu Y-F, Keller B P, Keller S, Kapolnek D, Kozodoy P, DenBaars S P and Mishra U K 1996 *Appl. Phys. Lett.* **69** 1438
- [339] Wu Y-F, Keller B P, Keller S, Nguyen N X, Nguyen M L C, Jenkins T J, Kehias L T, DenBaars S P and Mishra U K 1997 *IEEE Electron. Device Lett.* **18** 438
- [340] Wu Y-F, Keller S, Kozodoy P, Keller B P, Parikh P, Kapolnek D, DenBaars S P and Mishra U K 1997 *IEEE Electron. Device Lett.* **18** 290
- [341] Gaska R, Osinsky A, Yang J W and Shur M S 1998 *IEEE Electron. Device Lett.* **19** 89
- [342] Yu E T, Sullivan G J, Asbeck P M, Wang C D, Qiao D and Lau S S 1997 *Appl. Phys. Lett.* **71** 2794
- [343] Eastman L 1998 *Mater. Res. Soc. Symp. Proc.* **482** at press
- [344] Xie W, Grillo D C, Gunshor R L, Kobayashi M, Jeon H, Ding J, Nurmikko A V, Hua G C and Otsuka N 1992 *Appl. Phys. Lett.* **60** 1999
- [345] Koga K and Yamaguchi T 1991 *Prog. Crystal Growth Character* **23** 127
- [346] Eason D E, Yu Z, Hughes W C, Rowland W H, Boney C, Cook J W Jr, Schetzina J F, Cantwell G and Harasch W C 1995 *Appl. Phys. Lett.* **66** 115
- [347] Maruska H P, Stevenson D A and Pankove J I 1973 *Appl. Phys. Lett.* **22** 303
- [348] Pankove J I 1973 *J. Luminescence* **7** 114
- [349] Maruska H P and Stevenson D A 1974 *Solid-State Electron.* **17** 1171
- [350] Kawabata T, Matsuda T and Koike S 1984 *J. Appl. Phys.* **56** 2367
- [351] Jacob G and Bois D 1977 *Appl. Phys. Lett.* **30** 412
- [352] Lagerstedt O, Monemar B and Gislason H 1978 *J. Appl. Phys.* **49** 2953
- [353] Nakamura S, Mukai T and Senoh M 1991 *Japan. J. Appl. Phys.* **30** L1998
- [354] Nakamura S, Mukai T and Senoh M 1994 *Appl. Phys. Lett.* **64** 1687
- [355] Nakamura S 1995 *J. Vac. Sci. Technol. A* **13** 705
- [356] Craford M G 1992 *Circuits & Devices* September 24
- [357] Meyer M 1996 *Semicond. Comp.* **2** 32
- [358] Dingle D, Shaklee K L, Leheny R F and Zetterstrom R B 1971 *Appl. Phys. Lett.* **19** 5
- [359] Redwing J M, Loeber D A S, Anderson N G, Tischler M A and Flynn J S 1996 *Appl. Phys. Lett.* **69** 1
- [360] Hofmann R *et al* 1996 *Appl. Phys. Lett.* **69** 2068
- [361] Nakamura S, Senoh M, Nagahama S, Iwasa N, Yamada T, Matsushita T, Sugimoto Y and Kiyoku H 1996 *Appl. Phys. Lett.* **69** 1477
- [362] Sakai H, Koide T, Suzuki H, Yamaguchi M, Yamasaki S, Koike M, Amano H and Akasaki I 1995 *Japan. J. Appl. Phys.* **34** L1429
- [363] Kneissl M, Bour D P, Johnson N M, Romano L T, Krusor B S, Donaldson R, Walker J and Dunnrowicz C 1998 *Appl. Phys. Lett.* **72** 1539
- [364] Nakamura S, Senoh M, Nagahama S, Iwasa N, Yamada T, Matsushita T, Kiyoku H and Sugimoto Y 1996 *Appl. Phys. Lett.* **68** 2105
- [365] Kuramata A, Domen K, Soeji R, Horino K, Kubota S and Tanahashi T 1997 *Japan. J. Appl. Phys.* **36** L1130
- [366] Nakamura S, Senoh M, Nagahama S, Iwasa N, Yamada T, Matsushita T, Sugimoto Y and Kiyoku H 1996 *Appl. Phys. Lett.* **69** 3034
- [367] Nakamura S *et al* 1997 *Japan. J. Appl. Phys.* **36** L1568
- [368] Nakamura S *et al* 1998 *Appl. Phys. Lett.* **72** 2014